Karlsruhe Institute of Technology

Understanding low-level clouds in western Equatorial Africa during the long dry season

Zur Erlangung des akademischen Grades eines

Doktors der Naturwissenschaften (Dr. rer. nat.)

von der KIT-Fakultät für Physik
des Karlsruher Instituts für Technologie (KIT)

genehmigte

Dissertation

von

M. Sc. Raffael Aellig

geboren in Jegenstorf BE (Schweiz)

February 29, 2024

Tag der mündlichen Prüfung: 26. Januar 2024
Erster Gutachter: Prof. Dr. Andreas H. Fink
Zweiter Gutachter: Prof. Dr. Peter Knippertz

Abstract

The thesis uses a variety of observational data and numerical weather prediction model experiments to show the causes of the genesis and lysis of low-level clouds in tropical western Equatorial Africa during the long dry season from June to September. Such low-level clouds play a crucial role in the conservation of the rainforest and the Earth's radiation budget. However, low-level clouds are not accurately represented in weather and climate models, leading to biased calculations based on more precise radiation budgets, including climate change projections.

Low-level clouds have different phenotypic characteristics depending on the perspective, which are highlighted in this thesis. By utilising synoptic weather station data (EECRA, ISD, MIDAS, AMMA) and spaceborne satellite data (MSG, CALIPSO, CloudSat), we can identify the distinct diurnal cycle of clouds in various parts of Gabon. In the coastal region, low-level clouds show a morning breakup, while on the windward side of the Chaillu Mountains, a stagnant layer forms without clearing. In contrast, the eastern region of Gabon experiences a large amplitude of low-level clouds in the diurnal cycle. The data from the station evidences a transition from cumulus to stratocumulus throughout the day, signifying the break-up of the cloud cover due to convection. Furthermore, Mesoscale convective systems are observable in the Northeast of the Republic of Congo, and are heading towards northwest, likely resulting in showers in the Northeast of Gabon. Additionally, the mid- and high-level cloud and the Mesoscale Convective Systems lower the precision of detecting low-level clouds from space, since they obstruct the view. The cloud fraction product 2B-Geoprof-LiDAR, acquired by the sun-synchronous satellites CALIPSO and CloudSat, provides valuable information regarding on the vertical positioning of low-level clouds over in various regions of western Equatorial Africa. Notably, a significant contrast exists between ocean and land, with the former exhibiting a highly stratiform low-level cloud layer, whereas the land encounters more vertical disruption. This can be attributed to its rougher surface and stronger daytime convection.

Using the Numerical Weather Prediction model ICON, noticeable differences in temperature, humidity, wind, and stability are apparent between explicit and parameterised convection. The deep convection parameterisation caused an atmospheric drying at the boundaries of the simulated domain due to convective precipitation. In the parameterised version, a lower moisture content is advected into the innermost model nest, as demonstrated by the moisture budgets at the boundaries of the domain. This is corroborated by a reduction in low-level clouds and precipitation in western Equatorial Africa. Furthermore, the parameterisation of shallow convection results in a decrease in moisture in the lower troposphere and an increase in the transition region between the lower and middle troposphere. The parameterisation scheme lifts the boundary layer resulting in reduced specific humidity in the humid mixed layer, which extends deeper into the middle troposphere. This area is comparably drier in the explicit run. By utilizing the Froude Number as a stabilization indicator, evidence reveals that there is a nocturnal flow around the Chaillu Mountains, as has been documented in historical observations, already. Overall a comprehensive understanding of low-level cloud is conducted in this study.

Zusammenfassung

Die Dissertation zeigt anhand von verschiedenen Beobachtungsdaten und numerischen Wettervorhersagemodellen die Ursachen für die Entstehung und Auflösung niedriger Wolken im westlichen Äquatorialafrika während der langen Trockenzeit von Juni bis September. Tiefe Wolken spielen eine wichtige Rolle bei der Erhaltung des Regenwaldes und im Strahlungshaushalt der Erde. Sie werden jedoch in Wetter- und Klimamodellen nicht korrekt repräsentiert, was zu Ungenauigkeiten in Berechnungen führt, die auf korrekteren Strahlungsbudgets basieren, wie z.B. Projektionen des Klimawandels.

Niedrige Wolken haben je nach Perspektive unterschiedliche phänotypische Eigenschaften, die in dieser Dissertation untersucht werden. Mit Hilfe von Stationsdaten und Satellitendaten konnte der unterschiedliche Tagesgang der Wolken zwischen der küstennahen Region, in der die tiefen Wolken ein morgendliches Aufbrechen zeigen, der windzugewandten Seite der Chaillu Berge, wo sich eine Staulage ohne Aufklarung bildet, und dem östlichen Teil Gabuns, der durch eine große Amplitude der tiefen Wolken im Tagesgang gekennzeichnet ist, gebildet werden. Die Stationsdaten zeigen zudem einen Übergang von Cumulus zu Stratocumulus im Tagesverlauf, was auf eine durch Konvektion aufgebrochene Wolkendecke hindeutet. Über dem Nordosten der Republik Kongo sind ebenfalls mesoskalige konvektive Systeme zu erkennen, die sich in Richtung Nordwesten bewegen und dementsprechend im Nordosten von Gabun Regenschauer bringen können. Darüber hinaus verringern diese Wolken und die Wolkenausläufer die Genauigkeit der Erkennung niedriger Wolken aus dem Weltraum, da sie die Wolken verdecken. Das Produkt 2B-Geoprof-LiDAR, das auf den sonnensynchronen, erdumfliegenden Satelliten CALIPSO und CloudSat basiert, lieferte außerdem Informationen über die vertikale Verteilung von Wolken in verschiedenen Regionen im westlichen Äquatorialafrika. Ein Hauptunterschied zwischen Ozean und Land ist die sehr stratiforme Wolkenschicht über dem Wasser, die über Land vertikal viel stärker perturbiert wird, einerseits durch die rauere Oberfläche und andererseits durch die stärkere Konvektion tagsüber über Land.

Bei der Verwendung des numerischen Wettervorhersagemodells ICON gibt es auffällige Unterschiede in Temperatur, Feuchte, Wind und Stabilität zwischen expliziter und parametrisierter Konvektion. Die Parametrisierung der hochreichenden Konvektion führt zu einer Austrocknung der Atmosphäre an den Grenzen der innersten Domain durch konvektiven Niederschlag. In der parameterisierten Version wird ein entsprechend niedriger Feuchtegehalt in die Modelldomain transportiert, wie anhand von des Feuchtebudgets an den Domaingrenzen gezeigt wird. Dies ist erkennbar an der geringeren Anzahl von tiefen Wolken und dem reduzierten Niederschlag im westlichen Äquatorial Afrika. Die Parameterisierung der flachen Konvektion führt zu einer Austrocknung der unteren Troposphäre und einer Feuchtigkeitsanhäufung im Übergang von der unteren zur mittleren Troposphäre im Vergleich zur Simulation ohne parametrisierte Konvektion. Das Parameterisierungsschema hebt die Grenzschicht an, was zu einer niedrigeren spezifischen Feuchte in der feuchten Mischungsschicht führt, die im expliziten Lauf weiter in die trockenere mittlere Troposphäre reicht. Mithilfe der Froude-Zahl, die einen Stabilisierungsindikator darstellt, kann gezeigt werden, dass die Chaillu Berge in der Nacht umströmt werden, was bereits in historischen Beobachtungen aufgezeichnet wurde.

Preface

Raffael Aellig, the PhD candidate, confirms that he contributed significant scientific research. The thesis contains material from the following publications:

> Champagne, O.*, Aellig R.*, Fink, A. H., Philippon, N., Camberlin, P., Moron, V., Knippertz, P., Seze, G., and v. d. Linden, R., "Climatology of low-level clouds over Western equatorial Africa based on ground observations and satellites". Journal of Climate 36.13 (2023): 4289-4306.
> *Both authors contributed equally to the manuscript

> Aellig R., Moron, V., Camberlin, P. "Cloud observing data of 85 stations in western Central Africa". Dataset published on KITopen, (2023). https://doi.org/10.5445/IR/1000150635.

The reasearch was done within the project "Dynamics, Variability and Bioclimatic Effects of Low Clouds in Western Central Africa" (DYVALOCCA), a trinational project of France, Germany and Gabon, consisting contribution of the Université Grenoble Alpes, the Université d'Aix-Marseille, the Université de Bourgogne, Karlsruhe Institute of Technology and the Université Omar-Bongo in Libreville. The project was funded by the binational funding call from the "Agence nationale de la recherche" (ANR) and the "Deutsche Forschungsgemeinschaft" (DFG). The proposal for for the research project was written by Dr. Nathalie Philippon and Prof. Dr. Andreas H. Fink.

Following datasets contributed to the success of this thesis: the Integrated Global Radiosonde Archive (IGRA) of the National Centers for Environmental Information (NCEI), the NCAR Upper Air Database of the National Center for atmospheric research (NCAR), the Integrated Surface Database (ISD) of NCEI, Met Office Integrated Data Archive System (MIDAS) of the United Kingdom Met Office, the African Monsoon Multidisciplinary Analysis (AMMA), the Meteosat Second Generation (MSG) of EUMETSAT, the CALIOP satellite of the Centre national d'études spatiales (CNES), and the CloudSat satellite of NASA.

The PhD candidate was supervised by Prof. Dr. Andreas H. Fink and co-supervised by Prof. Dr. Peter Knippertz. This copy has been supplied on the understanding that this is copyright material and that no quotation from the thesis may be published without proper acknowledgement.

Contents

List of Figures

List of Tables

Part I.

Introduction

1. Introduction

Low level clouds are a central factor in our climate and weather systems. They affect the radiation budget of our Earth system. This is because clouds reflect shortwave radiation back into space and absorb longwave and shortwave radiation, whose energy can remain in the atmosphere. In addition, low-level clouds emit radiation depending on their temperature. These and other processes affect the greenhouse effect, and therefore how much energy is absorbed in which part of the world.

However, these low-level clouds are not fully understood. For one thing, their effect on current weather and climate is hard to quantify (Klein et al., 2018) and a main source of uncertainty in climate models (Dufresne and Bony, 2008). For example, it is very difficult to say exactly how much shortwave solar radiation is absorbed by a stratocumulus cloud and how much is reflected. An incorrect assumption quickly leads to large biases in the radiation budget. It is a challenging task to precisely quantify the impact of low clouds on the climate (Wang, 2013). On the other hand, the formation and dissipation of low-level clouds is not fully understood. The physics and associated processes can now be described by theory at smallest scales (Houze, 2014), but research is still trying to understand the various processes involved in cloud genesis and lysis. However, observations are needed to understand low-level clouds.

1.1. Cloud observations

Cloud measurements and observations have been made for centuries using bare eye. Historical observations date back to the Ancient and Middle Ages and became increasingly significant during modern ship explorations. During the era of great discoveries, meteorology, including the study of cloud phenology, gained growing significance. The increasing importance of meteorology was driven by the need to anticipate and mitigate the impact of adverse weather events and avoid surprises during exploration. Over the past two centuries, increasing numbers of systematic weather observations have been made.

Specifically, the publication of the first meteorological journals spurred the development of meteorology in German-speaking regions (Brönnimann, 2009). Since then, research in meteorology and climatology has progressively expanded, and a greater number of observations have been conducted using precise measurement technology. These days, cloud observations are carried out according to a standardised procedure established by the World Meteorological Organisation (WMO, 2019b). However, African weather research did not receive much attention from the meteorological science community during the first half of the 20th century. In comparison to Europe, there were limited weather observations made especially in Central Africa. Currently, significant differences still persist between the data recorded in Europe, North America, China, and Africa. Recorded observations in Africa, particularly in Central Africa, are rare (Bigot et al., 2016, 2016; Nicholson et al., 2018) and challenging to obtain from sources. If there are any measurements in this region, they mainly concentrate on the rainy season. The absence of knowledge regarding the condition of the atmosphere and climate exacerbates the challenge of comprehending the mechanisms responsible for low-level cloud formation and their dynamics within the atmosphere.

1.2. The importance of low-level clouds in western Equatorial Africa

Particularly crucial for the sustainability of the rainforest in western Central Africa (WEA) are the low-level clouds. These clouds play a vital role by reducing incoming light, preventing stress on plants and trees. Additionally, they help maintain high humidity in the lower atmosphere near the ground, as noted by Philippon et al. (Philippon et al., 2019). In Gabon, stratocumulus clouds typically cover the country during the dry season (Dommo et al., 2018).

The low-level cloud cover (LLCC) in WEA during the extended dry season from June to September (JJAS), while the Intertropical Convergence Zone (ITCZ) is positioned farther north, holds significant importance for the ecosystem's dynamics (Philippon et al., 2019). The Congo Basin and its surroundings boast the second-largest primary rainforest area globally, trailing only the Amazon Rainforest (Mayaux et al., 2013). Functioning as a habitat for diverse flora and fauna species, it concurrently serves as a crucial carbon reservoir. The rainforest plays a pivotal role in the climate, often referred to as the "lung of the Earth's atmosphere" (Pan et al., 2011).

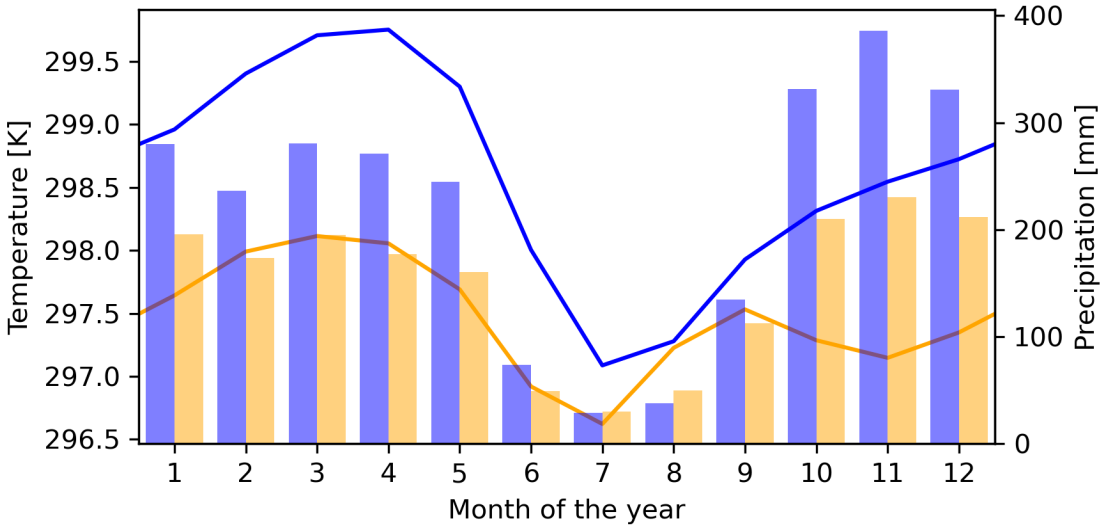

Figure 1.1.: Climate Diagram of Libreville (Blue) at the coast and Franceville M'vengue (Orange) on the Batéké plateau. Lines are the mean monthly temperatures [K] and bars are the monthly precipitations [mm] averaged from 1940 to 2022 based on ERA5 Hersbach et al., 2020 with the nearest grid point to the respected location.

In the WEA, annual rainfall ranges from 1500 to 2500 mm (see Fig. 1.1, Maloba Makanga, 2010), less than in the Amazonian rainforest, which can receive up to 3000 mm/year. However, the tropical rainforest in WEA can survive the relatively dry months from June to September, when rainfall is typically absent in Gabon. The key factor that allows the tropical rainforest to persist is low level cloud cover (LLCC) during the dry season. LLCC reduces sunlight and maintains a cool and moist environment by isolating the rainforest from the middle and upper troposphere. The deck of the LLCC preserves the forest (Oliveira et al., 2014). Without LLCC, plants would experience heat and water stress, potentially leading to the transformation of a rainforest into a savannah over time. The Okoumé tree grows naturally in relatively cooler conditions during the dry season and is a major export for Gabon's forestry industry (Guidosse et al., 2022). The cooling effect of LLCCs is critical for ecosystem functions, parts of the economy in WEA, crucial as possible moisture source for near-by semi-arid regions Spracklen et al., 2012, and serves as carbon storage for climate stability. A substantial reduction in LLCC due to climate change could serve as a critical tipping point for WEA forests, potentially posing a more significant threat than deforestation in the region (Mayaux et al., 2013).

Paleoclimatic investigations reveal a notable volatility in Central African forests. Approximately 2500 years ago, during the last forest crisis, evergreen forests managed to survive in three primary refugia, including a littoral and submontane refuge in WEA (Maley et al., 2018). However, there is ongoing debate about whether this crisis was primarily influenced by climatic factors, such as Atlantic and Pacific El Niño variability, or by human activities linked to the Bantu expansion across Central Africa (Garcin et al., 2018; Bayon et al., 2019). Consequently, there is an urgent need to enhance our understanding of the mechanisms governing LLCC in WCA.

2. Theoretical Background

LLCC in WEA during the long dry season from June to September is important for flora, fauna, climate and socio-economic aspects, as explained in the previous chapter. However, LLCC in WEA are poorly understood. The reasons for genesis and lysis are not well understood. This also makes it difficult to predict these LLCC in the face of changing climatic and anthropogenic conditions. They strongly influence the radiation budget of the atmosphere (Wang, 2013). Accordingly, they contribute to the greenhouse effect, which in turn leads to changing climatic conditions as the cloud cover changes. A broad and improved understanding and focus on unravelling these LLCC during the long dry season in WEA is therefore of great importance.

Therefore, an overview about the actual knowledge about LLCC in WEA will be given. As a starting point the geographical situation will be explained with its climatological behaviour in this region. The focus will be on the current understanding of the genesis and lysis of LLCC. Additionally, this paper will present a diverse perspective on LLCC and explore previous research in the field. Further, the possibilities to simulate LLCC in WEA, will be elaborated.

2.1. Geography of western Equatorial Africa

Western Equatorial Africa includes the countries of Gabon, the Republic of Congo (RC) and Equatorial Guinea. Gabon contains the cities of Libreville, Port-Gentil, Franceville and Moanda (see Fig. 2.1. Among them, Libreville and Port-Gentil are located on the coast and larger in size. Pointe-Noire and Brazzaville, on the other hand, are two larger cities in RC. There is anthropogenic influence on nature around these cities and other settlements. However, the region is mostly covered with primeval forest (Megevand, 2013, Hymas, 2016) and therefore wilderness.

Gabon has a land area of over 267,000 square kilometres and a population of approximately 2.5 million individuals. The majority of this population resides in the major

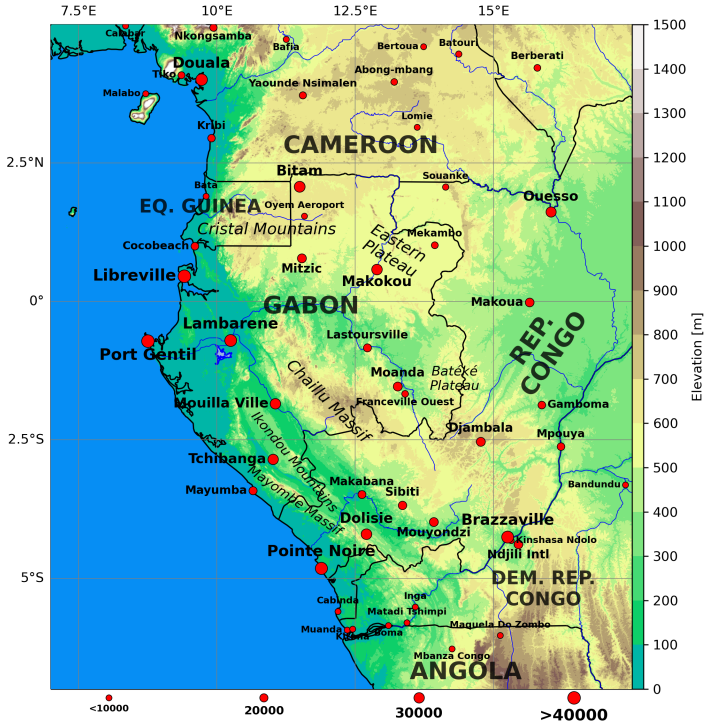

Figure 2.1.: Topography of western Equatorial Africa including the orography in meters. Red dots are stations and the size is the amount of available data reports.

urban centres of Libreville, Port-Gentil, Franceville, and Moanda. As the population is mainly concentrated in the aforementioned agglomerations, the rural areas are extremly sparesly populated, as the average population density is already low.

Gabon is geographically diverse and can be subdivided into regions. The coastal region follows the path of the Atlantic Ocean (see Fig. 2.1). The Mayombe and Ikondoue mountains, located in the south, are the only orographic elevations in the coastal region. Rivers flowing northwestwards come to an end near Lambaréné in the Ogooué River, while others flow into the South Atlantic directly. The Chaillu Mountains are found in the south of Gabon and extending into the RC, although elevations exceed roughly 1000 m.a.s.l. one of the highest peaks, Mount Mimongo, has a height of 1020 m.a.s.l. The Cristal mountains are located in the north of Gabon and in Equatorial Guinea and also have elevations below 1000 m.a.s.l. The Ogooué River runs through the Ogooué Valley between these mountain ranges. Its spring is in the RC, just southeastern of Gabon on the Batéké plateau. The Ogooué river flows north-westwards through the towns of Franceville and Lastourville

before reaching Booué. It flows farther west via Lambaréné until it reaches the South Atlantic to the south of Port-Gentil after more than 1200 km. Nearly 75% of Gabon is drained by the Ogooué. Another orographic feature is the Batéké plateau, which lies to the Southeast of Gabon and extends into the RC. The area to the east of Franceville has savannah-like characteristics and is not as densely forested as the rest of the country. The whole area is full of small rivers and is hilly. Towards the coast, the orography becomes flatter.

2.2. The climatology of Gabon

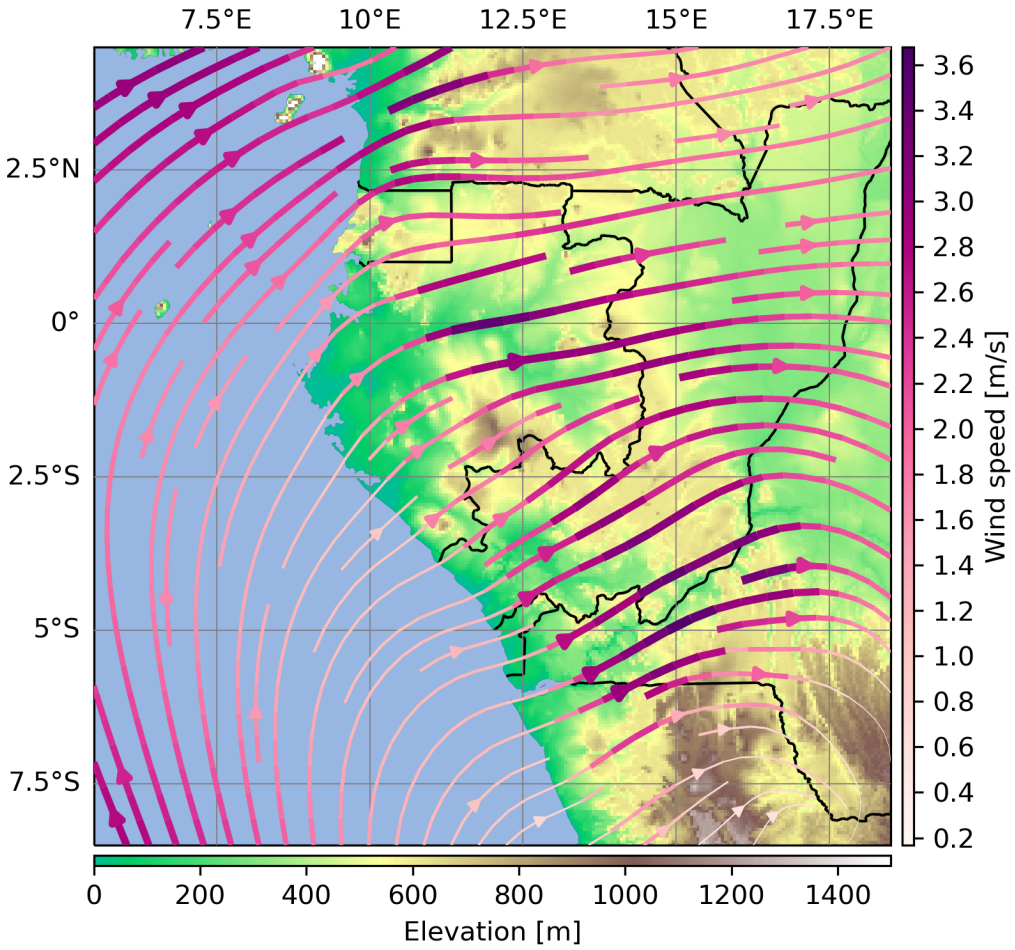

Figure 2.2.: Streamline averaged over July and August and from 1940 to 2022 based on ERA5 at the 925 hPa level with the wind speed in meters per seconds (Hersbach et al., 2020).

The Gabonese climatology is characterised by two rainy seasons and two dry seasons (see Fig. 1.1). Around the turn of the year, there is a short dry period, although its timing varies slightly. This is followed by a longer rainy season from February to May, followed by the long dry season beginning in early June and lasting until late September. The temperatures during the dry season are generally lower than during the rainy season, but the variations cannot be compared to boreal conditions (see Fig. 1.1). From October to December, a brief but intense rainy season occurs in western equatorial Africa.

The beginning of the rainy and dry periods differ in timing and location in this region. For example, the northern area of Gabon experiences an earlier onset of rain in September, while the Batéké Plateau sometimes remains dry until mid-October. Additionally, the dry season is characterised by minimal rainfall. Reports gathered from rainfall collectors suggest that rainfall in the Southeast is almost non-existent from June to September, while in the North, where the dry season is shorter, there can be occasional heavy rains during the dry season (Maloba Makanga, 2010).

The rainy season in western Equatorial Africa is typically dominated by mesoscale convective systems (MCS) that exhibit a high frequency of lightning strikes (Toracinta and Zipser, 2001, Christian et al., 2003, Williams and Sàtori, 2004, Zipser et al., 2006, Albrecht et al., 2016). MCSs occur along the Atlantic coast from March to May. Moreover, studies have shown that elevated terrain and land-sea breeze could act as a trigger mechanism for MCSs (Laing et al., 2011). Land-sea breeze interactions in WEA, resulting in high precipitation rates, are currently the subject of research (Hartman, 2018).

In addition, the northward flowing Benguela Current (Peterson and Stramma, 1991, Moroshkin et al., 1970) dominates the coastal waters of WEA. Also, there is an occurrence of deep, cold water upwelling along the coast. Periodic occurrences of Benguela Niña events (Imbol Koungue et al., 2019; Shannon and Pillar, 1986) magnify the sea surface cooling effect on the lower troposphere, influencing cloud formation in the southeastern Atlantic (Philander et al., 1996). A stronger land-sea temperature contrast can result from an increased cooling of the sea surface temperature along the Benguela Current. This, in turn, encourages the initiation of MCSs by promoting the circulation of land-sea breeze (Howard and Washington, 2018). Additionally, there is a significant seasonal dependence and connection between Atlantic sea surface temperature (SST) and precipitation variability in West Africa (Balas et al., 2007).

In Western Equatorial Africa, the lower level winds blow northerly to north-easterly over the Atlantic Ocean. As you travel farther inland, the winds change to westerlies. This

can be observed in Figure 1, which illustrates the streamlines at an altitude of 925 hPa. The winds change to an easterly direction at around 800 to 750 hPa, although it is not shown here.

Recent research suggests that the WEA region experiences considerable cloudiness during the dry season (Wilson and Jetz, 2016). These clouds shield the rainforest from excessive solar radiation and insulate the lower atmosphere, thus maintaining high humidity levels within the mixed layer (Philippon et al., 2019). The daily frequency of cloud cover averages at 80% (Philippon et al., 2016). Additionally, it seems that low-level clouds have a significant amplitude in the diurnal cycle (Eastman and Warren, 2014).

The behaviour of low-level clouds in altered climates proves challenging to predict, owing to ambiguous alterations in their formation mechanisms due to various factors like augmented turbulence and temperature. For instance, amplified turbulence may lead to earlier cloud breakups; whereas increased temperature would increase the saturation capacity, causing low-level clouds to form later and in smaller numbers. Due to our inadequate knowledge of low-level clouds, it is challenging to make robust predictions of their behaviour in a changing climate. Therefore, the following section provides an overview of historical weather observations in western Equatorial Africa, including the first documented low-level clouds in the region.

2.3. Early observations

Meteorological observations, comprising of clouds and wind systems, were already being done in WEA in 1875, as detailed and summarised by Brönimann (2009). Initial investigations of meteorology and climatology in WEA were conducted by Alexander Danckelmann (1878) and supplemented by Oskar Lorenz (1878). The documented data consist of a meteorological observation station that was in operation for almost two years, situiated near the coast, slightly south of Pointe-Noire (Danckelmann), and four temporary observation stations situated along the river Ogooués between Lambaréné and Lopé. Cloud and fog veils were seen for several consecutive days at the coastal station during the dry season. August and September were the months with the highest amount of cloud cover with 78% percent of the clouds moving towards the west and north. The most commonly observed clouds moving towards west and north were cumulus, stratus and stratocumulus. During the dry season, thunderstorms were indicated by the observation of sheet lightning to the north. The onset of the sea breeze was generally observed between 9 and 10 in the

morning. Calm weather was usually witnessed around sunset, however, the wind was variable.

The measurements taken along the Ogooué were of shorter duration (a few weeks) and lacked professional quality (von Danckelmann, 1878). The four stations were situated close to Lambaréné, Booué, Achoucka, and Lopé. However, the data collected still holds significance. In Lopé, it remained cloudy during the dry season and July 1875 saw no rainfall. A strong westerly wind, almost everyday, was observed in Lopé during the evenings and nights of the dry season.

Although standardisation of the observations was not prevalent, these early 19th-century records still provide insight into the meteorological conditions experienced in WEA during the extended dry season. A more specific view on LLCC will be given in the next section.

2.4. Genesis and lysis of low-level clouds

Currently, there is no conceptual model for low-level clouds over western equatorial Africa. Previous research has been focused on the genesis and lysis of low-level clouds over southern West Africa (2.5–12.5°N and 10°W–10°E, van der Linden et al., 2015). First, van der Linden et al. (2015) constructed a climatology of low-level clouds in SWA during the rainy monsoon season based on synoptic weather station data and satellite data from the Meteosat Second Generation (MSG). The climatic data suggests that the area with numerous low-level stratiform clouds start to form daily to the South of 6-7°N across the ocean during sunset (around 1800 UTC). Following this, the clouds will proceed to expand inland and will reach their furthest extent northward at 10-11°N, around 3 to 4 hours after sunrise. After 1000 UTC, the stratus layer disperses into fair-weather cumulus clouds. Stratus clouds are primarily found in regions around Cape Palmas, the Ivory Coast, and the windward sides of the Mampong Range in Ghana and the Oshogbo Hills in Nigeria. There are also inconsistencies between the differently processed MSG data at night, such as the satellite application facilities in support to nowcasting and very short range forecasting (SAFNWC) encounters difficulties detecting low-level clouds, which are occasionally missclassified as cloud-free (van der Linden et al., 2015).

Furthermore, Dione et al. 2018 states that the nocturnal low-level jet (NLLJ) and the inflow of cold air masses propagating northwards from the coast of the Gulf of Guinea are frequently observed. The NLLJ, excluding periods of precipitation, is linked with low-level

stratus clouds. Stratus clouds usually build up between 2200 and 0600 UTC at the core height of the jet.

Adler et al. (2017) emphasise the crucial role of cooling in the atmospheric boundary layer for reaching saturation prior to LLCC formation, with specific humidity changes playing a minor role. Heat budget analysises show that horizontal cold air advection, radiative flux divergence and sensible heat flux divergence, especially in the presence of a low-level jet, contribute significantly to the cooling prior to LLCC formation. The results from Adler et al. (2019) contribute to the development of a conceptual model for understanding LLCC formation, maintenance and dissipation over southern West Africa.

The conceptual model developed by Lohou et al. (2020) includes four distinct phases, organised from sunset to the morning after sunrise based on the observational campaign Dynamics-Aerosol-Chemistry-Clouds Interactions in West Africa (DACCIWA). The first phase is the stable phase with a surface inversion, during which the increase in relative humidity (RH) occurs both through cooling and through a smaller increase in specific humidity (Adler et al., 2019). In the second phase, known as the jet phase, the nocturnal low-level jet sets in and the relative humidity continues to increase. At the beginning of the second phase as the maritime air reaches the observation site, the specific humidity decreases, thus minimizing the RH increase case by radiative cooling (Adler et al., 2019). In the third phase, called the stratus phase, the low-level stratus clouds begin to form, which persist until sunrise. The fourth phase is the convective phase, which begins at sunrise. The cloud base rises and the stratus breaks up into cumuliform clouds.

It is questionable to what extent this model can be applied in Gabon. Compared to SWA, WEA is more hilly, with the elevated terrain of the Chaillu mountains reaching up to 1000 m.a.s.l. (see section 2.1) and has a drier, more stable atmosphere as we are in the long dry season. The next section will discuss some factors which likely govern the life-cycle of low-level clouds in WEA.

2.5. Processes contributing to the genesis and lysis of low-level clouds in western Equatorial Africa

At present, one can only speculate about what leads to the formation and dissipation of low-level clouds in WEA. One open question is the source of the moisture for LLCC formation. The moisture may be advected eastwards into the continent from the South Atlantic at lower levels. Another possibility is the transport of moist air masses from

the Congo Basin to WEA. Advection occurs via the easterly winds, while entrainment of moisture occurs during the day via the lowest layers of the middle troposphere into the boundary layer. Outflow from convective systems that pass over the extreme northeast of Gabon in July and August and move towards the northwest could also be a source of moisture over WEA. In addition, rainfall from the east could increase humidity in WEA. As precipitation in the dry season is very rare in the south of Gabon, this applies mainly to the north of Gabon (Maloba Makanga, 2010).

Radiative cooling is also a crucial factor in the formation of LLCC (Lohou et al., 2020). The strength of the radiation depends on the temperature of the clouds (Viúdez-Mora et al., 2015). Due to the orographic conditions in WEA, we are situated at higher altitudes, resulting in lower temperatures. The colder temperatures can lead to a reduction in radiative cooling at the cloud top. This would ultimately lead to a reduction in LLCC formation via radiative cooling. Mixing with colder air is another important factor that can shape the formation of LLCC (Bretherton, 1997). This can result in additional cooling, which in turn reduces the saturation capacity.

Due to the topography, it is also possible to assume another effect. As westerly winds dominate in the lower levels (see Fig. 2.2), maritime air masses are advected along the windward slope of the Chaillu mountains. This slope can lead to cloud formation because of orographic uplift and the resulting cooling of the air masses (Q. Jiang, 2003).

Furthermore, there are various causes for the lysis of the LLCC. Precipitation that occurs in the north can cause a decrease in humidity. Drier air masses in the mid-troposphere can cause lower humidity in the lowest levels due to boundary layer mixing (Bretherton, 1997). Daytime convection breaks up the cloud deck. The resulting break-up leads to increased solar radiation at the surface, further increases convection, resulting in a positive feedback.

Another factor that can lead to a drying of the atmosphere is turbulence. A stronger horizontal wind can cause increased turbulence, resulting in stronger vertical mixing and subsequent dryness. Further, warm air mixture enhances saturation capacity, resulting in quicker evaporation within LLCC. Subsidence due to the Walker-circulation also leads to a reduction in humidity near the ground, as higher, typically drier air reaches the ground and thus promotes the dissipation of clouds (Cook and Vizy, 2016, Bjerknes, 1969).

Orographic features can also play a key role in cloud dissipation, as they do in cloud formation. Cloud formation takes place on the windward slope, however, an occurrence of foehn effect can lead to cloud dissipation on the leeward side (Yoshino, 1981).

Foehn occurs when dry air descends on the leeward side of mountainous terrain. Due to adiabatic warming during descent, the temperature increases. Foehn effects remain a topic of research due to their lack of full understanding. Furthermore, foehn occurs heterogeneously and to varying degrees in different locations. Dommo et al. (2018) have examined the Foehn effect as a potential contributor to cloudless or less cloudy conditions east of the Chaillu mountains.

A first overview of the low-level clouds in WEA has been published by Dommo et al. (2018). They aim to provide an introductory account of LLCC in WEA from June to September, together with an assessment of the associated atmospheric and sea-surface conditions. Using two satellite datasets, synoptic weather observations, European Centre for Medium-Range Weather Forecasts interim reanalysis (ERA-interim, Dee et al., 2011) data and sea surface temperature observations, this study presents evidence that LLCC is widespread in the region, primarily consisting of stratiform clouds, with a higher occurrence rate in Gabon and southern RC. The study highlights the occurrence of a foehn effect (as previously mentioned), which leads to a fast dissipation of LLCC towards the east. The diurnal cycle of LLCC is shaped by topography. Coastal plains and valleys facing the ocean tend to have more clouds at shortly before sunrise, whereas windward slopes and plateaus reach a higher amplitude and peak around some hours after sunrise. Additionally, the study notes a marked north-south sea surface temperature gradient and lower temperatures off the Gabonese coast, which correlates with significant cloud cover. The diurnal LLCC dynamics vary from those in southern West Africa, exhibiting notable variations in amplitude and phase attributed to intricate topography. The study highlights constraints in precisely depicting LLCC diurnal patterns in coastal plains, given disparities in data sets. It stresses the significance of additional case studies and even in-situ measurements to tackle these concerns.

Low-level stratiform clouds typically form in the eastern basin of subtropical oceans, where the sea surface temperature is low and the boundary layer is stable with an inversion (Klein and Hartmann, 1993, Eastman and Warren, 2014). Such clouds are commonly observed near arid coastal areas, like those found in Namibia (Cermak, 2012). The annual cycle of low-level clouds is linked to the annual stability cycle, and both diurnal cycles display a peak in the morning after sunrise (Eastman and Warren, 2014).

2.6. Observational approaches to understand low-level clouds

Observations are utilised to comprehend the various processes that result in the formation of stratiform clouds. Initial impressions of conditions in WEA are provided by Danckelmann's (1878) observations. Nevertheless, systematic and continuous measurements are essential to acquire a more extensive understanding of low-level clouds.

For this reason, weather stations operated by most weather services or air traffic control are ideal. Synoptic weather stations provide weather data collected from measuring instruments and visual observations every three hours. The regularity of the measurement interval is beneficial. Formatting adheres to conventional academic standards, maintaining formality and clarity throughout the text (WMO, 2019b). Different platforms offer this data, but some require decoding and converting for usability. The Integrated Surface Database (ISD, Smith et al., 2011) is one such platform, discussed in further detail in the Data and Methods chapter. Measuring stations are commonly situated at airports and other meteorological and climatic points of significance. In Gabon, there is a dearth of such stations. In fact, the number of measuring stations in this country is exceptionally low.

To gain a deeper understanding of low-level clouds and their diurnal cycle within the long dry season, additional components must be analysed besides Dommo et al.'s study (2018). To establish a more reliable climatology of low-level clouds, it is necessary to explore a wider range of synoptic station data and extend the period beyond 2008 when the Extended Edited Synoptic Cloud Reports Archive from Ships and Land Stations Over the Globe (EECRA, Hahn and Warren, 1999) ends. In order to enhance the comprehensiveness of the climatology based on stations, it is recommended to incorporate databases including the Integrated Surface Database (ISD, Smith et al., 2011), Met Office Integrated Data Archive System (MIDAS, MetOffice, 2012), and the synoptic weather station data obtained from the African Monsoon Multidisciplinary Analyses (AMMA, 2002) project.

Another, even sparser, observational dataset is upper-air data. Upper-air observations can be categorised into two methods: observations using a pilot balloon (PiBal) and Radiosonde (RaSo). PiBal measurements record horizontal wind at various levels, as well as the base height of clouds if present. A balloon filled with helium or hydrogen is used for this method. The average rate of ascent is determined by the updraft force acting on the balloon while it is in the atmosphere. Altitude can be assessed by observing the ascent speed, and theodolites (from a sufficient distance) can be used to determine horizontal repositioning. By taking these measurements at two different altitude levels, the horizontal

velocity can be calculated. Once the balloon vanishes into a cloud, determining its position becomes impossible. Nevertheless, the height of the cloud base can be ascertained.

Alternatively, radiosondes can be used for more advanced observations. This approach also employs a balloon filled with helium or hydrogen, which carries a measuring unit that records temperature, humidity, and pressure (Fletcher, 2023). Additionally, the radiosonde can utilise GPS capabilities to determine its own location. The recorded data is transmitted to the surface using radio waves via a transmission unit. Radio soundings serve as crucial instruments for atmospheric measurements, and their data is assimilated into numerous operational weather models of most of national weather services to achieve a more precise state of the atmosphere. However, radiosondes necessitate additional equipment to receive data and are notably more expensive. Depending on the type of balloon used, radiosondes ascend into the stratosphere and eventually burst at a certain altitude when the balloon becomes too stretched. Databases housing radiosonde measurements include the Upper Air Database (UADB, Research Data Archive and Information Systems Laboratory, 2014) of the National Centre for Atmospheric Research (NCAR) and the Integrated Global Radiosonde Archive (IGRA, Durre et al., 2016).

Another perspective is provided by the space-borne satellite viewpoint of low-level clouds. Such satellites include both geo-stationary and non-geo-stationary satellites that can observe the Earth. Geo-stationary satellites are particularly useful for low-level cloud observations because they provide continuous observation from the same point of view, which thereby makes the comparison between different points in time more straightforward. The drawback is that they are located at a very large distance from the Earth (about 35,000 kilometres), why a high resolution of observations is challenging.. Even with excellent optics, the most precise observations possess a resolution of just 2-3 kilometres. Currently, geo-stationary satellites mostly employs passive sensors (EUMETSAT, 2004). With the launch of the Meteosat Third Generation in December 2022, new instruments and improved satellite retrieval resolution will soon be accessible, alongside an active sounder which provides a vertical insight into the atmosphere (Holmlund et al., 2021). In addition to geostationary satellites, there are also non-geostationary satellites, which often are polar orbiting. Due to their closer proximity to the Earth, polar-orbiting, sun-synchronous satellites are easier to use with active measuring instruments, as the reflection of a signal can be better assigned to a specific location and altitude, and can even provide vertical profiles of certain parameters of the atmosphere (NASA, 2011, national d'études spatiales - CNES, 2003). One disadvantage of non-geostationary satellites is their movement relative

to Earth's surface. This hinders the ability to measure specific areas continuously, as only periodic retrievals are possible. In comparison, geostationary satellites offer a better temporal and horizontal resolution of the Earth's surface. On the other hand, sun-synchronous satellites provide higher horizontal and vertical spatial resolution.

All collected observational data can be condensed and processed into reanalysis data, which are models that utilize data assimilation tools to produce hindcasts. One of the most advanced and widely recognized reanalysis datasets is the European Centre for Medium-Range Weather Forecasts (ECMWF) reanalysis generation five (ERA5, Hersbach et al., 2020), which was developed by Copernicus Climate Change Service and produced by ECMWF. Reanalysis data provides a comprehensive view of the atmosphere, enabling a realistic representation by integrating measurements.

To better map the Earth, various data types are available, ranging from synoptic station to upper-air and space-borne observations, alongside reanalysis data, which are useful in mapping the atmosphere. The individual measurement methods offer their respective advantages and disadvantages in terms of accuracy and coverage and must therefore always be placed in context.

2.7. Simulating the Earth's atmosphere and low-level clouds

Simulating low-level clouds in numerical weather prediction (NWP) models is another approach to understanding the processes of formation, persistence and dissipation of low-level clouds. These clouds, which are a significant uncertainty in climate models' radiation budgets (Roehrig et al., 2013, Cheng and Xu, 2015), do have a considerable impact on the bias of the radiation budgets (Wang, 2013). Climate projections have highlighted a significant variance in the representation of parameters such as low-level clouds (J. H. Jiang et al., 2012). A comparison of Coupled Model Intercomparison Project phase 3 (CMIP3) with phase 5 (CMIP5) indicates little progress in low-level cloud modelling within climate models (Lauer and Hamilton, 2013). Hannak et al. (2017) showed that a large part of the model spread of low-level clouds depends on the different subgrid cloud schemes. Diurnal trends highlight significant issues in the vertical transfer of heat and moisture. Further, clouds are highly sensitive to modifications in the atmosphere's conditions, making them challenging to predict in a chaotic system like the atmosphere (Bony et al., 2015). They also depend on many different parameters and processes. Further, CMIP5 models still do

not properly represent low-levels clouds, and further investigation is suggested in this regard (Roehrig et al., 2013).

It is not feasible to simulate and replicate all processes in NWP. One reason is that there exist processes which are not properly understood. Cloud microphysics processes serve as a good example, as it remains uncertain how hydrometeors grow and in what circumstances. Furthermore, the genesis of the nuclei that form hydrometeors is not fully understood and remains under investigation (Lohmann et al., 2016). A second reason for poor model performance is that processes cannot be resolved at the smallest scale because the computing power is not available. A comprehensive global weather model contains millions of grid points when coarsely resolved. As the model becomes finer, the demand for computing power increases, potentially reaching billions or trillions of grid points, where numerical processes must be resolved. Attempts have always been made to increase the resolution of weather and climate models. Computing capacities increase with time, however, so does the energy consumption of the supercomputers (Kimura, 2002, Shuman, 1989). There are methods to decrease energy usage, such as the implementation of accelerators, specifically GPUs, in NWPs to forecast weather and climate conditions (Michalakes and Vachharajani, 2008). The initial weather modelling technique was introduced by Richardson (1922). Presently, the resolution is remarkably high. The operational global Integrated Forecast System (IFS) model of ECMWF has a horizontal resolution of 9 km. Due to the fact that many processes are not resolvable with such resolution, parameterisations become necessary. Parameterisations are utilised to simulate processes that are physically and dynamically unresolved. A range of approaches exists for this.

For instance, a physical process may be computed on a sub-grid level and then extrapolated to a larger scale (Stensrud, 2009). It is also feasible to simulate subgrid processes by utilizing parameters present on the coarser grid. This includes simulating additional exchange processes between grid cells that would otherwise be ignored. Additionally, statistical measuring methods can generate parameterisations that represent a statistical mean or simulate exchange process functions. The realm of parameterisations is extensive, and any unmodelled processes are attempted to be parameterised. One important parameterisation is the convection. As these parameterisations can never correspond perfectly to actual conditions, they are always only approximations of an imitated process.

There are various factors contributing to cloud formation, with a particular emphasis on LLCC. Temperature and humidity are critical in the condensation process, and their

levels determine whether or not clouds will form. Lack of water vapour saturation leads to no cloud formation, although a cloud could still exist on a sub-grid level if there is no saturation since temperature and humidity are distributed non-uniformly within the grid. The degree of inhomogeneity in turn depends on other factors such as turbulence and convection, which also play a role in the parameterisation of clouds. Low-level clouds have been modelled in a range of studies. For instance, researchers have attempted to examine how various boundary layer schemes impact the formation of low-level clouds and their subsequent effects (Neggers, 2015). One option is to concentrate on convection and its impact on the development and dispersal of low-level clouds. Convection can be addressed explicitly in a non-hydrostatic model or parameterised. Various methods are available to simulate convection, depending on the NWP model. The Tiedtke/Bechtold scheme (Tiedtke, 1989, Bechtold et al., 2008) is widely utilised for parameterising convection on coarse grids, in cases where convection cannot be resolved. It is based on three different types of convection: deep, mid-level, and shallow convection. Depending on the strength of the convection driving factors, only one of the three convection parameterizations becomes active. The scheme will be explained deeper in chapter 5.

2.8. Overview

In summary, it can be concluded that numerous factors contribute to the formation, persistence, and dissipation of low-level clouds. The objective of this research is to determine the extent to which specific processes affect the LLCC in WEA. It is essential to establish a solid database foundation for low-level clouds in WEA to obtain a comprehensive understanding of their climatology. Although some explanation has been given for low-level clouds, it remains difficult to specify which processes contribute to the formation and dissolution of clouds, and how these factors operate. Small-scale modelling has not yet been conducted to understand these processes in WEA. It is necessary to use NWP to gain a better understanding of genesis and lysis, as measurements do not contain as comprehensive information as modelling data. The following chapter will explain this in more detail.

3. Research Questions

The preceding chapter provided an overview of contemporary research on low-level clouds in Western Equatorial Africa. Dommo et al. (2018) documented the occurrence of low-level clouds in this region and outlined additional considerations arising from disparate low-level cloud datasets like the Geoprof product (van der Linden et al., 2015). Employing multiple databases can reduce potential gaps in the EECRA data collection and can extend the time period of the research, earlier in time and until today as explained in chapter 2.

Low-level clouds are detected not just through station data but also via radiosondes. The accurate in-situ radiosondes measurements in the atmosphere, including temperature, humidity, pressure, and wind, allow radiosondes for an assessement of the vertical profiles. Nevertheless, regarding the scarcity of radiosonde measurements, they are of limited value in WEA. Using radiosondes, various properties and assumptions can be selectively tested and confirmed.

There is a substantial amount of satellite data available on clouds, too. The Meteosat Second Generation (MSG, EUMETSAT, 2004) geostationary satellites offer uninterrupted data from 0°E. As noted previously, the SAFNWC cloud classification product was utilised to examine low-level clouds in the WEA region (Dommo et al., 2018). Nonetheless, this approach encounters challenges in identifying low-level clouds (van der Linden et al., 2015). Nevertheless, recognition of low-level cloud formations can be achieved by using the unprocessed satellite data and applying predetermined thresholds for specific channels of the satellite's observing system (van der Linden et al., 2015, Schrage and Fink, 2012), which thresholds are adapted from the processing schemes established by Lensky and Rosenfeld (2008). This technique enables a more precise identification of low-level clouds compared to SAFNWC (van der Linden et al., 2015).

Under these circumstances, the following research questions arise:

RQ1: How can a comprehensive climatology of low-level clouds be developed?
Specifically, in this context, the following questions emerge:

- **RQ1a:** What are the factors contributing to cloud formation from different observational perspectives in western Equatorial Africa during the long dry season between June and September?
- **RQ1b:** What is the low-level cloud diurnal cycle in western Equatorial Africa during the long dry season between June and September?
- **RQ1c:** Do we expect different climatologies from different observational perspectives?

Low-level cloud studies can also be carried out through modelling. The modelling of low-level clouds during the dry season from June to September in WEA is yet to be explored. The previous chapter includes descriptions of various techniques available for this research. As detailed in the preceding Chapter, it is possible to consider the influence of convective parameterisation on cloud formation, and thereby better understand the mechanism of low-level cloud formation. To carry out this investigation, we employ the Icosahedral Nonhydrostatic Numerical Weather Prediction model (ICON, Zängl et al., 2015), utilizing parameterised convection, explicit deep with parameterised shallow convection and explicit convection.

Consequently, the following research questions arises:

RQ2: How do the different approaches concerning convection affect the formation and dissipation of low-level clouds?
Specifically, the following questions arise:

- **RQ2a:** How does the parameterisation of convection impact atmospheric moisture and its role in cloud formation and dissolution?
- **RQ2b:** What is the effect of shallow convection parameterisation on moisture levels in the model?
- **RQ2c:** Which fluxes, both sensible and latent, are observed on the ground in the context of parameterised, shallow convection or explicit convection only?

The following section outlines the utilized data and methods used to address these questions. This will bring us closer to counter the challenges understanding low-level clouds and, hopefully, aid in improving their representation in models in western Equatorial Africa during the long dry season.

Part II.

Data and Methods

4. Observations - station, upper-air, and satellite data

This chapter presents the observations utilised in this thesis, drawn from four different observations data sources, some of which are historical. The surface observations underwent a homogenisation test to rectify any data biases (Aellig et al., 2022). Likewise, the thesis relied on two sources of upper air observations, pilot balloon (PiBal) and radiosondes (RaSo). Satellite observations were obtained from three different satellites across two data sets for this thesis. Two different statistical techniques were used to cross-compare surface-based and space-borne satellite observations.

4.1. Synoptic surface observations

Cloud observations on a synoptic scale are a widely established global practice, often conducted at airports to ensure weather condition monitoring and to provide alerts to approaching airplanes in potentially hazardous situations, as required for safety. These records have been recorded for over a century. In Gabon, the source AMMA (African Monsoon Multidisciplinary Analysis, AMMA, 2002) indicates that the first cloud observations date back to 1931. The following observations have been accumulated over time and exist in both physical and digital formats, stored by diverse institutions on varying platforms and adhering to various standards. To conduct this research, we utilised four distinct datasets, arranged in descending order of reliability.

4.1.1. EECRA

The "Extended Edited Synoptic Cloud Reports Archive from Ships and Land Stations Over the Globe" (EECRA, Hahn and Warren, 1999) is the most dependable dataset. It predominantly includes cloud observations and is managed by the National Center for Atmospheric Research (NCAR). The synoptic code from the WMO (WMO, 2019b) is

followed by the dataset. The dataset includes data from 1952 to 2009, with a decrease in data density from 2000 onwards. The developers of the EECRA dataset performed quality control.

The prominent advantages of EECRA are its worldwide observation coverage with lengthy observations, unobscured low-level cloud observations and the availability of other meteorological parameters to verify cloud observations. However, its limitations include a lack of heterogeneity over land and sea, hindrance of low-level cloud observation by higher clouds, and inadequate quantitative information on cloud optical depths (Hahn and Warren, 1999). Due to its robust quality control and consistency checks, the EECRA dataset has been classified as the most dependable.

4.1.2. ISD

An additional dataset employed in this thesis is the Integrated Surface Database (ISD), which is administered by the National Center for Environmental Information (NCEI, Smith et al., 2011). The ISD predates the EECRA by First observations in Gabon date back to 1937, which is much earlier than those from EECRA (Hahn and Warren, 1999). Additionally, the ISD is subjected to quality control measures. The Integrated Surface Database (ISD) comprises more than just synoptic observations as defined by the World Meteorological Organization (WMO) (WMO, 2019b). It also includes hourly and half-hourly Meteorological Aerodrome Reports (METAR) from different stations. Regrettably, due to inconsistencies in the reports (e.g. cloud cover is reported in different scales instead of octas), this data was unsuitable for further analysis in the thesis. Unfortunately, a significant number of cloud observations could not be utilized from 2013 onwards due to an error in data processing. This error resulted in the absence of several values.

4.1.3. MIDAS

The Met Office Integrated Data Archive System (MIDAS) is a database comprising synoptic weather reports, unlike the ISD, which includes METAR data. Global observations within the MIDAS database date back to 1853 (MetOffice, 2012). Notably, since 2013, MIDAS has had no errors, which affords it an advantage in filling gaps within the ISD database. Unfortunately, MIDAS data is only available from 1970 for most of the stations of interest in WEA.

4.1.4. AMMA

The AMMA database holds the oldest data in WEA (Fleury et al., 2011), dating back to 1931. However, most data from before 1980 has not undergone proper quality checks and does not follow standard meteorological reporting protocols. Many old records are still being digitised. Unfortunately, it was not possible to obtain digital copies of the ancient cloud information for this study from the WEA at the time of writing. Due to the absence of a quality check and discrepancies between the AMMA dataset and the other three datasets, we did not utilize the AMMA dataset prior to 1980 for further analysis. Despite its potential to considerably expand our timeline, we deemed it unsuitable for use before 1980.

4.1.5. Homogenization of the Surface Observations

The use of different standards for measuring time across countries and over a long time period necessitated the implementation of homogeneity tests to ensure data accuracy. We employed the Standard Normal Homogeneity Test (SNHT; Alexandersson and Moberg, 1997) on the dataset and further conducted a visual inspection to detect breaking points. After analysis, we identified and corrected 7 breaking points across 6 stations (Aellig et al., 2022). Bitam (1978 and 2013), Lambaréné (2015), Mitzic (1998), Moanda (1996), Mouila (2010), and Tchibanga (1985) are the stations whose data is utilized for the climatology of low-level clouds.

4.2. Upper-air Data

Upper air data include two different types of observations, radiosondes and pilot balloons. Radiosondes are attached to balloons filled with a gas (helium or hydrogen) that is lighter than ambient air. Radiosondes measure temperature, humidity, pressure and their GPS position. The position can be used to determine the wind. The data is sent back via radio signals to a receiver on the ground.

A pilot balloon is only measured from the ground via the eye. Therefore, only the wind direction can be determined. From the calculated updraft speed and time, the position can be determined using a theodolite. Pilot balloons need eye contact to determine their position. It can therefore only be launched in daylight and provides information as long

as it is not in a cloud. In addition, the cloud base height can be determined at a time when visual contact is lost.

Upper-air data is limited in the WEA region. Pilot balloons and radiosondes are launched only from three locations in Gabon: Libreville, Franceville, and Port-Gentil. Presently, only one launch is conducted per day at the Libreville airport in Gabon. However, it appears that in Pointe-Noire and Ouesso, in the Republic of Congo, radiosondes are launched during our case study period.

4.2.1. Integrated Global Radiosonde Archive - IGRA

The integrated Global Radiosonde Archive version 2.0 (IGRA) is an upper-air data base including radiosondes pilot balloons observation from the whole world (Durre et al., 2016). The dataset is qualitiy controlled and based on 30 different sources (Durre et al., 2016). The IGRA data base goes from 1905 to today.

4.2.2. NCAR Upper Air Database - UADB

The National Center for Atmospheric Research (NCAR) host the Upper Air Database (UADB) consisting radiosonde and pilot balloon observations (Research Data Archive and Information Systems Laboratory, 2014). It bases on 50 different sources and is quality controlled. The dataset includes the variables geopotential height, temperature, humidity, wind. Earliest observation in the region of interest are dated back to 1957. The dataset was added to the already existing IGRA to fill data gaps and check inconsistencies.

4.3. Satellite data

Satellites play a crucial role in monitoring the Earth's atmosphere. There are typically two types of Earth observing satellites: geostationary and non-geostationary. Geostationary satellites offer spatial and temporal observations of consistent parts of the earth as they remain stationary in orbit. On the other hand, there are earth cycling satellites which can measure much more exact because they are much closer to the Earth.

4.3.1. Meteosat Second Generation - MSG

The Meteosat Second Generation (MSG) consortium is a partnership between the European Space Agency (ESA) and the European Organisation for the Exploitation of Meteorological

Satellites (EUMETSAT, 2004). At its core, the satellite provides the Spinning Enhanced Visible and InfraRed Imager (SEVIRI) (Schmid, 2000). SEVIRI measures in 12 distinct spectral channels, eight of which are located in the infrared spectrum, and a high-resolution visible (HRV) channel with a wide spectrum, while there are three more in the visible spectrum (see tab. 4.3). The data collected by SEVIRI satellite has been accessible since 2004. The satellite is positioned at 0° longitude and 0° latitude, at an altitude of about 36'000 km above sea level. The resolution in the tropics in Gabon (at Nadir) is approximately 3 km x 3 km.

The channels measured by SEVIRI offer insight into the atmosphere of the Earth regarding its temperature, aerosols, and moisture. Based on the measure of radiation, the reflectance is calculated using the solar reflectance term in the following manner:

$$\rho_\lambda = \frac{B_\lambda}{\mu_0 * F_0(\lambda)}, \tag{4.1}$$

with B_λ as physical spectral radiance in mW/m^2, μ_0 as the cosine of the solar zenith angle, and $F_0(\lambda)$ as the extraterrestrial solar flux at wavelength λ in $\frac{mW}{m^2 * ster * cm^{-1}}$ listed in tab. 4.1(EUMETSAT, 2012) .

Table 4.1.: Calibation factor for the extraterrestrial solar flux at the equinox for certain wavelengths (EUMETSAT, 2012)

Channel ID	MSG1	MSG2
VIS 0.6	20.76	20.76
VIS 0.8	23.24	23.30
VIS 1.6	19.85	19.73
VIS 3.9	4.92	4.92

The brightness temperature is calculated with the inverse Planck function:

$$T = \frac{(\frac{C_2 * \nu_c}{ln(\frac{C_1 * \nu_c^3}{B} + 1)} - b)}{A}, \tag{4.2}$$

with B as the physical spectral radiance, constant C_1 as $1.19104 * 10^{-5} mW m^{-2} sr^{-1}$, constant C_2 as $1.43877 K(cm^{-1})^{-1}$, ν_c as the central wave number and a and b as coefficient depending on the channel. The central wave number ν_c and the constants a and b are from the look up table 4.2 from EUMETSAT (2012).

Based on this information, a variety of phenomena can be identified. Rosenfeld and Lensky (2008) proposed qualitative schemes to represent different phenomena in the

Table 4.2.: Look up table to calculate brightness temperature for the 8 infrared channels measured by SEVIRI (EUMETSAT, 2012)

Channel ID	ν_C	A	B
IR 3.9	2567.330	0.9956	3.410
IR 6.2	1598.103	0.9962	2.218
IR 7.3	1362.081	0.9991	0.478
IR 8.7	1149.069	0.9996	0.179
IR 9.7	1034.343	0.9999	0.060
IR 10.8	930.647	0.9983	0.625
IR 12.0	839.660	0.9988	0.397
IR 12.0	752.387	0.9981	0.578

Table 4.3.: Spectral channels (band widths) of the SEVIRI instrument (Schmid, 2000)

Channel ID	Spectral Band [µm]		Band
HRV	0.37	1.25	Visible and near IR
VIS 0.6	0.56	0.71	
VIS 0.8	0.74	0.88	
NIR 1.6	1.50	1.78	
IR 3.9	3.48	4.36	Window
IR 8.7	8.30	9.10	
IR 10.8	9.80	11.80	
IR 12.0	11.00	13.00	
IR 6.2	5.35	7.15	Water vapour
IR 7.3	6.85	7.85	
IR 9.7	9.38	9.94	Ozone
IR 13.4	12.40	14.40	CO

earth's atmosphere using channel combinations to produce RGB images. Among them are the night-microphysical scheme (NMS) and the day-microphysical scheme (DMS), which are employed in this thesis.

4.3.2. Day-microphysical scheme - DMS

The DMS is based on three channels, namely VIS0.8, IR3.9r, and IR10.8 (see tab. 4.3). The reflectance of VIS0.8 is a significant indicator of both cloud water and ice and the cloud optical depth, which are marked in red. The reflectance of solar channel IR3.9r serves as an indicator of particle phase and size, depicted in green. Due to its spectral proximity to the visible range, this parameter can also be applied beyond just measuring

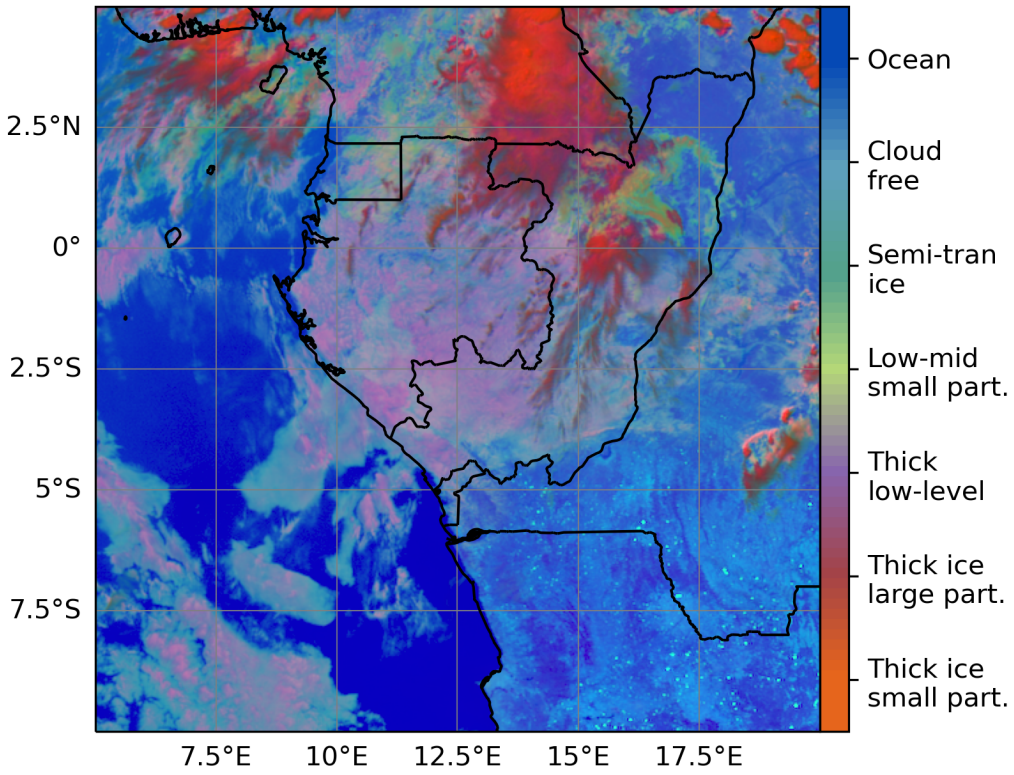

Figure 4.1.: Day-microphysical scheme adabted from Lensky and Rosenfeld (2008) for the 17th July 2018 at 1300 UTC using SEVIRI from the MSG. Categorization of adapted from EUMETSAT (2012).

brightness temperature. Additionally, the height of the highest emitting entity is denoted by the brightness temperature in channel IR10.8, shown in blue. In combination, their colour represents clouds transitioning from precipitating (pink) large droplets to non-precipitating (white) small droplets (Lensky and Rosenfeld, 2008). Yellowish appearing colours are indicative of supercooled water clouds due to the lower temperature modulated in blue. Clouds with cold and thick tops appear red due to the presence of large ice particles, whereas cloud tops with smaller ice particles tend to appear orange. Figure 4.1 provides an example. The colours in the colour palette signify cloud classifications from EUMETSAT (2012). The intermediate spectra result from a basic interpolation in the RGB spectrum.

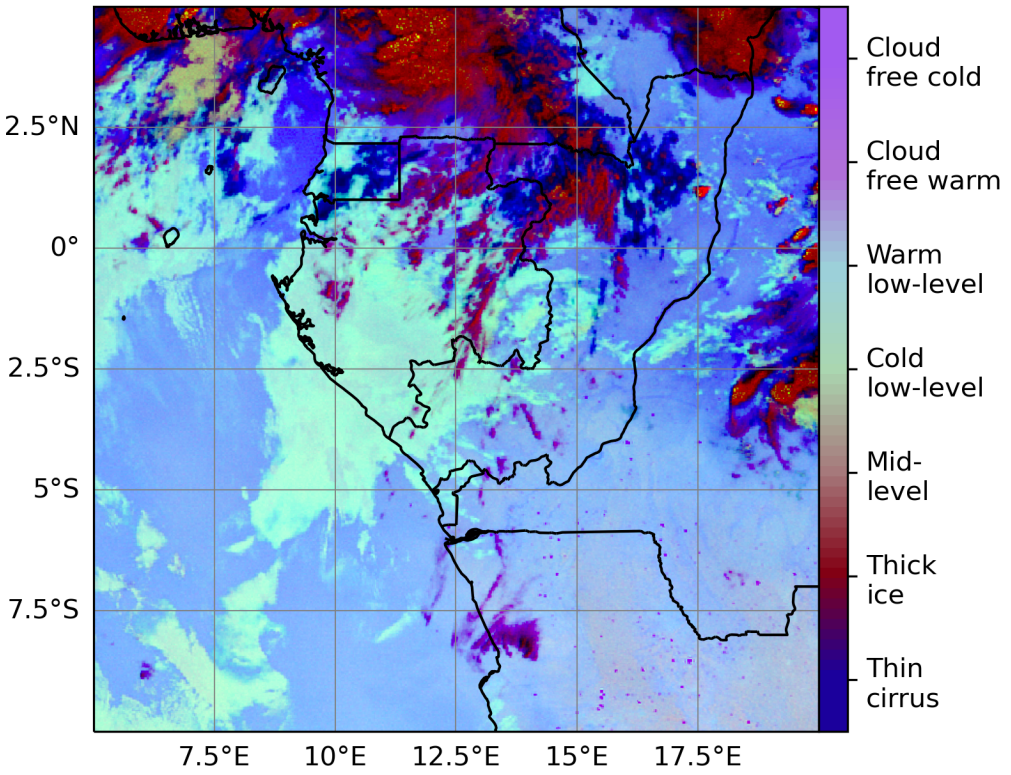

Figure 4.2.: Night-microphysical scheme adabted from Lensky and Rosenfeld (2008) for the 17th July 2018 at 1800 UTC using SEVIRI from the MSG. Categorization of adapted from EUMETSAT (2012).

4.3.3. Night-microphysical scheme - NMS

The NMS does not employ reflectance-based channels as it is designed to operate during the night without shortwave radiation. An RGB image is created using three infrared channels to analyse cloud and aerosol particles in the atmosphere of the Earth. The opacity of clouds is depicted in red, which is calculated as the difference between the brightness temperatures of the IR12.0 and IR10.8 channels (Lensky and Rosenfeld, 2008). The particle size is represented by the channel difference between IR10.8 and IR3.9, and is shown in green. The brightness temperature of channel IR12.0 represents the height of the uppermost object in the Earth's atmosphere. As a representative image, see Fig. 4.2. Clouds with a high concentration of larger droplets of water and possibly precipitating have a greater green appearance. White to teal colours indicate the presence of fog or

low-level clouds. When the clouds are colder, which is more common in tropical regions at higher altitudes, they turn yellow. Deep convective clouds are characterised by a scattered red-yellow tone.

4.3.4. Low-level cloud determination of SEVIRI data

Based on these two schemes for day and night, specific thresholds are selected to ascertain the presence of LLCC at a given point on the grid, in clear or overcast sky, or atop a higher cloud that does prevent the determination of LLCC. During daylight hours, a grid box is classified as LLCC when the reflectance level of the VIS0.8 channel exceeds 25%, and the brightness temperature of IR10.8 measures above 283 K. VIS0.8 represents the water content and optical depth, while IR10.8 indicates the altitude. For the night, the temperature difference in brightness between the IR3.9 and IR10.8 channels must be greater than 2 K and the brightness temperature of the IR10.8 channel must exceed 283 K. If the temperature recorded on channel IR10.8 is less than 283 K, it is inferred that there is a higher cloud ceiling than LLCC. If the brightness temperature of channel IR10.8 is higher than 283 K and the cloud definition parameters are not fully filled, the grid box is assumed to be clear sky.

4.3.5. 2B-Geoprof-LiDAR

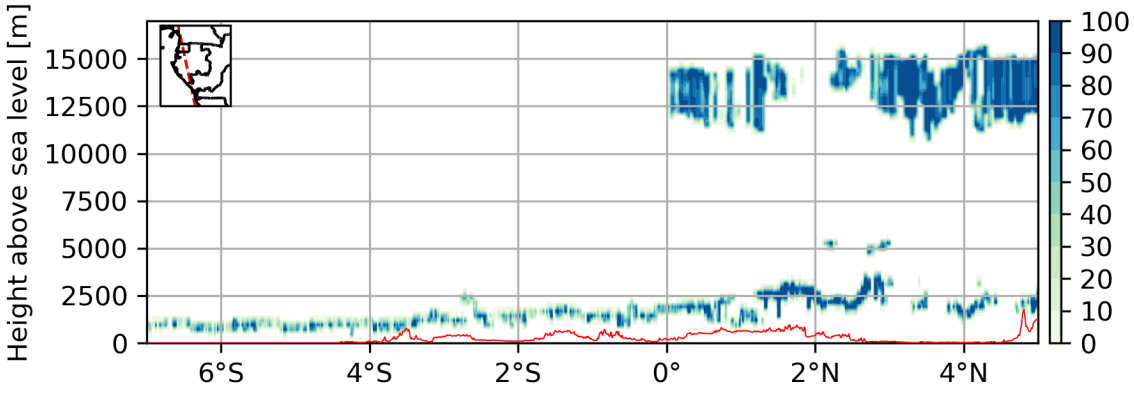

Figure 4.3.: 2B-Geoprof-LiDAR (Geoprof, Mace and Zhang, 2014) snapshot of the cloud fraction from one overpass of WEA at 1230 UTC on the 15th July 2015.

The cloud product 2B-Geoprof-LiDAR (hereafter named Geoprof) is based on observations of two different satellites. The Cooperative Institute for Research in the Atmosphere's Data Processing Center (DPC) is responsible for producing this product.

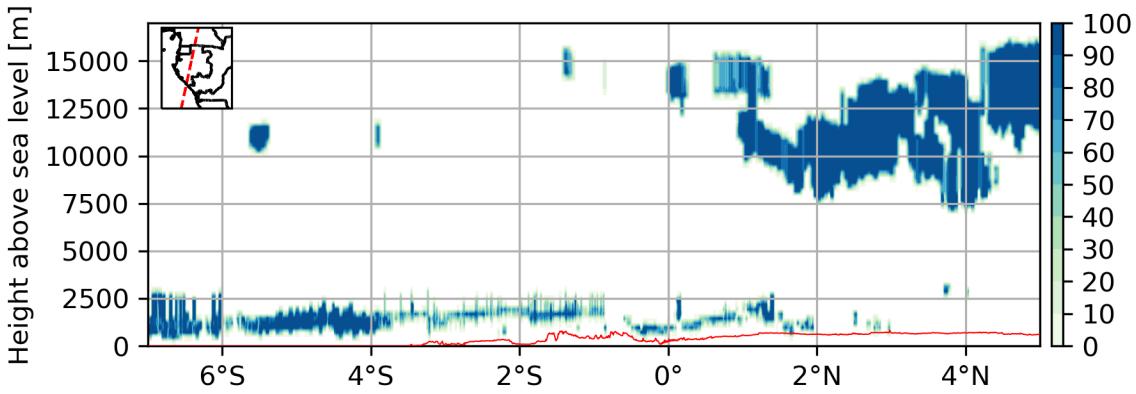

Figure 4.4.: 2B-Geoprof-LiDAR (Geoprof, Mace and Zhang, 2014) snapshot of the cloud fraction from one overpass of WEA at 0100 UTC on the 11th July 2010.

The two satellites used are CloudSat (NASA, 2003b) and Cloud-Aerosol Lidar and Infrared Pathfinder Satellite Observations (CALIPSO, national d'études spatiales - CNES, 2003). Positioned in polar orbit, the satellites are sun-synchronous and orbiting in the A-train at an altitude of 709 to 710 km above ground level. It takes 94 minutes to orbit the Earth. The repeat period, where the same path is crossed again, is 16 days.

CloudSat is a component of NASA's Earth Observing System (EOS) programme (NASA, 2003b). The satellite is equipped with the Cloud Profiling Radar (CPR) that operates at a frequency of 94 GHz to identify cloud water, ice and droplets in the atmosphere (NASA, 2003a). The CPR is approximately 1000 times more sensitive than a standard radar. It scans a swath of 25 km below it and has a 1.7 km along-track resolution, a 1.4 km cross-track resolution, and a vertical resolution of 500 meters. The vertical resolution is a major advantage provided by this satellite, as it offers insight into the profile (NASA, 2003a).

CALIPSO is a joint project by the Earth Observing System (EOS) program from NASA and the Centre Nationales d'Etudes spatiales (CNES) from France (national d'études spatiales - CNES, 2003). CALIPSO's Cloud-Aerosol Lidar with Orthogonal Polarisation (CALIOP) is an essential satellite instrument required to create the Geoprof product. The cloud-aerosol LiDAR operates at the wavelengths of 532 nm and 1064 nm respectively and have a pulse energy of 110 mJ per channel (Winker et al., 2007). The LiDAR channels have a vertical resolution range of 30 to 60 metres and an along-track resolution of 333 metres. The combined measurements from both CPR and LiDAR makes the Geoprof product comprehensive.

The cloud fraction from Geoprof opens up the vertical structure and distribution of clouds in the earth's atmosphere. An example of an overflight is shown in Fig. 4.3 for

the day around noon and in Fig. 4.4 for the night around midnight. While the CPR is able to penetrate more thick clouds and scan even below cloud decks, CALIOP is able to detect rather thin Cirrus clouds but get blocked by thicker, opaque clouds (Mace and Zhang, 2014). Geoprof data was used from 2006 to 2017. However, due to a battery incident in spring 2011, CloudSat was no longer able to take measurements at night, when no sunlight is available for the panels to run the systems (NASA, 2011). Therefore, data at night is only used from June to September in the years from 2006 to 2010. The construction of the cloud fraction algorithm in Geoprof, which is based on two satellites, is detailed in Marchand et al. (2008) and Mace et al. (2014). In this thesis the data release version P1_05 is used (Marchand and Mace, 2018).

4.4. Verification

Table 4.4.: Contingency table to validate the SEVIRI cloud occurrence by the synoptic weather station observations.

Observation / Prediction	Cloud fraction by synoptic weather station greater equal than 4 Octas	Cloud fraction by synoptic weather station smaller than 4 Octas
Cloud fraction by SEVIRI data equal or greater than 50 %	A - Hits	B - False Alarmes
Cloud fraction by SEVIRI data smaller than 50 %	C - Missed events	D - Right rejections

This section details the validation process for LLCC from the SEVIRI satellite. Consequently, an accurate point of comparison with the satellite data is required. It is essential to validate satellite data since it is often processed and diagnostic products, such as cloud fraction, make differing assumptions according to the location and time of the measurement. The low-level cloud information obtained from the synoptic weather station was used as a reference point to evaluate the LLCC from the SEVIRI satellite.

To compare the satellite data with synoptic weather stations, we considered all pixels within a 20 km radius of a station for a point-to-point comparison. This maximum distance of 20 km is recognized as the limit for identifying a LLCC, based on an assumed angle of 80° to account for clouds and a cloud base height of 2000 metres above ground level (m.a.g.l.) to still see low-level clouds (WMO, 2019a). All pixels are then multiplied by

a cosine function ranging from 0 to half pi. The function is applied in accordance with the pixel distance to the station coordinates, producing a weight that is based on the distance of the observer.

Therefore, observations directly above hold more weight than those farther away. Additionally, any data points where more than 50% of the 20 km radius is covered by higher clouds have been excluded. This was to ensure a reliable comparison by eliminating a small fraction of the measurable area around the station. Subsequently, the satellite data from SEVIRI was used to produce the percentage of low-level cloud cover at each station. Using the calculated cloud fraction obtained from the satellite, it is now possible to compare it with the cloud fraction information from the station. To make the datasets comparable, a binary classification of 'cloudy' and 'non-cloudy' weather situations was employed, which enabled the use of a contingency table (see tab. 4.4). Regarding the synoptic weather station data, an event is recorded if the reported cloud fraction is greater than or equal to 4 Octas. To determine whether the satellite data depicts cloud cover, the Receiver Operating Characteristics (ROC) method is employed to identify the optimal threshold (see next subsection).

Based on the set thresholds, the identification of a hit (A - cloudy condition ascertained by satellite and observed at the station), a false alarm (B - cloudy condition ascertained by satellite but not observed at the station), a missed event (C - non-cloudy condition ascertained by satellite but observed at the station), and a right rejection (D - non-cloudy condition determined by satellite and not observed at the station) are defined (see tab. 4.4). For later analyse the hit rate,

$$Hit\ rate = \frac{Hit}{Hits + Missed\ events} \tag{4.3}$$

and the false alarm ratio

$$False\ alarm\ ratio = \frac{False\ alarms}{Hits + False\ alarms} \tag{4.4}$$

is defined. This will be used by the ROC analyses. Finally, validation of both datasets (NMS & DMS) is achieved using the Heidke Skill Score (HSS, Heidke, 1926), with the threshold received from the ROC.

4.4.1. Receiver-Operating-Characteristic - ROC

ROC curves are a technique for determining optimal thresholds by grouping data. The objective in this instance is to establish the best LLCC threshold for defining cloudy weather from a satellite viewpoint at a station. Validation of the satellite data versus the station data can then be completed using a binary comparison of whether the situation is "cloudy" or "not cloudy". This comparison is made based on the satellite's efficiency in identifying cloudy conditions without incorrectly detecting them as such. Using the method outlined in the preceding section, the satellite dataset can ascertain the cloud fraction for a particular point in the area. The comparison is carried out using an increasing threshold value, in 12.5% increments, from 0% to 100%, to determine when a particular cloud fraction at a given point is classified as a cloudy area. At each step, the hit rate and false alarm ratio are calculated based on the contingency table (see tab. 4.4) using equations 4.3 and 4.4. A diagram displaying the ROC-curve can then be created with the false alarm ratio on the x-axis (to be kept as small as possible) and the hit rate on the y-axis (to be made as large as possible). The value with the highest hit rate, while not magnifying the false alarm rate too much, is ultimately the best threshold using this method.

4.4.2. Heidke-Skill-Score - HSS

The HSS is a measure that evaluates the accuracy of a prediction compared to a specific observation. It was developed by Paul Heidke (1926). The comparison is binary, and it tests whether an event occurred or not, as described in the contingency table (see tab. 4.4). In our case, the event is the appearance of a low-level cloud. An event is predicted when the cloud fraction determined by SEVIRI exceeds or equals the threshold determined by the ROC.

The HSS uses the measure of hits (A), false alarms (B), missed events (C), and right rejections (D) to create a skill-score. Skill scores is in the following format:

$$Skill = \frac{actual\ score - standard\ score}{perfect\ score - standard\ score} \tag{4.5}$$

This is represented in the HSS equation

$$HSS = \frac{\frac{A+D}{N} - \frac{(A+B)(A+C)+(B+D)(C+D)}{n^2}}{1 - \frac{(A+B)(A+C)+(B+D)(C+D)}{N^2}}, \tag{4.6}$$

what can be simplified to

$$HSS = \frac{2 * (A * D - B * C)}{(A + C) * (C + D) + (A + B) * (B + D)}. \tag{4.7}$$

, with A, B, C, and D from the contingency table and N as the number of comparisons done. The HSS measures the fractional improvement compared to a standard forecast and can be normalized for use with different datasets (Heidke, 1926). Negative HSS values indicate that actual skill is worse than chance, while HSS values ranging from 0 to 1 indicate actual skill is better than chance. A score of 1 denotes a perfect prediction. The HSS is used to validate the cloud fraction of the MSG dataset for every synoptic report and station. Unfortunately, it was not feasible to verify Geoprof using synoptic station data due to the absence of CloudSat and CALIPSO satellite coverage in the region of interest and the scarce overflights.

4.5. Climatology Built

Assumptions were made when constructing the diurnal cycle of LLCC during the JJAS long dry season in the region of interest. Analysis of low-level cloud information from the synoptic weather station was carried out together and then separated by cloud type. This separation allows for the identification of the dominant clouds at specific times of day. The synoptic weather station reported nine different cloud types, all of which can be found in the tab. 4.5.

Table 4.5.: Low-level cloud types reported by synoptic weather stations (WMO, 2019b)

Cloud description	Cloud number	Abbreviation
Cumulus of small vertical extent	1	Cu
Cumulus of moderate or great vertical extent	2	Cu
Cumulumnimbus without anvil	3	Cb
Stratocumulus from the spreading out of cumulus	4	Sc
Stratocumulus not from the spreading out of Cumulus	5	Sc
Stratus not accompanied by precipitation	6	St
Stratus or cumulus fractus accompanied by precipitation	7	St or Cu
Cumulus and stratocumulus at different levels	8	Sc and Cu
Cumulunimbus with anvil	9	Cb

The clouds are classified into two groups based on their stratiform or cumuliform nature. Afterward, the diurnal patterns of these groups are calculated and analysed.

Using SEVIRI data and defined thresholds to determine the occurrence of low-level clouds at each grid point (see subsec. 4.3.4), this thesis calculates the low-level cloud occurrence frequency (LCOF) to establish the climatology of LLCC in WEA during the long dry season using SEVIRI data.

The construction of the climatology of LLCC by Geoprof is quite intricate and requires more assumptions. Geoprof provides a vertical distribution of cloud fraction, but only along the satellite's path at different heights. Thus, a spatial grouping must be performed to prepare the data for quantitative analysis. Initially, the path is divided into half-degree sections along the latitude and separated into boxes every 500 metres vertically. Cloud occurrence frequency and the cloud fraction of the relevant box are calculated using the Maximum-Random-Overlap (MRO, Hogan and Illingworth, 2000) method. MRO treats continuous layers as one layer with maximum overlapping and spatially separated layers as randomly overlapping. The MRO formula is as follows:

$$C_{k,l}^{ran} = C_k^{max} + C_l^{max} - C_k^{max} * C_l^{max}, \tag{4.8}$$

where $C_{k,l}^{ran}$ is the cloud fraction of the two layers k and l, C_k^{max} the maximum cloud fraction of layer k, and C_l^{max} the maximum cloud fraction of layer l. The described methodology is applied to all contiguous layers from bottom to top. Van der Linden et al. (2015) also employed the same technique to the Geoprof data in their studies. The outcome of these approaches is a two-dimensional gridded dataset, which is based on the retrieved cloud fraction. The climatology of the clouds is created using two distinct approaches: averaging the obtained cloud fraction and the cloud occurrence frequency (COF). There, we obtained strips of cloud optical thickness and determined the mean cloud fraction along the flight paths for each strip across the area of interest.

To achieve low-level clouds on a 2D latitudinal and longitudinal grid, we combine gridded 2D cloud fraction swaths from 0 to 3000 metres using MRO and calculate the frequency of low-level cloud occurrences. This results in two 2D LCOF and cloud fraction means, one for daytime and one for nighttime.

Using the methods outlined above, we compute the diurnal cycle and the climatology of the low-level clouds based on the existing datasets. The results of the diurnal cycle analysis can be found in the Results section.

5. Numerical weather prediction - ICON

Numerical weather prediction (NWP) models are used in atmospheric science to model processes in the atmosphere for a more comprehensive understanding. There are several types of NWP models: some for weather prediction, others for climate, and some are hybrids. Despite some models being tailored for weather services, others are exclusively developed for research and sciences, or a combination of the two. NWP models are typically constructed in grids of various levels, forming a three-dimensional model of the Earth's atmosphere. Each grid point contains physical and dynamical information on the intended atmosphere state. From this starting point, the NWP is integrated forward in time with a certain time step. This integration contains two significant components of atmosphere changes in time: dynamics and physics. Advection, subsidence, and uplift constitute the dynamical integration, while condensation, radiation, convection, and various other micro- to macro-physical processes form the physical integration of an NWP model.

5.1. ICON-NWP

The Icosahedral Nonhydrostatic Numerical Weather Prediction (ICON-NWP) model, also known as ICON, is utilised in this thesis (Zängl et al., 2015). This section provides a fundamental overview of the model. The ICON model was developed by the German Weather Service (DWD) and the Max-Planck-Institute (MPI) in Hamburg, and its name derives from its icosahedral shape.

The Earth and its atmosphere are no longer represented in rectangular grid boxes as in earlier NWP models. Instead, a triangular grid is used to represent the atmosphere (Prill et al., 2022). The underlying horizontal grid of the ICON model follows the notation RnBk, which represents a grid generated from an icosahedron whose edges are initially divided into n parts (R), followed by k subsequent edge bisections (B). The overall quantity of cells in a global ICON grid, known as RnBk, can be calculated via $n_{cells} = 20 * n^2 4^k$. The circumcenters of the cells carry data for most ICON variables, with the exception of the

orthogonal normal wind. The wind is designated at the midpoints of triangle edges and measured perpendicularly. Determining the horizontal grid point spacing can be achieved using the spherical surface formula, adapted to the following equation:

$$\overline{\Delta x} = \sqrt{\frac{4R_{earth}^2\pi}{n_{cells}}} = \frac{4R_{earth}^2}{n2^k}\sqrt{\pi/5} \approx 5050/(n2^k)\ [km], \tag{5.1}$$

with R_{earth} as the radius of the Earth (Prill et al., 2022). In our case study we used $R = 3$ and $k = 7$ as the outermost domain (parent domain), resulting in a horizontal resolution of 13.2 km. For further information regarding domain-specific details, refer to section 5.2.

The ICON model allows for online nesting in an inner domain with a higher resolution. Online means that ICON calculates the inner nests at the same time as the outer parent domain. The capacity for online nesting in the inner domain is a fundamental aspect of the ICON model. It makes it possible to use the ICON model with various methodologies, including Large-Eddy-Simulations (LES), high-resolution simulations, or for idealized case studies. Furthermore, the ICON model is a non-hydrostatic model that allows for vertical movement of air parcels without requiring the pressure gradient to be balanced by gravity. This characteristic is especially vital in situations involving thunderstorms, mountainous landscapes, or locations with significant vertical motion.

As ICON is a non-hydrostatic model, it cannot necessarily be assumed that pressure levels increase monotonically with altitude (Prill et al., 2022). Therefore, an altitude staggering approach is used for the vertical grid. ICON utilizes a vertical grid structure comprising of layers with a two-dimensional layout. The model employs a Lorenz-type staggering (Herzog and Gaßmann, 2005), positioning vertical velocity at layer boundaries (half levels) and other prognostic variables at the layer centres (full levels, Prill et al., 2022). Moreover, ICON integrates a terrain-following hybrid vertical coordinate system based on height, which includes the Smooth Level Vertical (SLEVE) coordinate implementation (Schär et al., 2002, Leuenberger et al., 2010). This approach permits a speedier transitioning to level out between the upper troposphere and lower stratosphere in comparison to the conventional height-based coordinates (Schär et al., 2002). The vertical grid spacing is managed by namelist parameters, which include the quantity of levels, stretching factor, model top height, minimum layer thickness, and flat height. The stretching factor affects the thickness and distribution of the vertical levels, with the layer thickness expanding as height increases.

5.1.1. Dynamics and Prognostics

The fundamental element of the numerical weather forecasting system is the dynamical core, responsible for progressing the discrete equations governing fluid dynamics over time. As for the second primary component within ICON, tracer advection computes the advection of prognostic variables. Thereafter, the dynamical core and advection scheme are coupled with parameterisations for phenomena like convection or microphysical processes, which occur discretely and at scales too small to directly resolve in the model. The methodology and its corresponding physics parameters are detailed in subsection 5.1.2.

ICON employs the prognostic variable equations system, originally proposed by Gassmann and Herzog (2008), in conjunction with two-dimensional Lamb transformations (Zängl et al., 2015). These transformations effectively convert nonlinear horizontal momentum advection into a vector invariant form. The specified set of equations describes a two-component system comprising of dry air and all three water phases (vapour, liquid, ice). The prognostic equations are utilised to ascertain the horizontal velocity components across the triangular edges, the vertical wind component (ω), the overall air mixture density (ρ), virtual potential temperature (θ_v), and specific masses and number densities of tracers.

5.1.2. Physics parameterisations

With ICON, there are various options available to simulate unresolved processes through parameterisations and schemes. This section describes the main parameterisations and specific adaptations for tropical conditions. The Rapid Radiative Transfer Model (RRTM) radiation scheme is used in all domains (Mlawer et al., 1997, Barker et al., 2003). Radiative transfer models for the atmosphere consist of different parts, such as optical properties of atmospheric components and the surface, which are represented by parameterisations. Furthermore, a radiation solver is responsible for determining the path of radiation through the optical medium (Prill et al., 2022). Global weather and climate models currently ignore horizontal radiative transfer in their radiation schemes and only account for the vertical dimension (Prill et al., 2022). Clouds have a significant radiative impact and can demonstrate variations at smaller scales than the model grid-boxes. Therefore, the radiation is calculated distinctly for both the clear-sky and cloudy parts of each grid box. ICON's RRTM radiation scheme is structured to adopt the RRTM gas optics scheme, dividing the

spectral range into 30 bands (16 in the longwave and 14 in the shortwave spectrum, Mlawer et al., 1997). Furthermore, the RRTM scheme relies on several presumptions concerning the scattering and absorption of water, ice, or vapour and their respective shape. This results in the radiation solver utilising these diverse attributes to compute reflectance, transmission, and internal radiation sources within every grid box and on each model layer. The output of this process establishes the resulting radiation flux in both upward and downward directions under both cloudy and clear sky conditions.

The radiation scheme employs the cloud cover parameterisation to calculate precise estimates for cloud cover, cloud water, cloud ice, and precipitation (snow, rain, graupel). The model relies on multiple assumptions regarding the subgrid distribution of water. Meanwhile, the diagnostic cloud cover scheme utilizes data from turbulence, convection, and microphysics parameterisations, allowing for subgrid variability in water vapor, cloud liquid water, and cloud ice to be taken into account.

Table 5.1.: Parameterisations used for the physics in the ICON model adapted from the ICON tutorial (Prill et al., 2022)

Phenomena	Scheme
Non-orographic gravitiy wave drag	parameterisation of gravity wave drag (Orr et al., 2010)
Sub-grid scale orographic drag	Scheme to parameterize the sub-grid scale orographic drag (Lott and Miller, 1997)
Turbulence transfer	Prognostic flux calculation as total kinetic energy (TKE) (Raschendorfer, 2001)
Land transfer model	Multi-layer soil model (TERRA) respecting radiation, biophysical control of evapotranspiration, and heat and soil-water transport (Schrodin and Heise, 2001, Schulz et al., 2016)
Microphysics	Single-moment scheme (Doms et al., 2011, Seifert, 2008)

Regarding convection, ICON provides a bulk mass flux convection scheme that offers three different types of convective clouds (shallow, mid-level, deep), with only one type present in a column at a time based on a trigger function. The cloud base mass flux closure differs for each type of convection, with a CAPE-based closure for deep convection, a boundary layer equilibrium closure for shallow convection, and a large-scale omega-based closure for mid-level convection. Prein et al. 2015 suggest that a cumulus parameterisation is required for resolutions coarser than 4 km. However, for high-resolution simulations (1-3 km), the largest convective clouds can be resolved, rendering

some of the parameterisation affecting deep and mid-level convection unnecessary. The applied method is a modified version of the Tiedtke-Bechtold (Tiedtke, 1989, Bechtold et al., 2008) convection scheme employed in the IFS model, which integrates an enhanced CAPE closure for deep convection to better represent the diurnal cycle of convection over land (Bechtold et al., 2014). Other important physical parameterisations in ICON that were applied in our case study are listed in tab. 5.1.

5.2. Case Study set-up

To calculate a specific geographical region, one can utilize ICON in an area limited mode (ICON-LAM). This can save computational resources as NWP does not have to be utilized on a global scale. However, to achieve this, the coarsest domain, also known as the parent domain, necessitates boundary conditions. We utilized a parent domain of $n = 3$ and $k = 7$ resulting in a 13.2 km horizontal resolution (refer to 5.1). An NWP necessitates an initial state, which can be established through the initial conditions. The horizontal resolution aligns with the boundary conditions accessible via the deterministic ICON Global Reanalysis, enabling its use without modification as initial and boundary conditions for ICON's parent domain. The parent domain's horizontal extent ranges from 1°E to 23°E and from 13°S to 9°N, encompassing a total of 34,888 grid cells. In our case, the boundaries are updated every three hours to ensure that our model accurately reflects the current global reality. Although constant boundary conditions could be assumed, doing so would result in significant deviation from actual reanalysis.

The parent domain is nested twice to allow for a more precise resolution in the region of interest. The first nest (2nd domain) ranges from 3°E to 21°E and from 11°S to 7°N. This results in a horizontal resolution of 6.6 kilometres (see 5.1), half of the parent grid, and a horizontal cell count of 85'304. The second nest (3rd domain) ranges from 5°E to 19°E and from 9°S to 5°N. This leads to a horizontal resolution of 3.3 kilometres, which is a quarter of the coarsest domain (see equation 5.1). The finest domain contains a total of 221,640 cells.

5.2.1. Initial and boundary data and grid

The grids were generated using the ICON Grid Generator software provided by the DWD (Reinert et al., 2020). The external parameter files were also generated in this way, most of which remain constant over shorter simulation times, with some showing a monthly

dependence. These external parameters consist of topography, soil type, and land-sea mask. The initial and boundary conditions rely on global ICON reanalysis data that use a horizontal grid structure of R03B07. These were produced by DWD and downloaded through Pamore (PArallel MOdel data REtrieve from Oracle databases). We used them for our case study.

5.2.2. Convection scheme

Explicit calculation of convection is achievable in a non-hydrostatic model, but when it comes to small-scale convection, a parameterisation scheme is necessary. Convection plays a vital role in modelling the atmosphere, generating cloud formation, precipitation, entrainment, detrainment, subsidence and many other tropospheric phenomena. As outlined in subsection 5.1.2, the ICON model can utilise the Tiedtke/Bechtold convection scheme (Tiedtke, 1989,Bechtold et al., 2008), which allows for the option of shallow and deep convection represented in the NWP model. This is coherent if deep convection can be explicitly calculated through a fine grid with a horizontal resolution of less than 4 km. However, shallow convection cannot yet be explicitly calculated at such a resolution as its processes need finer resolution to represent them correctly.

To simulate, convection has been parameterised in domains 1 and 2. The horizontal resolutions of 13.3 km and 6.6 km, respectively, indicate that turning off the convection scheme would be inappropriate, as convective processes cannot be resolved at this resolution and would be ignored. In the innermost domain, where the horizontal resolution is 3.3 km, we created three distinct cases that vary in their utilization of the convection scheme:

Firstly, a simulation was conducted that fully parameterised convection, including both shallow and deep convection. This particular test case will be referred to as the **parameterised** case.

Then, assuming that deep convection parameterization is unnecessary with a horizontal resolution of 3.3 km, it was deactivated. However, shallow convection is retained to represent its processes. This case will be referred to as a **hybrid**.

The third case entails a simulation wherein the convection scheme is entirely deactivated. Here, the model's numerical convection only explicitly induces convection. This is also the case for shallow convection. This case is referred to as **explicit** or a simulation with explicit convection only.

The ICON simulations are computed utilizing these three settings, and Chapter 7 illustrates their outcomes. The current case study's principal emphasis is on the previously described convective schemes. In this study, we identify and analyse three distinct scenarios: completely parameterised convection (hereafter referred to as 'parameterised'), parameterised shallow convection but not deep convection and mid-level (hereafter referred to as 'hybrid'), and fully explicitly computed with no parameterised convection (hereafter referred to as 'explicit'). Table 5.2 describes the hybrid scenario with $inwp = 1$ and $lshallowconv\_only = True$.

5.2.3. Numerical weather prediction set-up

Several approaches and simulation behaviours have been assessed in this case study, drawing on both existing literature (Schlemmer et al., 2020, Avgoustoglou et al., 2020). A list of crucial settings is provided in tab. 5.2. Given our location in a tropical region, a range of factors were taken into account when determining the optimal settings, including those outlined in tech reports and ICON documentation (Prill et al., 2022).

5.2.4. Case study selection

The case study being conducted with ICON was selected based on specific criteria. The simulation period for ICON needs to be during the dry season. Thus, we have restricted the time frame to July and August, as these are the months when the low-level clouds

Table 5.2.: List of different model settings used in the case study to adapt to the tropical conditions.

Test cases	Parameters	Descriptions
Tropical Setting for the laminar layer over the ocean	rat_sea = 1.0	Changed parameters based on sensitivity study of parameters related to the boundary layer and surface layer.
Tiedtke/Bechtold convection scheme	inwp = 1	Tiedke convection scheme to simulate deep convection, where horizontal resolution is too coarse to resolve deep convection.
Shallow convection scheme	inwp = 1, lshallowconv_only = True	Only the shallow convection scheme is used. The resolution is high enough to simulate deep convection, but not for shallow convection.
Vertical diffusion coefficient	tkhmin = 0.898	Scaling factor for minimum vertical diffusion coefficient for heat and moisture
Evaporation onset below cloud	rhebc_land = 0.7, rhebc_ocean = 0.76	The threshold of relative humidity to establish the evaporation below cloud base.
Entrainment parameter	entrorg = 0.00195	Entrainment parameter to determine the amount of mixing dry or moist air into an moving air parcel (Avgoustoglou et al., 2020)
Initial and boundary data	ICON reanalysis data	ICON reanalysis data as initial and boundary condition war used in this case study. ERA-5 was tested, too but showed unexpected behaviour in moisture
Time interval to update the boundary data	dhour = 3	Boundary data update every hour (only for ERA-5 possible) or every 3 hours for ICON simulations with ICON reanalysis boundary data.

are at their densest (Dommo et al., 2018). The availability of diverse tendencies in the ERA5 (*E*uropean *Re**a**n*alysis version *5*) data (Hersbach et al., 2020) for the years 2018 and 2019 was another determinant in selecting a case. Ultimately, the moisture tendencies derived from ERA5 were no longer considered in this work. To compare the data with actuality, we examined the availability of observation data from radiosonde or Pilot balloon (PiBal) ascents at specific stations in western Equatorial Africa. The upper-air data time slots depicted in Fig. 5.2 and 5.3 illustrate that Pointe-Noire and Ouesso had good data availability periods in July and August 2018. Additionally, assessments of satellite images by visual inspection were conducted to determine the presence of expected stratus clouds.

Taking into account the aforementioned factors, we have selected the time period from the 14th to the 21st July 2018 to serve as our case study. In order to allow NWP models to reach equilibrium and reduce numerical uncertainties, we adopted a 2-hour spin-up time for all three domains. The parent domain was initiated on 13th July 2018 at 1800 UTC, followed by the commencement of the first nest (domain 2) at 2000 UTC and the innermost nest (domain 3) at 2200 UTC.

5.2.5. Parameters in focus

To comprehend the process through which deep convective clouds are generated in the model, it is necessary to examine various parameters from the ICON model. Firstly, a thorough analysis of 2-dimensional variables, namely temperature, dew point temperature, specific humidity, cloud water droplets, cloud ice, rain water, sleet at a height of 2 metres, and meridional and zonal winds at a height of 10 metres, was conducted. Furthermore, this study utilized vertically integrated measures of humidity including precipitation, latent heat, sensible heat and moisture flux. Diagnostic variables were also examined, specifically low-level, mid-level and high-level cloud cover as well as total cloud cover. This research aimed to obtain a comprehensive, three-dimensional analysis of the atmosphere, and thus, certain variables were recorded at both the model and pressure levels. These variables encompassed temperature, pressure, density, the aforementioned humidity, and geopotential heights.

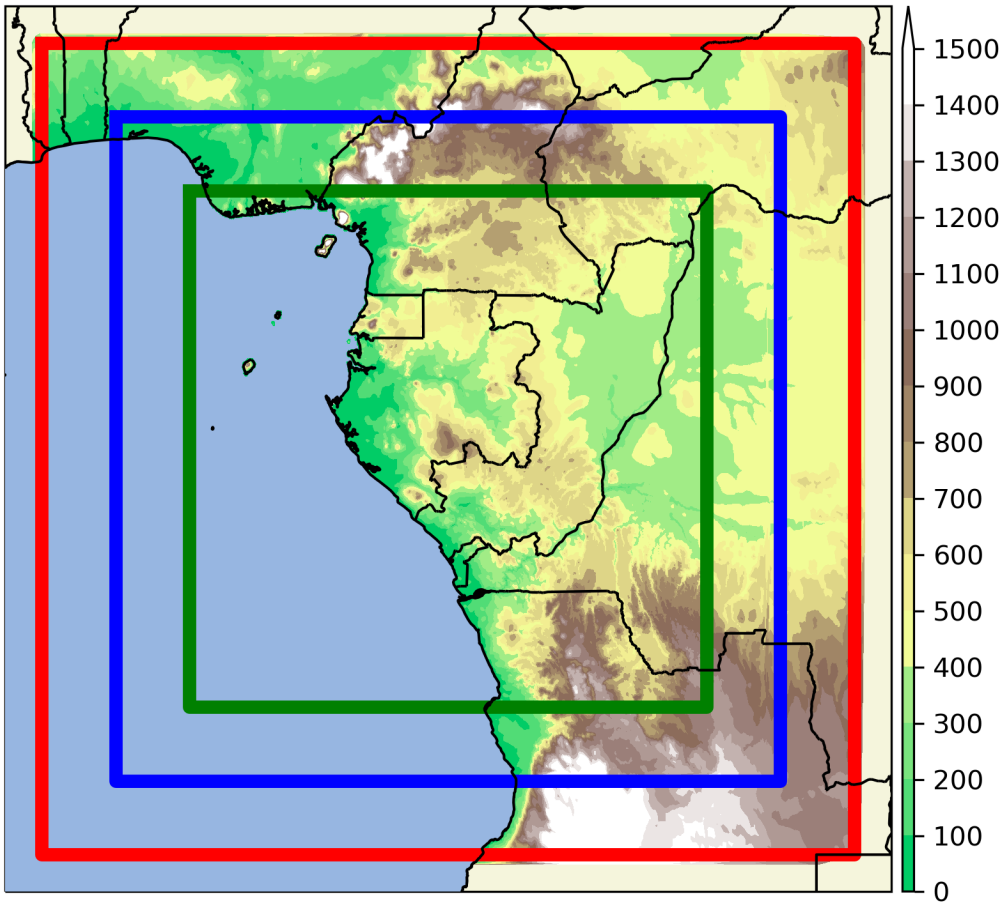

Figure 5.1.: Parent domain (red) of the case study and its two inner nests (blue & green) with the corresponding orography in the model. Spatial horizontal resolutions are 13.3 km, 6.6 km, and 3.3 km resp.

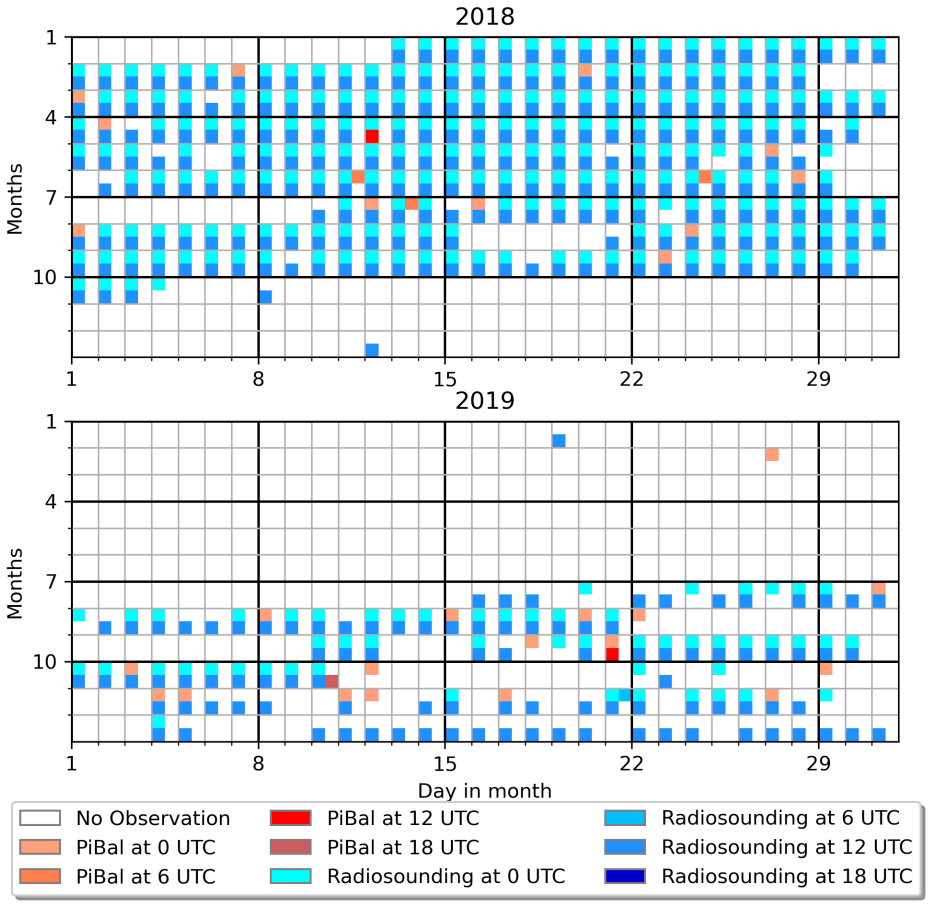

Figure 5.2.: Available upper-air soundings and pilot balloons at Pointe-Noire.

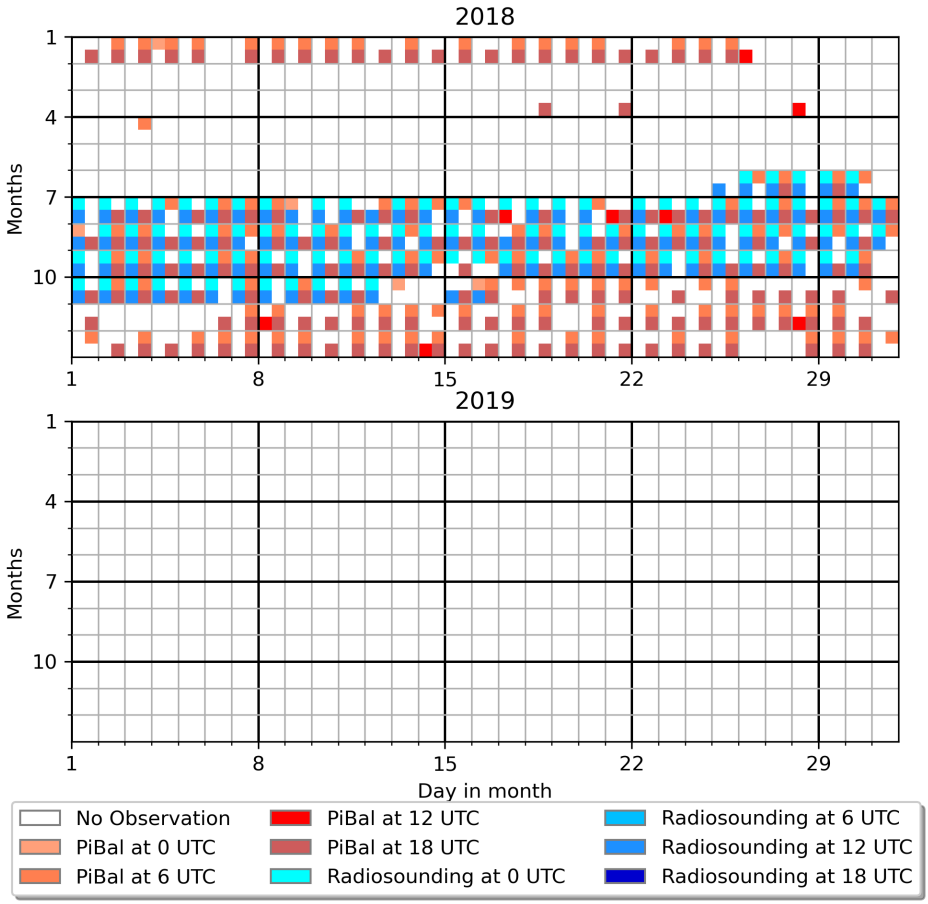

Figure 5.3.: Available upper-air soundings and pilot balloons at Ouesso.

Part III.

Results and Discussion

6. Observations - station and satellite data and its validation

There are different ways of looking at LLCC in WEAs during the long dry season. This chapter focuses on the observations of LLCC and low level cloud types and describes them from different perspectives: Satellite, observer and upper air perspectives. Furthermore, the focus varies in time and space scales. The dirunal cycle during the long dry season is examined from the perspective of a single station and from the spatially gridded view of the satellite. From the station perspective, we will have insight into 3-hourly data, while from the geostationary perspective, a more consistent observation in time is possible. The polar-orbiting satellites perspective is only available twice a day, around 0030 UTC and 1230 UTC, depending on the actual track of the satellites. Therefore, this chapter will first focus on the validation of the satellite data, then on the observer's perspective, and finally move to the satellite's perspective and their climatological outcome.

6.1. Validation of the Meteosat Second Generation low-level clouds determination

The MSG satellite retrievals undergo validation against surface station data through threshold comparisons using Receiving-Operator-Characteristic (ROC) curves and the Heidke-Skill-Score (HSS) method. The ROC indicates the ideal cloud fraction threshold to select when comparing satellite data obtained from MSG with station data. The overall skill of the satellite retrievals will subsequently be evaluated by the HSS.

6.1.1. Receiver Operating Characteristics

The ROC curve seeks to identify the ideal threshold value by comparing the hit rate and false alarm rate. This is accomplished by testing various levels of coverage, which are

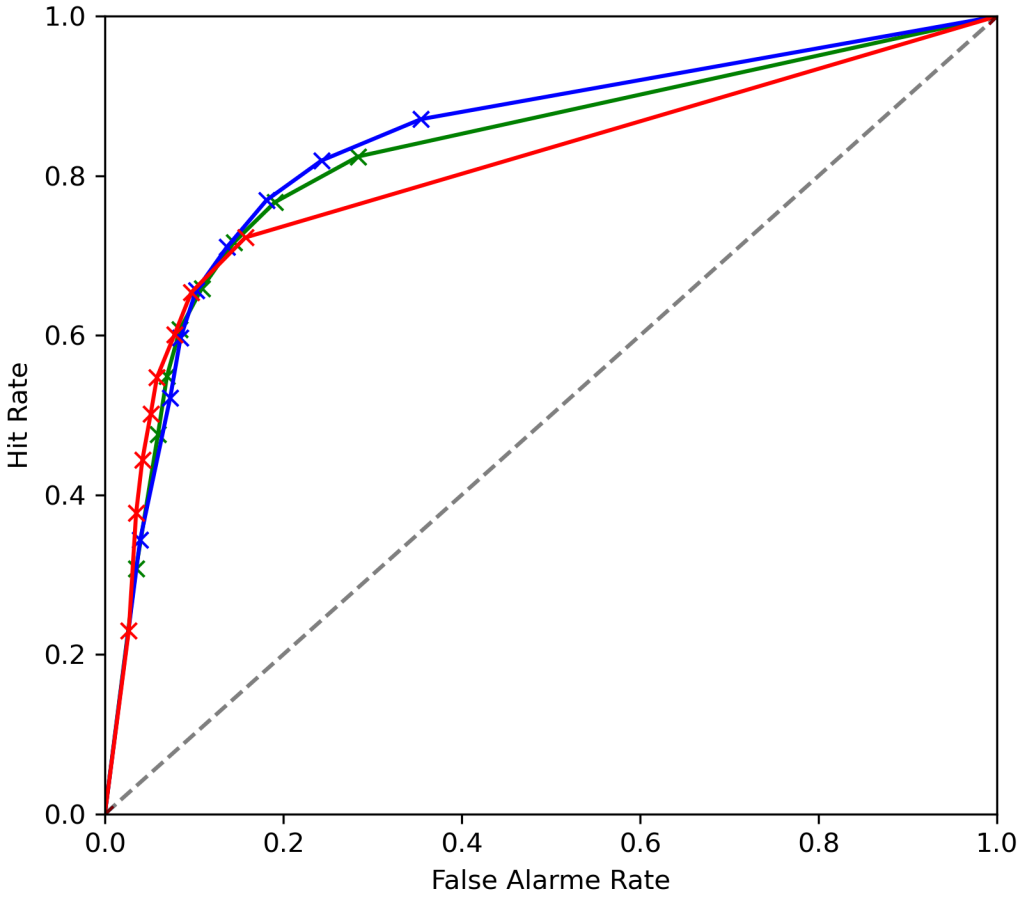

Figure 6.1.: Receiver Operating Characteristics curve representing the trade-off between the False Alarm Rate and the Hit Rate with increasing threshold determining low-level clouds at synoptic weather stations during nighttime (blue), during daytime (red) and in total (green).

defined by the satellite, and assessing the hit rate and false alarm rate. The optimal value for increasing the hit rate while avoiding significant increases in the false alarm rate is the one with the largest area under the curve (see Fig. 6.1).

The ROC curve shows greater right-skewness during the day and greater symmetry during the night. This can be attributed to the higher likelihood of detecting LLCC during the night. For optimal performance during the night, a higher threshold is recommended compared to daytime. The shape of all curves implies that the schemes have a tendency to overlook some parts of cloud fraction. Therefore, a lower threshold must be employed to clearly identify instances of cloudy conditions. Finally, the most suitable value is achieved

by considering 12.5% sky coverage to be cloudy. This approach aligns the space-based perspective with the station-based statistics.

6.1.2. Heidke-Skill-Score

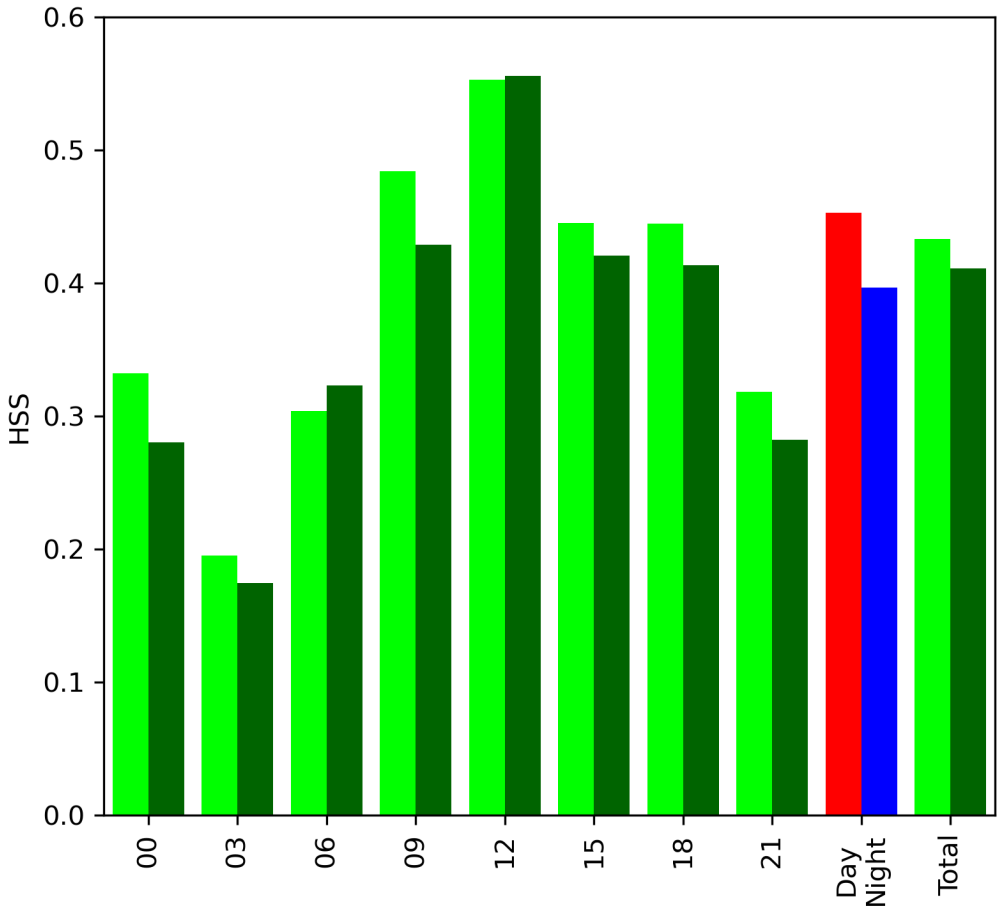

Figure 6.2.: Heidke-Skill-Score of satellite retrievals determining low-level clouds at synoptic weather stations every 3 hours and calculated for day (red) and night (blue) and in total, for the thresholds 12.5% (lime) and 25 % (darkgreen).

The HSS demonstrates a high dependence on time for the detection capabilities of LLCC by the MSG (see Fig. 6.2). The greatest values for detection occur during the day, with the peak at 1200 UTC. Although the value at 0600 UTC is still low due to the distortion caused by the sun glint, the HSS at 0900 UTC, 1200 UTC and 1500 UTC are between 0.4 and 0.6 for both thresholds shown. Overall, the satellite typically detects

a higher score for cloud cover when using the smallest threshold of 12.5%, with some exceptions at 0600 UTC and 1200 UTC when the second smallest threshold (25%) is applied. The HSS is more variable during the night, ranging from approximately 0.2 (at 3 UTC) to as high as 0.44 (at 1800 UTC).

The validation indicates that cloud detection is more frequent during the night, resulting in less underestimation or greater overestimation of LLCC as compared to daytime.

6.2. Observer's perspective

Observing the sky and recording the fraction of cloud cover and observed cloud type constitutes a fundamental observation technique that has been in use for centuries (see Chapter 2). However, it can be considered inconsistent as it relies on the individual's personal and subjective visual impression of the sky. Nonetheless, such observations still offer considerable value. The more recent the records, the more uniform and sophisticated the observations become. Nowadays, a standardised approach is used (WMO, 2019b) to observe clouds.

For further analysis, WEA has been divided into four subregions based on their topographical circumstances. These regions include the coastal region, which encompasses the area adjacent to the Atlantic Ocean; the windward Chaillu, where the wind blows uphill over the Chaillu mountains; the Plateau, which consists of the leeward side of the Chaillu, incorporating the Batéké plateau and the Ivindo-Ogooué plateau; and the northeast of the RC (see Fig. 6.3).

6.2.1. Diurnal Cycle of low-level cloud cover

The diurnal cycle of LLCC during the long dry season varies depending on the region in WEA. Figure 6.4 illustrates that LLCC typically forms at night and dissipates during the day. However, in WEA, LLCC density varies depending on the time and specific region. For instance, the coastal region of Gabon (blue) experiences lower levels of LLCC compared to the windward side of the Chaillu Massif (orange). The decay of the LLCC is stronger and therefore has a higher amplitude compared to the windward side of Chaillu. Although the formation and dissipation times are almost the same in these two regions, the genesis of the LLCC in the windward side of the Chaillu mountains is 3 hours earlier than in the near coastal region. In the plateau region, the diurnal cycle is offset by 3 to 6 hours compared to

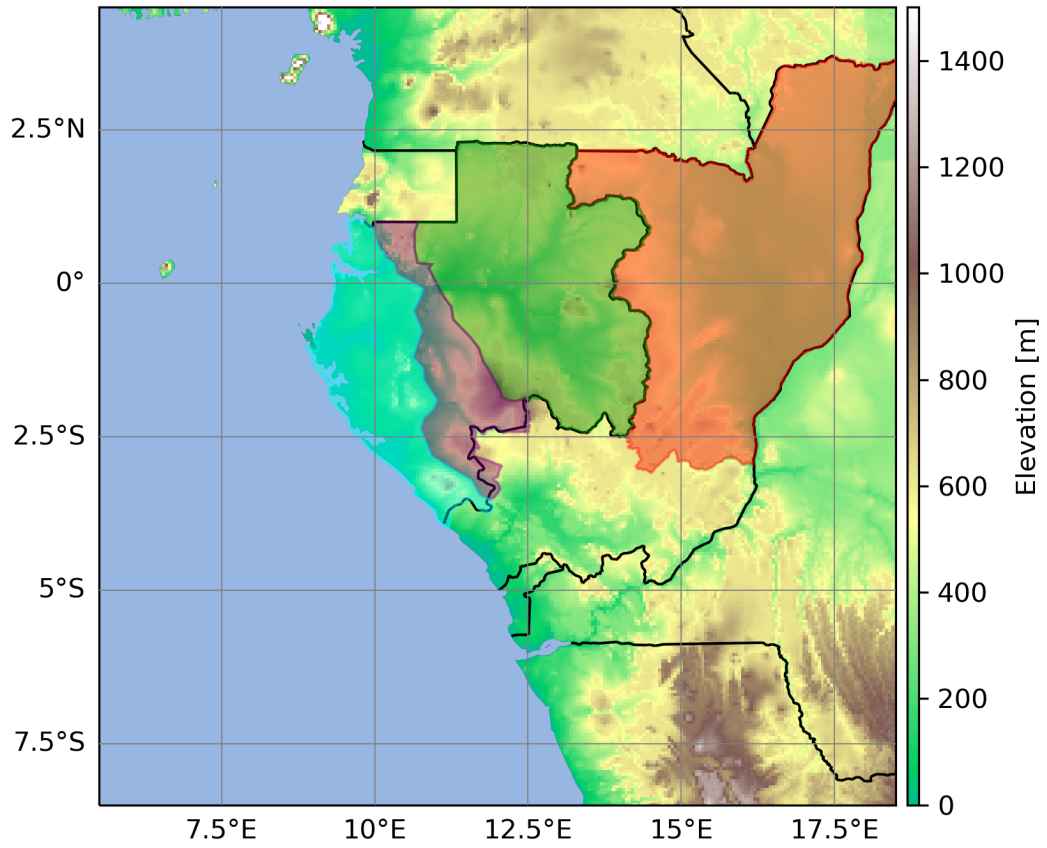

Figure 6.3.: Western Equatorial Africa with four subregions: Coastal region (cyan), windward side of the Chaillu mountains (purple), the plateau region (green) and the Northeast of the Republic of Congo (red).

the windward and coastal regions of the Chaillu. Additionally, the LLCC layer is slightly denser and has a higher amplitude over the Ogooué plateau. In the northeast part of the Republic of Congo (RC), the LLCC is generally lower than in regions of Gabon. However, the formation and dissolution times of the LLCC deck are similar to those over the plateau, with cloud formation during the night and morning and dissipation in the afternoon.

During daytime and early morning, the maximum amount of stratiform clouds is over the windward side of the Chaillu mountains, while at night the coastal regions have a higher fraction of stratiform clouds (see Fig. 6.4, bars). However, during late night and morning on the plateau, the percentage of stratiform clouds is similar to that of the coastal regions, but decreases sharply in the afternoon. Over the northeastern region of RC, the

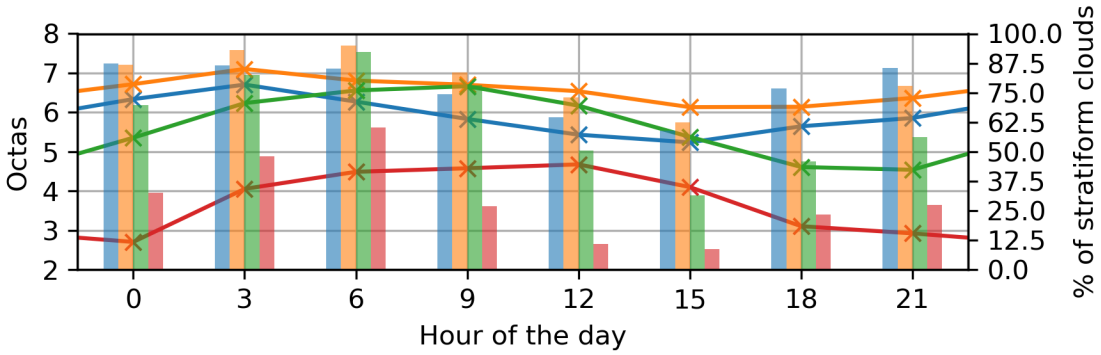

Figure 6.4.: Lines: Diurnal cycle of the LLCC separated into the subregions coastal, the windward side of the Chaillu mountains, the plateau behind the Chaillu mountains and the northeastern part of the Republic of Congo. Bars: Percentage of stratiform low-level clouds. Data is based on the synoptic weather reports from surface weather stations in each regions from June-September 1971-2019.

proportion of stratiform clouds is higher in amplitude when compared to the coastal and leeward regions of the Chaillu mountains. The Ogooué plateau and the coastal region, located up and downstream of the leeward side of the Chaillu mountains, exhibit a higher amplitude of LLCC and a lower prevalence of stratiform clouds on average. In the context of the prevailing environment in Gabon, a consistent flow and orographic uplift of air can result in a permanent high LLCC on the windward side of the Chaillu mountains.

Figure 6.5 presents a more detailed distribution of the diurnal cycle of LLCC. The upper panels (a-h) display the mean cloud fraction at reported main times (every three hours), whereas the middle panels (i-p) show the cloud fraction of stratiform LLCC types 4-8, and the lower panels only consider the average cloud fraction of cumuliform cloud types 1-3 and 9. Clear skies (0 octas) are only included in the upper panels for obvious reasons, as clear sky reports do not include a cloud type. In general, there is a higher occurrence of LLCC over Gabon compared to the RC. A noticeable trend among almost all stations is a lower cloud fraction in the panels with cumuliform clouds represented as compared to them with stratiform clouds. Cumuliform clouds are mainly observed later during the day when irradiation causes the cloud decks to break up. The diurnal cycle of all cloud types is less distinguishable compared to Fig. 6.4. However, the appearance of clouds during late night and early morning, and the disappearance of clouds during the afternoon and early evening is noticeable. Stratiform clouds have a higher amplitude in cloud fraction compared to cumuliform clouds and all cloud types considered (see Fig. 6.5). This phenomenon is evident in eastern Gabon, southeastern Cameroon, and southwestern

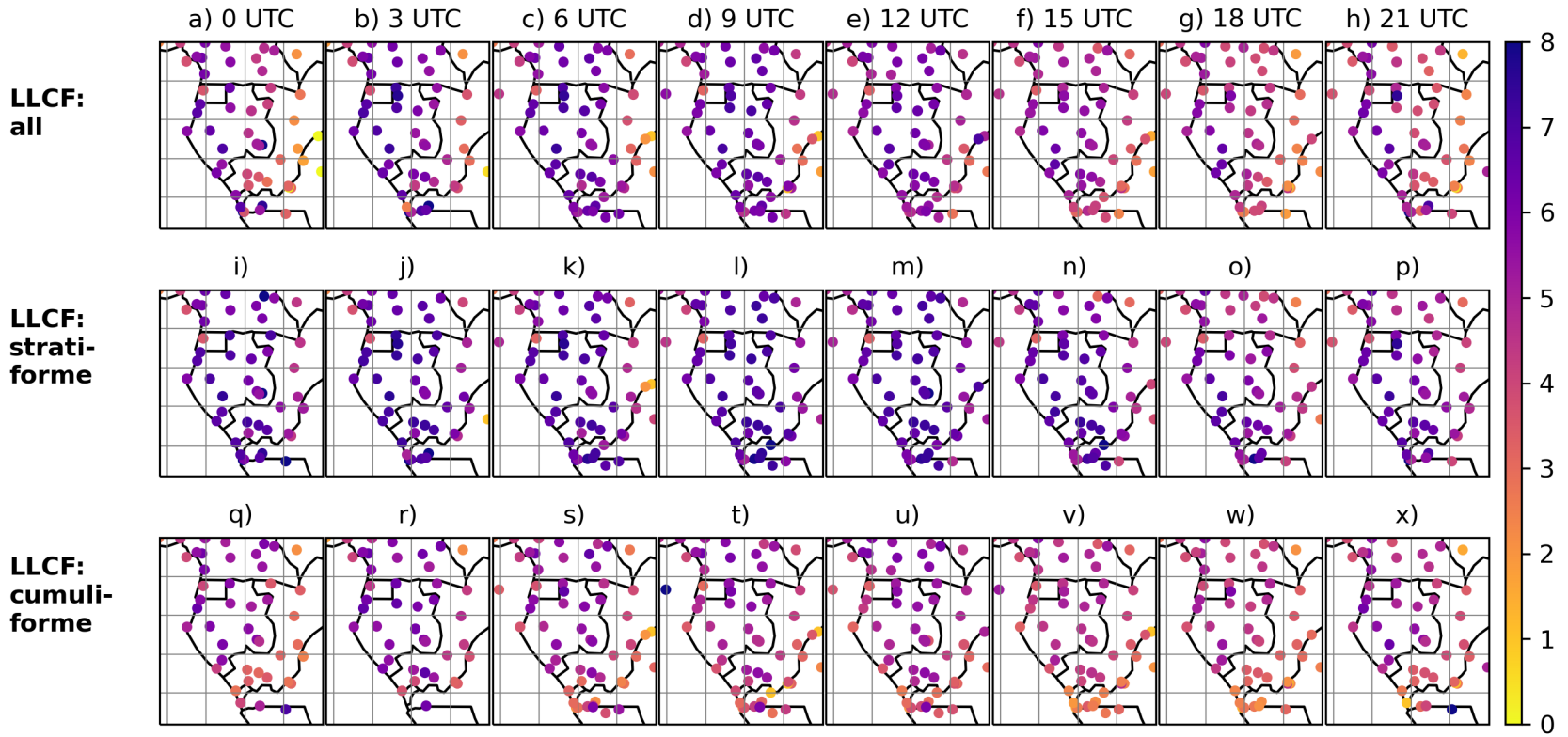

Figure 6.5.: Cloud fraction in WEA during JJAS for all cloud observations (a-h) and for distinct cloud types between stratiforme (cloud types 4, 5, 6, 7, and 8; i-p) and cumluliforme (cloud types 1, 2, 3, and 9; q-x). Data is based on the synoptic weather reports from surface weather stations in each subregions from 1971-2019 from June-September.

RC. The break up occurs earlier compared to the regions over Gabon. Additionally, as the stratiform clouds disappear (see Fig. 6.5i-p), the cumuliform clouds emerge (see Fig. 6.5q-x). This illustrates the transition from stratiform clouds to cumuliform clouds, which is primarily driven by radiation and turbulence during the day. Nevertheless, the convection is usually not as strong to create deep convection and finally precipitation.

The diurnal pattern of low-level clouds, as derived from station data, reveals nighttime and early morning formation of low-level clouds with a subsequent transition to cumuliform clouds during the afternoon. Additionally, the LLCC present on the windward side of the Chaillu mountains persist due to orographic lifting, thereby reducing the amplitude of the diurnal cycle. In summary, the combined dataset's diurnal cycle aligns with expectations established by Dommo et al. (2018).

6.2.2. Spatial distribution of cloud genera

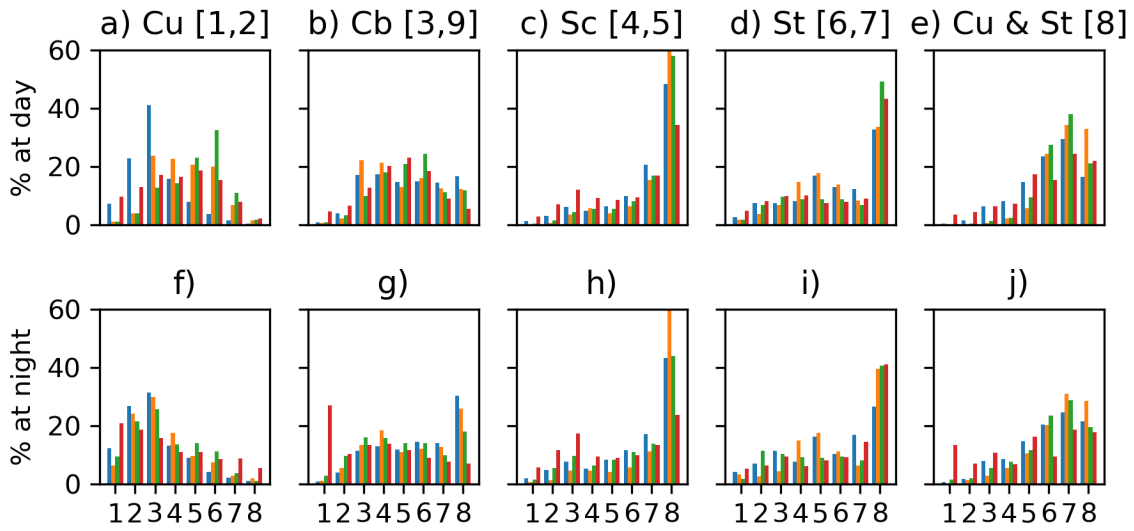

Figure 6.6.: Distribution in percentage of all synoptic low-level cloud types along the cloud fraction in Octas over each of the four regions Coastal (blue), windward side of the Chaillu mountains (orange), Plateau (green), and northeast RC (red). Upper panels are at daytime, lower panels at nighttime. Data is based on the synoptic weather reports from surface weather stations in each regions from 1971-2019 from June-September (Aellig et al., 2022)

The low-level cloud types provide valuable insights into the behaviour of the LLCC deck. The distribution of stratiform cloud genera (see Fig. 6.6c-e, h-j) is strongly left-skewed, indicating more stratiform clouds are present with increased cloud cover in

all four regions. Conversely, the distribution of cumuliform clouds is right-skewed. The distributions of cumulus clouds (type 1 and 2) are more or less similar during the night in all regions (see Fig. 6.6f). However, this is not true for the coastal region during the day. There is no significant skewness on the windward side of the Chaillu mountains and northeastern RC region. However, the low-level cumulus clouds on the Ogooué plateau have a right skew, while the coastal region has a left skew (see Fig. 6.6a). For the coast, cumulus clouds usually occur when they do not cover the entire sky, whereas over the plateau, they tend to cover larger regions. The cloud fraction for Cumulus is higher compared to other regions there, which provides evidence of how cumulus clouds are influenced differently in these two regions. While cumulus clouds can form over the coastal region after clear sky conditions, the cumulus clouds over the plateau appear to be a result of the break-up of the LLCC deck. Another noteworthy aspect is the distribution of cumulonimbus clouds (see Fig. 6.6g) at night, when comparing the northeast of the RC and the coastal area. As one moves farther east in WEA, the sky is less covered in the presence of a cumulonimbus cloud. This demonstrates that cumulus nimbus clouds in northeast RC are visible from greater distances when there are fewer low-level clouds concealing them. This suggests that if there are cumulonimbus clouds, they are more visible in the northeast of the RC. Mesoscale Convective Systems (MCS) are increasingly prevalent farther east, where the dry season has less of a dominant impact compared to farther west in western Equatorial Africa.

Stratocumulus clouds (see Fig. 6.6c+h) are associated with denser LLCC and are most pronounced over the windward side of the Chaillu mountain range. The contrast in cloud cover between the windward side of the Chaillu mountains and the other three regions is even greater at night. This highlights the orographic influence in cloud formation over the Chaillu mountains, which is significantly more prominent during nighttime, as

Table 6.1.: Cloud type frequencies at day and night depending on the subregion.

		Cu (1+2)	Cb (3+9)	Sc (4+5)	St (6+7)	Sc+Cu (8)	Total
Coastal	Day	15.8	12.9	39.3	0.7	31.3	86050
	Night	2.1	13.4	79.5	0.7	4.3	64172
Windward Chaillu	Day	12.9	8.4	52.4	0.9	25.3	51437
	Night	2.5	14.7	79.4	0.6	2.8	29562
Plateau	Day	26.2	11.1	47.2	2.5	13.0	101309
	Night	5.7	25.1	64.7	1.6	1.8	54273
NE RC	Day	46.4	25.6	19.3	5.6	3.0	70741
	Night	7.7	50.0	38.4	2.9	0.8	32503

previously mentioned in the preceding section. The stratus clouds (see Fig. 6.6d+i) exhibit limited distinctiveness, except for their association with denser cloud decks. The greater incidence of stratus during daytime in the northeast RC seems incongruous with the more convection-driven weather in this region compared to other regions. However, the limited amount of observations prohibits confident statements regarding the stratus clouds. Table 6.1 illustrates that stratus clouds (type 6 & 7) are only reported a few times and even less often during the night. Therefore, the statement based on this information is less robust.

Simultaneously observed Stratocumulus and Cumulus clouds of cloud type 8 exhibit a left-skewed distribution as illustrated in Figs. 6.6e & j. This suggests that these types of clouds are generally considered as transitional between cloud types 1 and 2, as well as 4 and 5. During nighttime in northeastern RC, cloud type 8 displays an unclear left skew shape. This may be attributed to the limited data available, as only less than 0.8% of cases report cloud type 8. Stratocumulus clouds (types 4 & 5) are frequently observed at night compared to during the day. The magnitude is greatest along the coast, while higher amounts of stratocumulus clouds are also present during the day along the windward side of the Chaillu mountains and over the plateau. Stratocumulus clouds occur less frequently over the northeast RC, but their mean fraction at night is twice that during the day. The lower cloud amplitude over the windward side of the Chaillu mountains shows the dominant part of orographically driven cloud formation compared to the other regions. According to table 6.1, cumulus (types 1 and 2) and cumulonimbus (types 3 and 9) are the predominant cloud types in the northeast RC, driven more by convection compared to other clouds. The higher occurrence of cumulus clouds (46.4% vs 7.7%) during the day indicates a significant impact of radiation, resulting in their frequent formation. A transition from cumulus to cumulunimbus during the afternoon and evening is also noteworthy. The development of deep convection may take more time during JJAS, but it still happens, and more transitions into the night in northeastern RC.

Taken together, each region has its own distinct occurrence of each low-level cloud type. The windward side of the Chaillu mountains has the strongest stratocumulus presence, while the northeast RC is more dominated by convection and has a higher occurrence of cumulus clouds. Furthermore, over the coastal region, cumulus clouds tend to occur with low amounts of clouds, which implies a stronger convection-driven cloud formation from a clear sky.

6.3. Satellite's perspective

Satellite observations provide a continuous and consistent perspective in both space and time compared to subjective, ground-based observations, owing to the use of the same instruments. This section focuses initially on observations from the geostationary MSG satellite. This is followed by an analysis of the Geoprof product based on two sun-synchronous satellites. A comparison between the two products concludes the section.

6.3.1. Meteosat Second Generation - The Geostationary Perspective

A consistent dataset, both temporally and spatially, is available for observing the atmosphere from space with MSG. Its data is subjected to both DMS and NMS schemes, resulting in RGB images that illustrate various cloud types. In chapter 4, the thresholds in two SEVIRI instrument channels are elaborated upon to define and showcase the diurnal cycle of LLCC. Firstly, a transition from night to day and vice versa occurs. The approach to detecting LLCC through SEVIRI instruments varies between these times. During the night, only IR or NIR channels are applicable, whereas during the day, visible channels are also available. Thus, there is incongruity in the comparison of LLCC between day and night utilizing SEVIRI. A marked decrease in LLCC is evident from night to day, as seen in Fig. 6.7. Additionally, a sun glint effect is observed around sunrise and sunset, indicated by a substantial increase in LCOF between 0600 UTC and 0700 UTC.

Between 1800 and 2100 UTC, the rise of the LCOF correlates with the increase in LLCC, as noted in the previous results chapters. Slight increases in LCOF frequency occur at night over the ocean due to outgoing longwave radiation cooling the lower troposphere, where cloud formation takes place. Additionally, over WEA, the LCOF also rises, but topographical and atmospheric circumstances may play a greater role compared to the more uniform ocean environment. During the night, there is a noticeable elevation of LCOF over the windward slope of the Chaillu mountains extending up to the western reaches of the Cristal mountains (see Fig. 6.7a-d) and along the coast from Gabon to RC, the Democratic Republic of Congo (DRC), and down to the north of Angola. A significant LLCC expansion occurs in the western component of the Chaillu mountains at 0300 UTC (see Fig. 6.7c,d). The rise along the leeward side of the Chaillu mountains is due to orographic lifting along the wind flow.

At 0600 UTC (see Fig. 6.7e), LLCC is higher along the leeward side of the Chaillu and Cristal mountains. However, the LLCC decreases in the leeward side of Chaillu compared

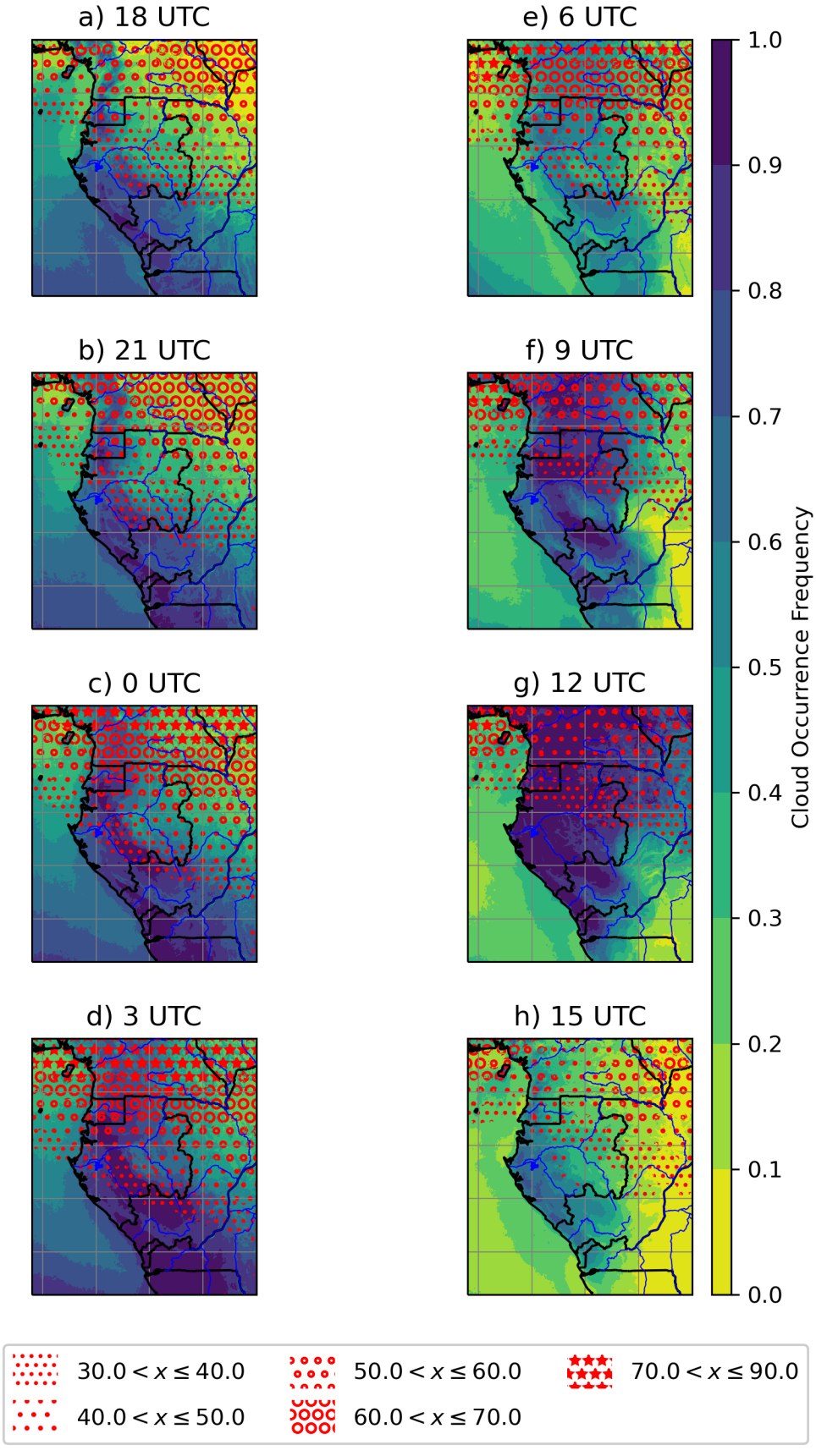

Figure 6.7.: LCOF above WEA every 3 hours. LHS at nightime, RHS at daytime. Hatched are frequencies of higher clouds where LCOF could not be determined.

to the rest of the area above the mountains of Chaillu. This reduction in the frequency of low-level clouds (LCOF) is also visible at 0300 UTC and 0900 UTC. The occurrence of this decrease in cloud frequency may be attributed to the droplet evaporation during descending behind the Chaillu mountains (a slight Foehn effect). From 0900 UTC to 1200 UTC, the LCOF shows an increase, particularly in the northern part of the region of interest (see Fig. 6.7f,g). Additionally, there is an increase in the higher clouds (red hatched) in the northern area. The detection of LLCC is not possible beneath higher clouds, leading to reduced reliability of the LCOF dataset towards the north (Cameroon). Additionally, it is reasonable to infer convection from the presence of taller clouds in the area northwards towards the ITCZ, where precipitation and convection are frequent features. In the afternoon, from 1200 UTC to 1500 UTC, the LCOF decreases over the whole WEA. Nonetheless, the decrease is less pronounced in the shelter of the Chaillu mountains. This is due to orographical lifting caused by the transfer of air from the Atlantic to the plateau region in the lower levels, resulting in increased cloud formation or reduced clearing in the course of the day. In the eastern part of Gabon and RC, a clear sky is observed along with a reduction in LLCC based on station data. Cloud type observations from the station data indicate a transition from stratocumulus clouds to cumulus clouds. Figure 6.7d,e shows an increase in LCOF in coastal regions from 1500 UTC to 1800 UTC. This finding contradicts the results obtained from station data. This change is a result of transitioning from daytime to nighttime and switching to various channels to determine the LCOF.

This section aims to present an overview of LCOF in WEA from the perspective of geostationary satellite observations. A clearly defined diurnal cycle shows the formation of clouds over Gabon during the night until midday. The east and north of the area of interest is more convectively active in the afternoon and early night. The windward side of Chaillu is more permanently dominated by LLCC, while on the leeward side a more frequent clearing is observed. In general, the diurnal cycle matches the observations made by surface stations.

6.3.2. CALIPSO/CloudSat - The vertical insight

In this section, we analyse the cloud product Geoprof, which is based on the CALIOP instrument on the CALIPSO satellite and the CPR instrument on the CloudSat satellite. Both satellites are part of the A-train and orbit the Earth in a sun-synchronous cycle of approximately 94 minutes over a 16-day period, passing over the region of interest (WEA)

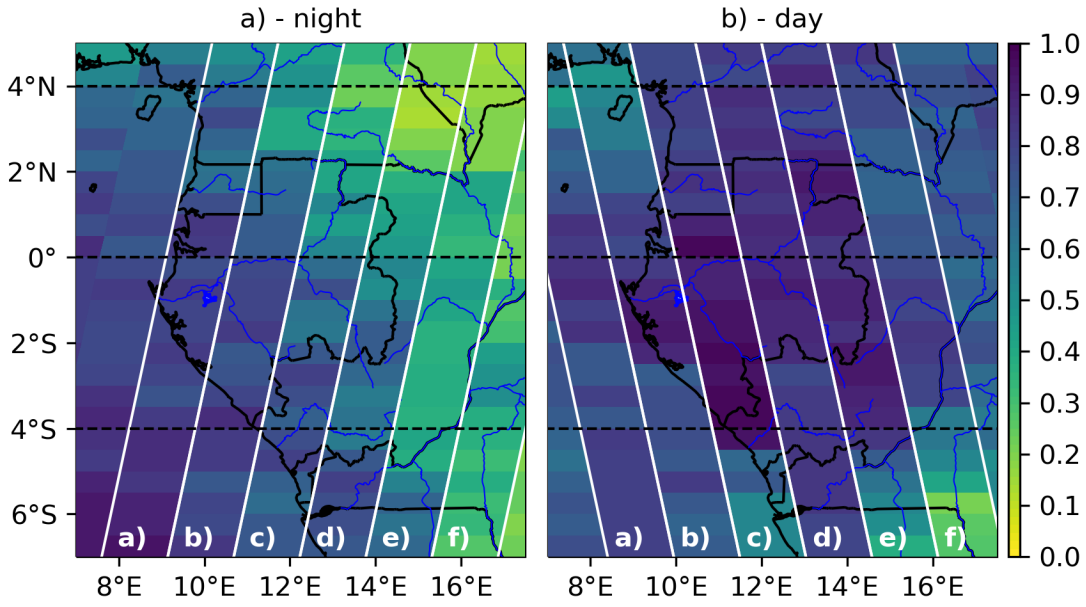

Figure 6.8.: LCOF climatology based on Geoprof. LHS at nighttime, RHS at daytime of all clouds below 3000 m.a.s.l. On each panel are 6 paths with corresponding letters. The vertical insight to this paths will be shown in Figs. 6.9 for nighttime, resp. 6.10 for daytime.

twice daily, shortly after noon and midnight. The sun-synchronous orbit does not permit a consistently spatial and temporal recording of the Earth. However, its instruments, which are both active and closely placed at 708 km above the Earth's surface, permit vertical insights into the Earth's atmosphere. The timeframes analyzed were from 2006 to 2010 during the night and from 2006 to 2018 during the day.

6.3.3. Low-level cloud occurence frequency distribution over western Equatorial Africa by CALIPSO and CloudSat

The vertical distribution of cloud cover is shown in an interesting way by the Geoprof LCOF (see Fig. 6.8). Clouds that are below 3000 m.a.s.l. are classified as LLCC (see Fig. 6.8a). There is a positive LCOF gradient from the east to the west during the night. In contrast, towards the northeast, the LCOF is significantly lower, which was observed in previous studies of LLCC.

Convection may result in the dissolution of LLCC and fragmentation of the cloud deck. During the night, the LCOF is lower in the DRC and eastern RC regions towards the east. In addition, the LLCC is weaker compared to closer to the coast. This suggests that the boundary layer is more moist closer to the sea and mixed higher up over land. Over the southwestern part of the Atlantic, there is a higher LCOF during the night, and as one moves more south, the cloud deck becomes more stratiform. This aligns with the general tendencies of the oceanic atmosphere in the southern Atlantic region during JJAS. LCOF is higher at noon when the satellites CALIPSO and CloudSat pass over the area of interest, compared to midnight (see Fig. 6.8). Comparing LCOF below 3000 m.a.s.l. during the day, it is higher over land while there is no significant contrast between the Atlantic and the land at night. During the night, the absence of radiation leads to a decrease in vertical mixing, and cloud formation can begin from outgoing radiative cooling. However, the LCOF is not yet exceptionally high at midnight when the polar-orbiting satellites pass over the region. Moreover, it has been observed that there is a higher LCOF during the day along higher orography. The LCOF exhibits higher levels along the Chaillu mountain range and around the Cristal mountains located to the north of the Ogooué valley. The orographic uplift of air parcels transported to the east results in condensation and cloud formation on the windward side and crest of the Cristal mountains. The LCOF is high at noon in southeastern Cameroon, compared to low LCOF during midnight in this region.

6.3.4. Low-level cloud occurence frequency's vertical distribution along the paths of CALIPSO and CloudSat

Shifting attention towards the vertical distribution of cloud occurrence frequency reveals a more varied outlook. In Fig. 6.9a, wherein the southwestern most region of the path traverses over the sea, a tight cloud distribution is observed with cloud cover mostly occurring below 1500 m.a.s.l. The highest concentration of clouds is located even lower, around 750 m.a.s.l. Upon reaching the northeastern part of the path that spans over land, the frequency of cloud occurrence is more evenly distributed vertically. The transition from sea to land, with its significantly rougher surface, substantially impacts the formation and persistence of clouds. Although there may be minimal turbulence during the night, and the orography may not reach high altitudes, the cloud layer transported from the sea experiences notable disturbances and greater vertical distribution from 2°S to 0° (see Fig. 6.9a). As we move farther northeastwards along the transect and go past the Cristal mountains, the LCOF becomes higher on the windward side and over the ridge. One

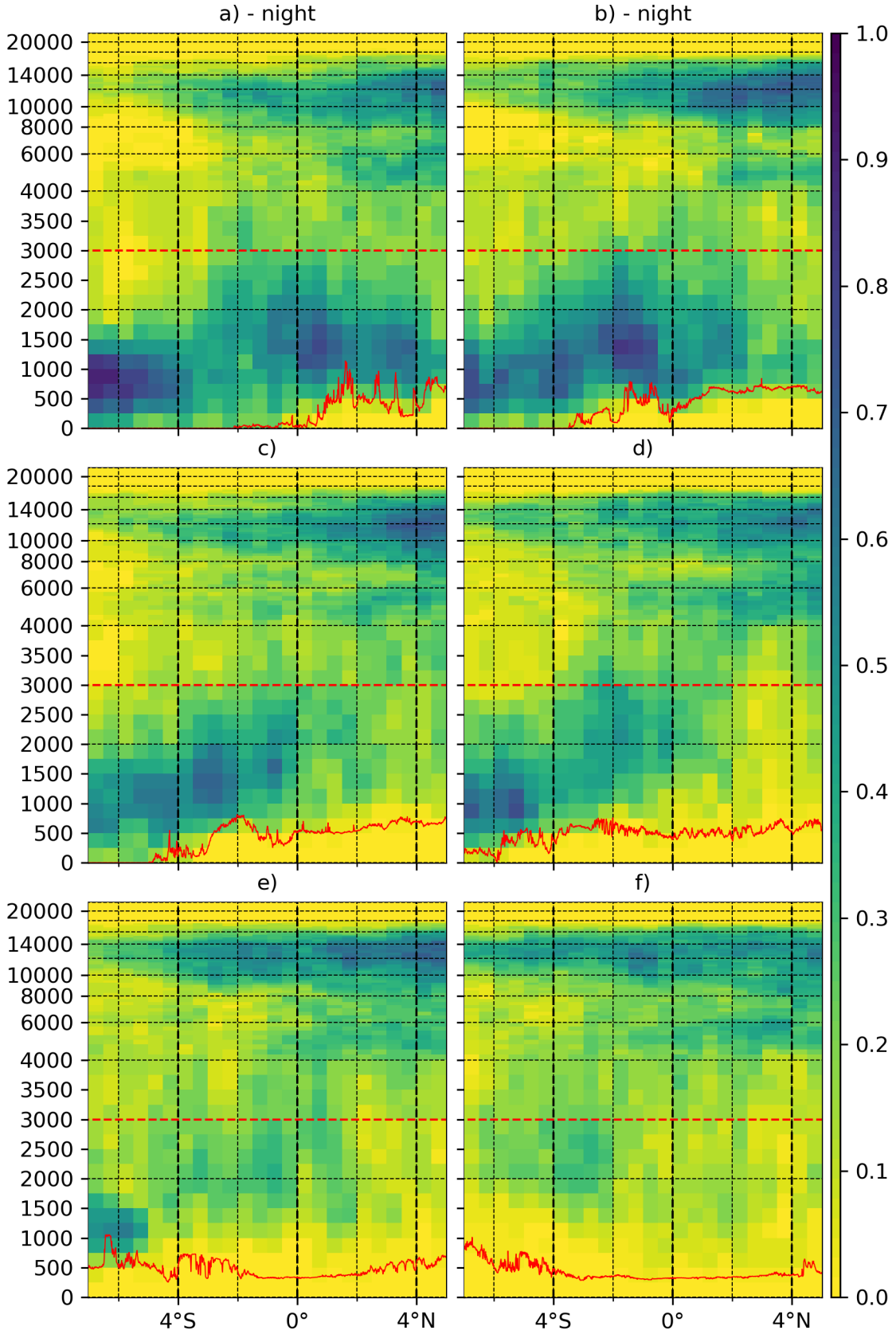

Figure 6.9.: LCOF climatology by Geoprof during the night. Swaths from west to east referenced in Fig. 6.8a

swath to the east, swath b) at midnight (see Fig. 6.8a), follows a path closer to the Chaillu mountain range and has a comparable vertical distribution to the previously mentioned swath to the west. From 7°S to 3.5°S (see Fig. 6.9b), the maritime cloud deck is visible, but has been significantly disturbed farther south due to its earlier landfall along the swath. A higher LCOF is observed along the windward side and over the ridge, corresponding to the orographic uplift over the windward side. As depicted in Fig. 6.9c, the COF is high below 3000 m.a.s.l. from the coast to the windward side of the Chaillu mountains. There is a slight decrease in COF within the leeward zone, while it is high again over the Batéké plateau extending to 0°. North of the equator, there is no clear differentiation of COF below and above 3000 m.a.s.l as shown in swath c of Fig. 6.9. In swath d (see Fig. 6.9), there is a higher LCOF in the southernmost part of the swath compared to the rest of the swath farther north. It is possible that the increased turbulence from the rougher surface or the higher moisture in the air due to the region's proximity to the sea could contribute to this. The COF ranges from ground level to 3000 m.a.s.l. over the Batéké plateau and RC, from 4°S to 0°. Farther north, COF is not higher closer to the ground. Swath e) in Fig. 6.9 exhibits a small section with a higher LCOF in the south, but COF subsequently decreases considerably over the remainder of the swath, farther north over RC. The LCOF is decreased in the northern regions of RC. In swath f) of Fig 6.9, the image looks similar. Between altitudes of 1000 and 3000 m.a.g.l., occasional clouds appear, but a distinctive LCOF is not visible at all. This far east over the DRC, LLCC is no longer expected due to the more intense convection there. Across all six swaths, there is a high COF towards the north. The deep convection occurring farther north results in significantly higher clouds, a finding already noted in both station observations and SEVIRI measurements.

At midday, the situation appears different (see Fig. 6.10). In the eastern region, where the path is almost entirely over the ocean, there is usually a clear cloud deck below 2000 m.a.s.l. (see Fig. 6.10a). The majority of clouds are found below 1000 m.a.s.l. As we move north, LCOF becomes more widely distributed, and the active convective system farther north generates an increasing number of high clouds over the Gulf of Guinea. In swath b) of Fig. 6.10, a clearly distinguishable cloud deck is also observed. However, between 3°S and 0.5°S, the swath passes over land which is impressively recognizable with a higher reaching and more intense COF in the lower troposphere. Due to radiation and roughness over land, the enhanced turbulence causes mixing of the atmosphere to go higher, leading to an intensification in the process of cloud formation. The Pico Basile (located between 3°N and 3.5°N) boasts remarkable concentrations of COF at high altitudes,

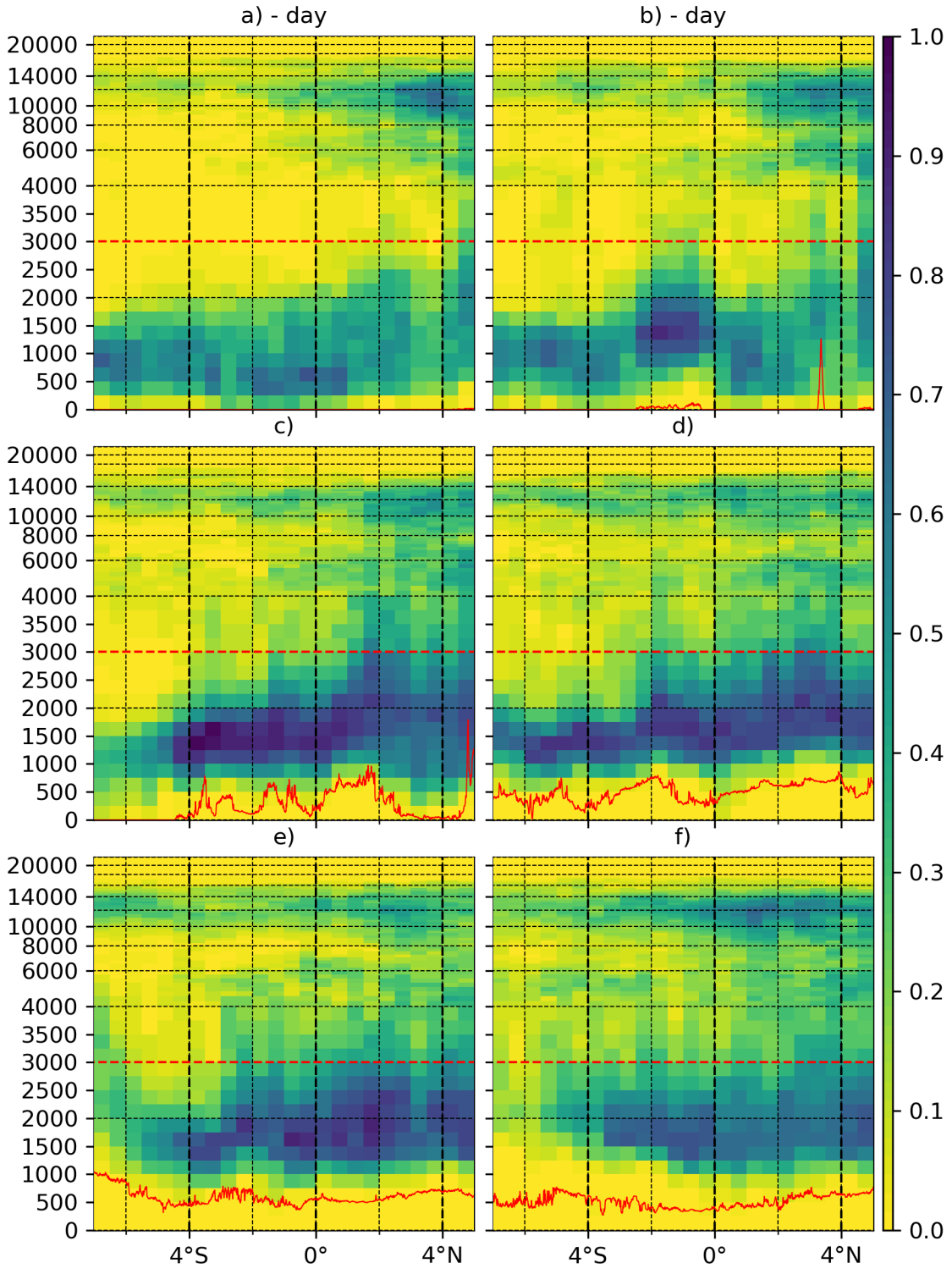

Figure 6.10.: LCOF climatology by Geoprof during the day. Swaths from west to east referenced in fig. 6.8b

though it is not particularly relevant to LLCC over WEA. Farther to the west in swath c) (see Fig. 6.10), the majority of the swath from 4°S to 2°N is over the windward side or crest of the Chaillu or Cristal mountain ranges, where a strong and dense cloud deck between ground and 3000 m a.s.l. is observed. This starts with the landfall of the swath. South of 4°S, near the coasts of Angola, DRC, and RC, the LCOF is weaker than over land. In this region, large-scale subsidence may be dominant. Along swath d) depicted in Fig. 6.10, there is a clear and dense cloud deck. Clouds in the southern region tend to be located below 2000 m.a.s.l, whereas in the northern area, they are more widely spread out vertically. The farther north you go, the more convection is activated, deepening the clouds and raising their altitude. Looking at swath e) and f), the COF is found to be highest within the first 3000 m.a.s.l., but more intense in swath e) specifically. Swath e) is situated above the Batéké plateau, which still contains a considerable amount of moisture in the lower troposphere. In swath f), there is a slightly higher frequency of very high clouds, indicating more active convection towards the east. In swath e) and f), fewer clouds are present in the southern region between 7°S and 4°S due to the drier climate and subsidence towards the arid climate, which dominate this area. Towards the northern areas in all swaths, the COF is more vertically distributed due to increased convection.

The Geoprof data demonstrates the vertical distribution of COF. Greater turbulence and radiation due to landfall lead to more vertically distributed clouds. The moisture concentration towards the ocean may be higher due to the higher LCOF over the ocean. However, it is also demonstrated which is at a higher elevation closer to the sea. At noon, the LCOF is higher over the windward side and the crest of the two mountain ranges compared to other regions, and during the night there is a clear negative gradient of LCOF towards the east.

6.4. Climaological outcome from the satellites and stations observations

The passage outlines the use of MSG data to study LLCC through the implementation of DMS and NMS schemes for cloud representation. The identification of LLCC employing instrument channels of SEVIRI is analysed, highlighting distinctions between daytime and nocturnal observations. The piece examines changes in LLCC patterns during the day and night, impacted by factors such as sun glint and local tropospheric conditions. It also explores the influence of topography on cloud formation, particularly around the

Chaillu and Cristal mountains. Furthermore, the study displayed the diurnal cycle of cloud cover in the WEA region, observing cloud formation during the night and increased convective activity in the afternoon. Additionally, the study noted regional variations in LLCC, including those over the ocean, coastal regions, windward and leeward sides, and plateau to the east. Overall, the satellite observations are consistent with the surface station data, offering a comprehensive overview of the cloud coverage in the study region.

This chapter analyses the cloud product Geoprof, derived from the CALIOP instrument on the CALIPSO satellite and the CPR instrument on the CloudSat satellite. The distribution of LCOF over WEA is examined, revealing an east to west positive gradient during the night. The text also examines variations in LCOF over different physical features, such as mountains and coastlines, during both day and night. The discussion examines the vertical distribution of cloud occurrence frequency, highlighting the influence of surface characteristics on cloud formation and persistence. Cloud patterns over land and sea are distinguished, taking into account aspects such as potential turbulence and radiation. Furthermore, the text investigates the impact of orography on LCOF and notes a greater occurrence along mountain ranges and peaks, as well as differences between observations during the day and night. The section shows the distinguishable patterns of cloud distribution noticed during the day and at night. It offers insights into the complex interactions between atmospheric conditions and geographical features in the WEA region.

7. ICON Modelling: Case Studies

This chapter analyses the behaviour of the LLCC in WEA during the extended dry season, along with its associated parameters, using NWP simulations. We investigate changes in the model's behaviour under different settings, assessing how closely it corresponds to the observations and achieving a modelled state of the atmosphere that is both physically and dynamically reasonable. Our study focuses on the sources, sinks and the advection of moisture, as well as the treatment of moisture in the deep and shallow convection schemes and with only explicit convection in the NWP model. We differentiate between three main settings in our case study: parameterised convection with parameterisation of both deep and shallow convections, hybrid convection with only shallow convection parameterised, and explicit convection with no convection parameterisation at all. This study was conducted from 14 July 2018 at 0000 UTC to 21 July 2018 at 0000 UTC. The choice of dates was based on a brief investigation of cloud cover by the NMS and DMS, demonstrating typical cloud conditions during that period. Furthermore, the high observational data availability from upper-air soundings during this period was crucial.

7.1. Description of the weather situation

This section describes the weather conditions during the case study period. Figure 7.1 illustrates the averaged streamline anomaly at 925 hPa on the 14th, 15th, 17th, and 18th July 2023, with reference to the wind flows in July and August from 1940 to 2022. Figure 7.2 displays the NMS and DMS at four different times during the case study. On the 14th, the anomaly in WEA is insignificantly different from the climatological average. The flow continues over the Chaillu mountains and into the Republic of Congo (RC), as shown in Fig. 2.2. Over the ocean, the anomaly is south-southwesterly. This indicates a somewhat weaker southerly wind and most likely a warmer SST because of the associated weaker Benguela Current (Nelson, 1992). In the far northeast of the domain, a convergence zone indicates convective systems over the RC and the DRC. The convective systems are also

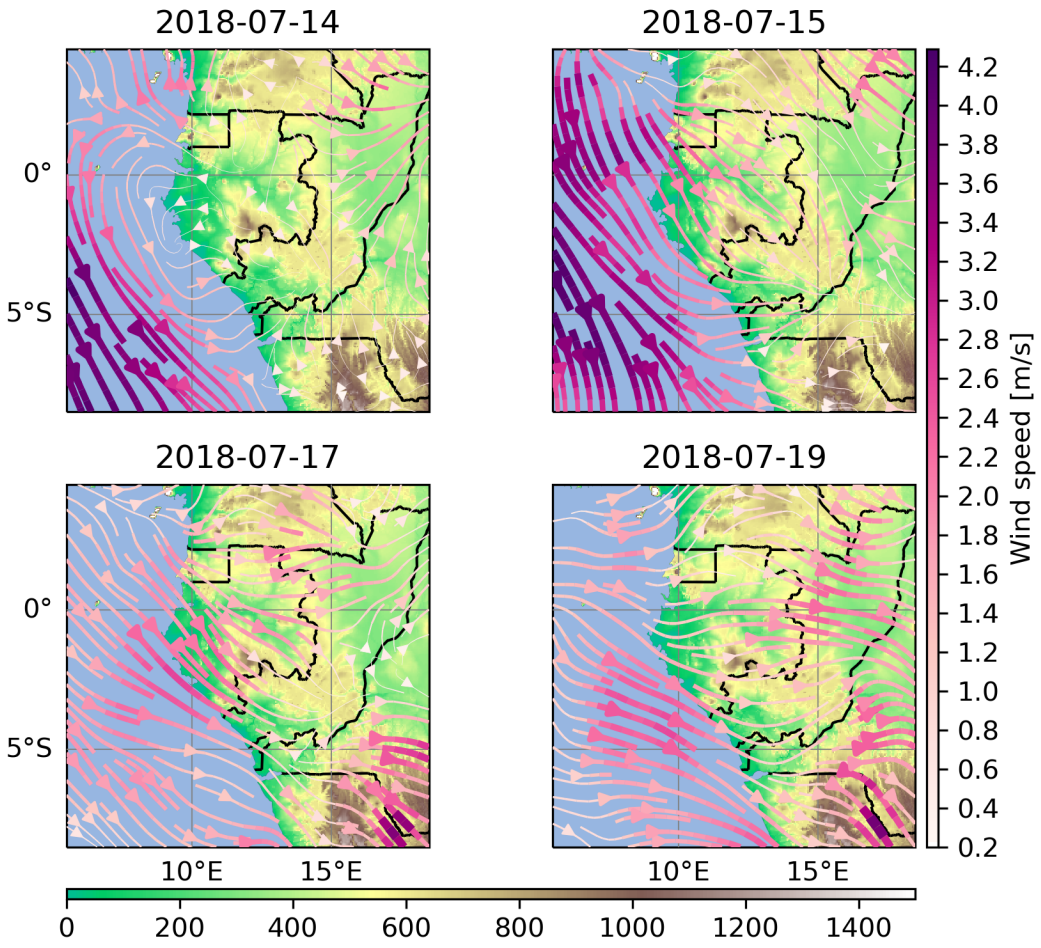

Figure 7.1.: Streamline anomalies daily averaged. The references are the years 1940-2022 in July and August based on ERA5 (Hersbach et al., 2020) in Fig. 2.2.

visible in the far northeast of the domain in the NMS (see Fig. 7.2a). The Batéké plateau, the leeward side of the Chaillu mountains, and the eastern part of Gabon and the RC are cloudless or have broken cloud covers. The coastal areas of Gabon are covered by LLCC.

On 15th July, there was a slight change in the weather. The anomaly of northwesterly flow over the ocean extends (see Fig. 2.2). The southerly winds at 925 hPa could come to a stop. The upwelling of deep ocean water along the coast was prevented, resulting in warmer SST. The streamflow anomaly over Gabon is southeast. The wind along the coastal area was blowing mainly from the west instead of the south. The increased potential for convection may result from a warmer and more humid boundary layer. At 2300 UTC on 15th July, numerous LLCC are observable during the night (see Fig. 7.2b). Mid-level clouds are arriving from the East. The mid-level clouds originate from the convective situation in

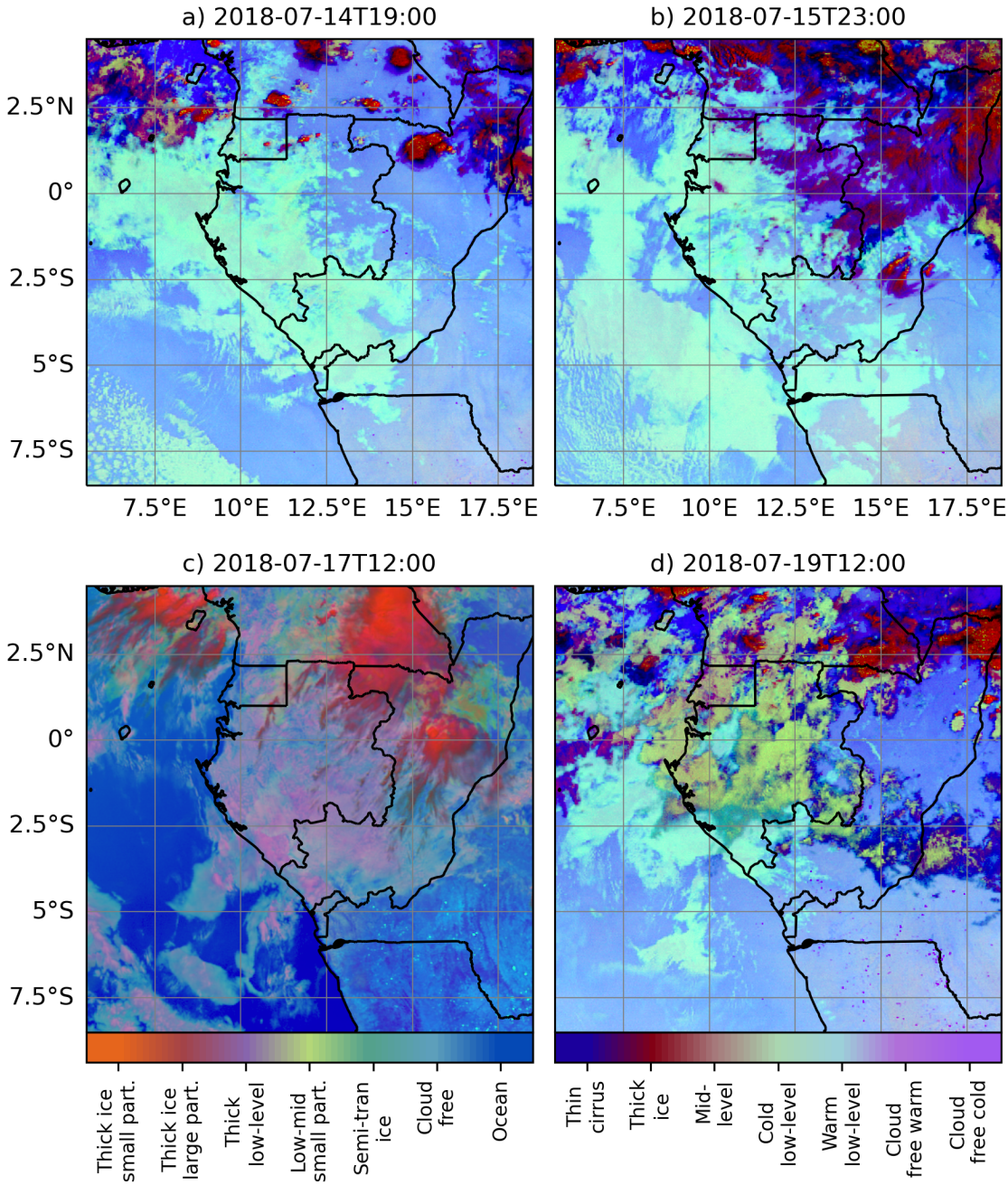

Figure 7.2.: NMS and DMS at four different times during the case study period.

the eastern region. These clouds are then transported towards the west in the middle to top troposphere. The ocean was widely covered by LLCC, with some break up patterns noted along the coastline. From the windward side to the leeward side and across the Batéké plateau, low-level clouds do not provide complete coverage of the sky.

On the 16th of the month, there are changes in streamline anomalies in comparison to those that occurred two days prior. The northwesterly anomaly strengthens and intensifies the westerly wind. Despite this, the stream flow anomaly weakens over the ocean and is now stronger from the west instead of the north. The LLCC remains dense throughout the whole Gabonese territory. Convective systems pass towards the Northwest over the RC and southern Cameroon. We observe the outflow of mid-level clouds towards Gabon.

On 19th July, the anomaly in the airflow over the ocean changes direction to the west-northwest (see Fig. 2.2). The climatological west wind flows no longer experience inhibtion. Over WEA, Gabon and the RC, the wind on 925 hPa is stronger from the West. A LLCC was observed on the western Gabonese territory, which was partially covered by mid-level clouds (see Fig. 7.2d). To the west of Gabon, over the Atlantic, one can observe LLCC in combination with mid-level-altitude clouds and a few high-altitude clouds.

In summary, the synoptic weather situation fluctuates daily. The LLCC from the coast over the Chaillu mountains remains persistent with occasional disruptions. However, the convective system in the far East of the region, extending from the northern Congo basin to Cameroon, exhibits greater variability with outflows at mid and high-levels towards Gabon.

7.2. Set-up of NWP

Numerical weather prediction aims to simulate a range of physical and dynamic processes, from large-scale flow to microphysics, in an attempt to represent reality. However, certain processes prove challenging to replicate or are too small to be resolved by the model's resolution (see Chapter 5). Therefore, various approaches, schemes, and simplifications are employed to substitute processes that cannot be directly represented in simulations. The setting configurations utilised in this particular study are detailed in Chapter 5 and tab. 5.2. The main focus is on predefined options for explicit, hybrid, and parameterised convection.

7.2.1. Regions, transects and points of interest

For further analysis, WEA has been divided into five subregions based on their topographical circumstances and their model specific interest concerning convection. These regions include the coastal region, which encompasses the area adjacent to the Atlantic Ocean; the

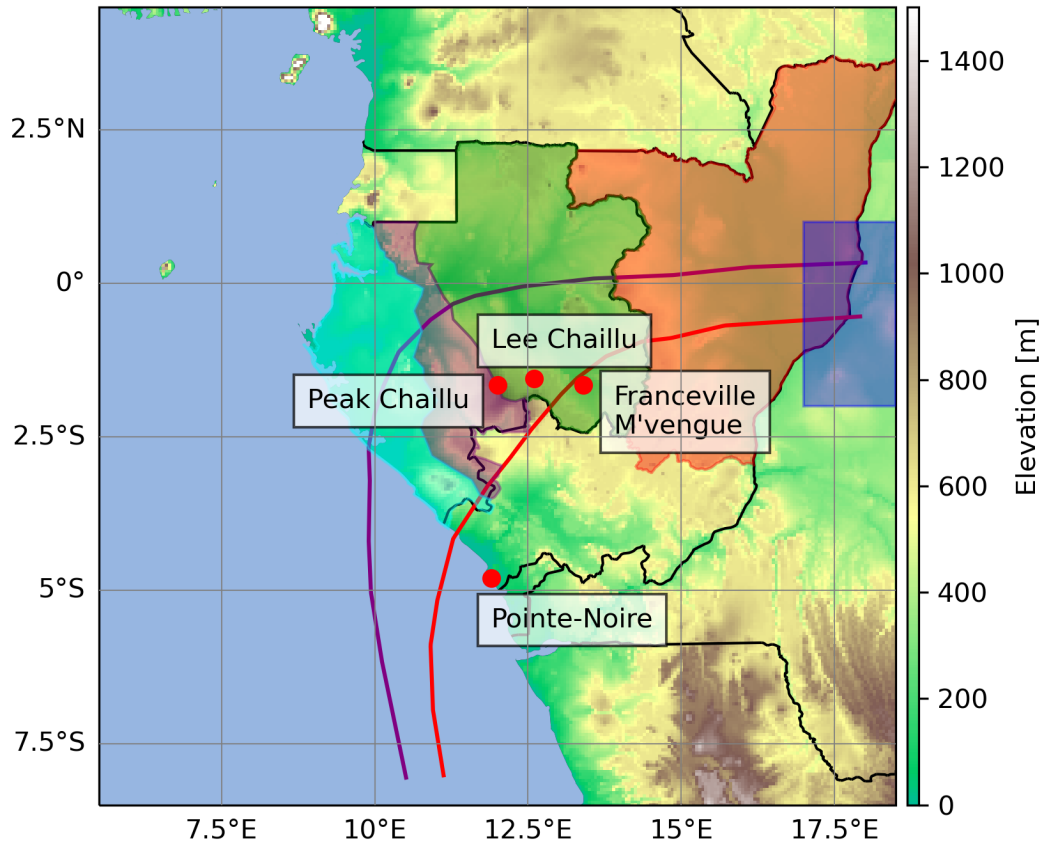

Figure 7.3.: Western Equatorial Africa including five subregions, two transects and four point of interests for further analysis: Coastal region (cyan), windward side of the Chaillu mountains (purple), the plateau region (green), the Northeast of the Republic of Congo (red) and a rectangle in the very east at the domain boundary (blue). The two transects: over the Chaillu mountains (red) and another along the Ogooué valley (purple). The four points of interest are Pointe-Noire, the highest summit of the Chaillu mountains, a position on the leeward side of the Chaillu mountains and Franceville M'vengue.

windward Chaillu, where the wind blows uphill over the Chaillu mountains; the Plateau, which consists of the leeward side of the Chaillu, incorporating the Batéké plateau and the Ivindo-Ogooué plateau; the northeast of the RC and a rectangle at the very East of the domain from 2°S - 1°N and 17 - 18°E (see Fig. 7.3). One of the transects traverses Chaillu (red) whereas the other follows Ogooué valley (purple). The four locations of interest are

Pointe-Noire, the highest peak in the Chaillu mountain range, a location on the leeward side of the Chaillu mountains, and Franceville M'vengue.

7.3. Validation of the case

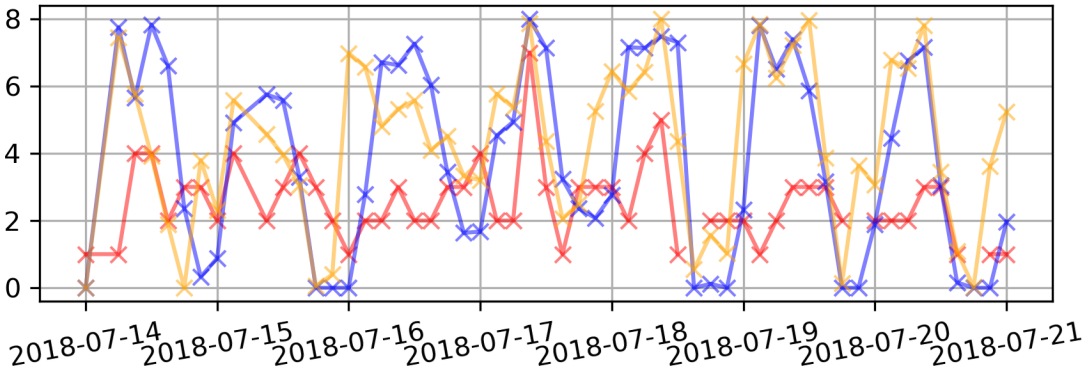

Figure 7.4.: Low-level fraction comparison with NWP comparison at Pointe-Noire.

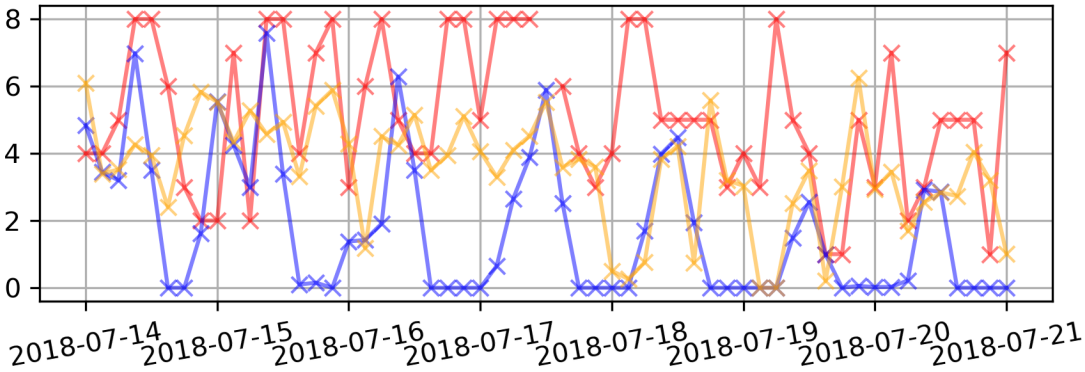

Figure 7.5.: Low-level fraction comparison with NWP comparison at Franceville M'vengue.

The first step involves validating the simulation by comparing the LLCC of the NWP data with the synoptic weather observation data. Figure 7.4 presents the differences in LLCC between the parameterised and explicit simulations, as well as the observations taken during the period in Pointe-Noire. It is noteworthy that both simulations exhibit a stronger diurnal cycle in contrast to the observations. The parameterised convection simulation indicates a higher tendency for LLCC in the morning, while the explicit simulation does not, resulting in an earlier cloud breakup. The simulations follow a typical diurnal cycle, with LLCC increasing in the night and morning, and decreasing in the afternoon. Both

parameterised and explicit simulations exhibit similar LLCC patterns. However, our observations do not accord with these findings, as LLCC rose on the 14th, 17th, and 18th, albeit not consistently each day.

Farther inland from the coast in Franceville M'vengue, a comparison is made between LLCC observations and simulations (see Fig. 7.5). The observations in Franceville illustrate higher levels of LLCC compared to the simulations. The expected diurnal cycle is clearly visible in the observations. However, the parameterised simulation indicates significant clearing in Franceville during the afternoon, which is not observed. The explicit convection includes a greater proportion of low-level cloud cover than the parameterised simulation, although not as high as the observed values. Clearing also occurs here, but not every afternoon.

Overall, the simulations encounter difficulty in forecasting LLCC on the eastside of the domain. The explicit convection displays better agreement with the observations. In contrast, the simulation reports greater variability along the coast, whereas the observations reveal less substantial changes.

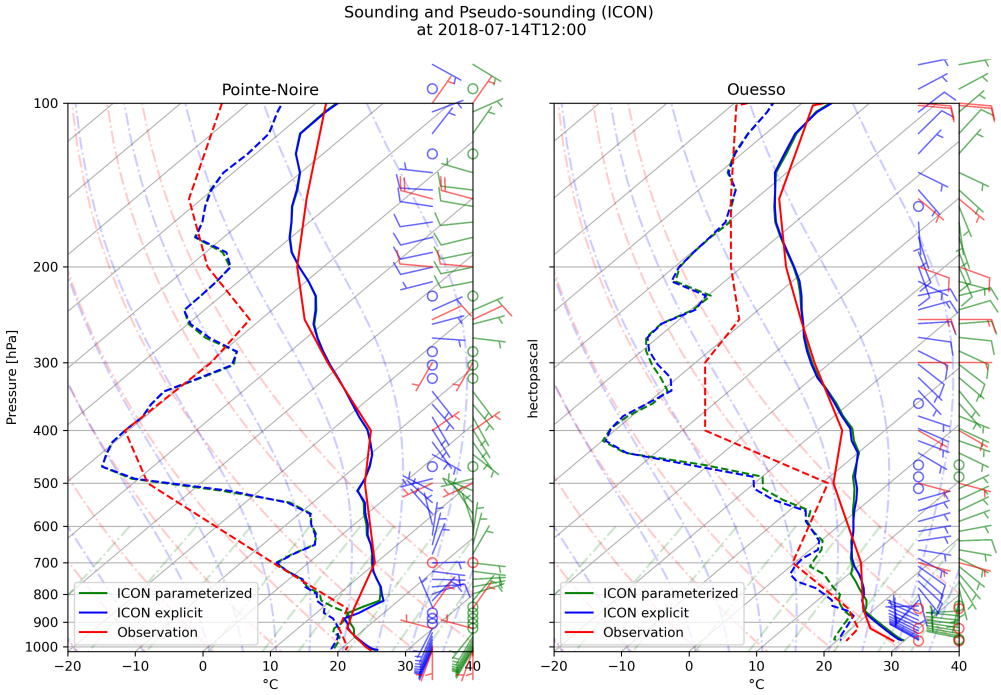

Figure 7.6.: Radiosonde observations (red) at noon in Pointe-Noire (left) and Ouess (right) and the closest vertical profile in the model for the parameterised (green) the explicit (blue) setting at 1200 UTC on the 14th July 2018.

The sounding observations provide a further insight into model validation. Wind direction is particularly well represented at Pointe-Noire. When a weak wind is observed, the noise cannot be represented in the model and differences occur anyway. The observed westerly wind reaches higher altitudes, while the modelled wind has no direction at $900hPa$ above Pointe-Noire. At Ouesso, there is no observed wind direction in the lower layers, while the model shows weak westerly winds up to $825hPa$. Above, the troposphere's wind is driven westwards in both the observations and the model. Humidity in the lower layers is difficult to predict. The model shows an underestimation of the surface humidity at Pointe-Noire, while there are no major differences between the parameterised and the explicit simulations. In Ouesso, the parameterised version shows a remarkably lower dew point temperature compared to the explicit run. Slight differences are also visible in the temperature profile.

Overall, the soundings show us the different shape of the modelled and observed atmosphere. A broader view of more soundings during the whole case study can be found in the appendix.

7.4. Behaviour under different convection regimes

This section shows the different behaviour of certain parameters under the three different settings of explicit, hybrid and parameterised convection. The analysis includes the regional analysis above, vertical insight along transects, vertical profiles of certain parameters over time, and moisture budget analysis of some regions.

7.4.1. Low-level cloud cover differences between model experiments

The low-level cloud fraction parameter (clcl) in the ICON model is a diagnostic variable, indicating the actual cloud coverage in the lower atmosphere. Figure 7.7 illustrates variations in clcl, contingent on the convection parameterisation settings employed in the simulations. The difference between the simulations with fully parameterised convection and only explicit convection is shown in Figs. 7.7a and b. Then, the comparison between conducting hybrid simulations with solely parameterised shallow convection and only explicit convection is depicted in Figs. 7.7c and d. Finally, Figs. 7.7e and f demonstrate the contrast in clcl between hybrid and explicit convection.

Figure 7.7a and b illustrate the contrast between all explicit convection and complete explicit convection and present a clear image of the whole WEA. LLCC is more prevalent

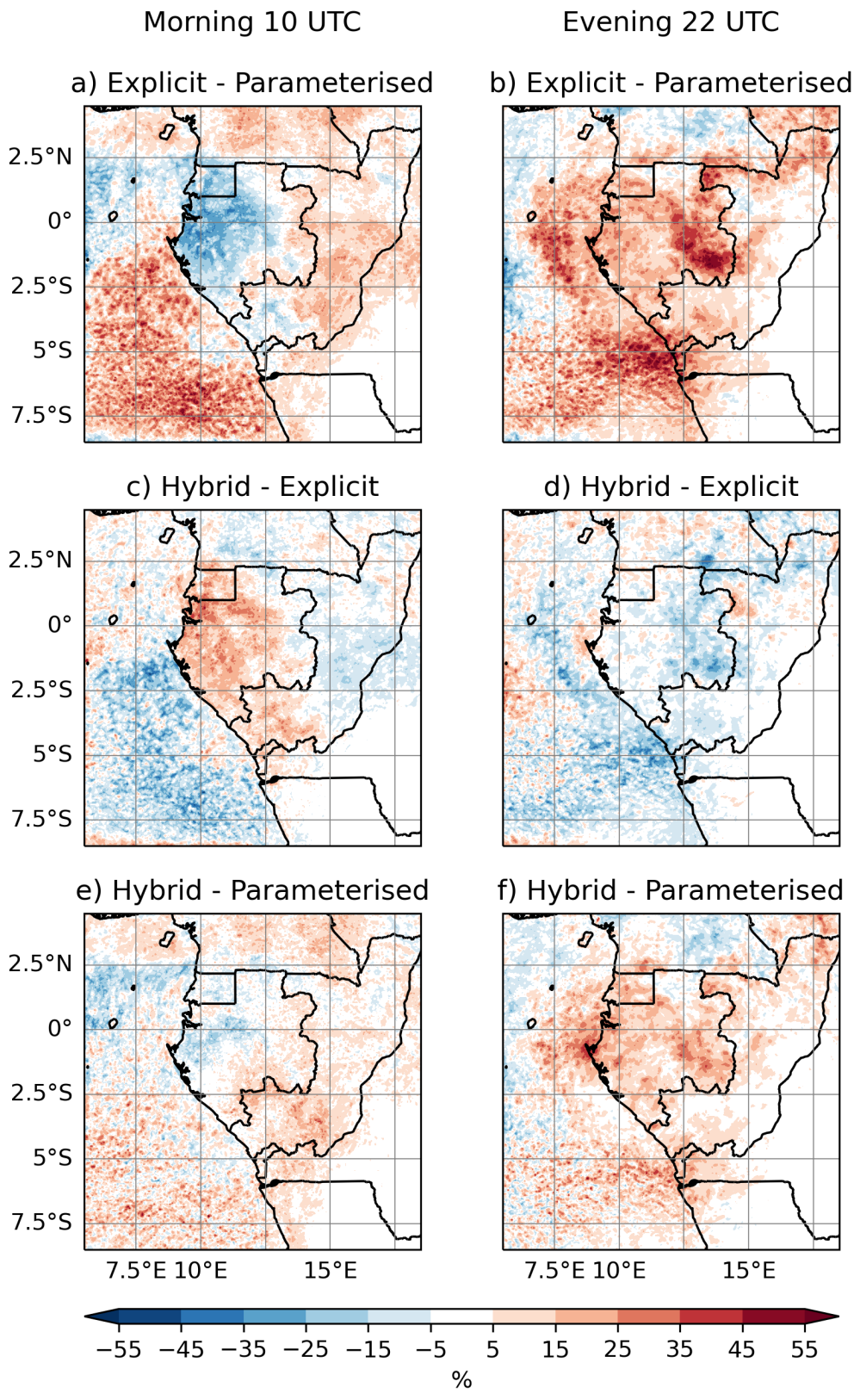

Figure 7.7.: Low-level cloud cover differences between the different convection settings (parameterised, hybrid, explicit) in the morning at 1000 UTC and the evening at 2200 UTC.

over the ocean in simulations with the parameterisation switched off, which is consistent throughout the simulated period. Nonetheless, this difference is less pronounced in the late afternoon and evening, as shown in Fig. 7.7b. Moreover, there is a higher occurrence of LLCC over Gabon at night in the explicit simulation. In the morning, the simulations utilizing the parameterised convection scheme show more clouds compared to the explicit one (see Fig. 7.7a). This is evident across the windward side, over the peak, on the leeward side of the Chaillu mountains, along the coastal regions, over the Ogooué valley, and partially over the plateau. Outside Gabon, the simulation using the parameterised convection scheme demonstrates a lower level of low-level cloud cover. During the rest of the day and night, the explicit convection simulation has a higher amount of LLCC.

When comparing the hybrid format with explicit deep convection and parameterised shallow convection while having all convection schemes enabled, a spatially similar image is obtained but with less extreme results (see Fig. 7.7c, d). More LLCC is produced over the entire WEA region when the parameterisation of deep convection is turned off. The only exception is in the morning from the windward side of the Chaillu and Cristal mountains up to the coast, where there is less equal LLCC. Over the sea, deep convection parameterisation generates fewer clouds. Still, some areas in the northern part of the region experience an increase in cloud production through deep convection parameterisation. However, there is almost a complete absence of low-level clouds in the southeastern part of the region, resulting in no discernible difference.

The comparison between the hybrid simulation and the simulation with all convection schemes switched off reveals a distinct outcome (see Fig. 7.7e, f). In the morning, the shallow convection schemes generate additional clouds over Gabon, similar to the deep convection scheme. The LLCC is also larger in the southern RC near the ocean during the morning. However, in the afternoon and night, the amount of LLCC is greater in the explicit convection simulation, albeit with a weaker disparity. Over the southern ocean within the region, simulations featuring explicit shallow convection indicate a more pronounced LLCC layer in early night. However, the distinction is less significant and noteworthy throughout the rest of the diurnal cycle.

7.4.2. Precipitation differences between model experiments

The amount of precipitation is highly dependent on the model settings. The difference between using parameterised convection or not is illustrated in fig. 7.8a. The explicit convection simulation yields greater precipitation amounts over the leeward side of the

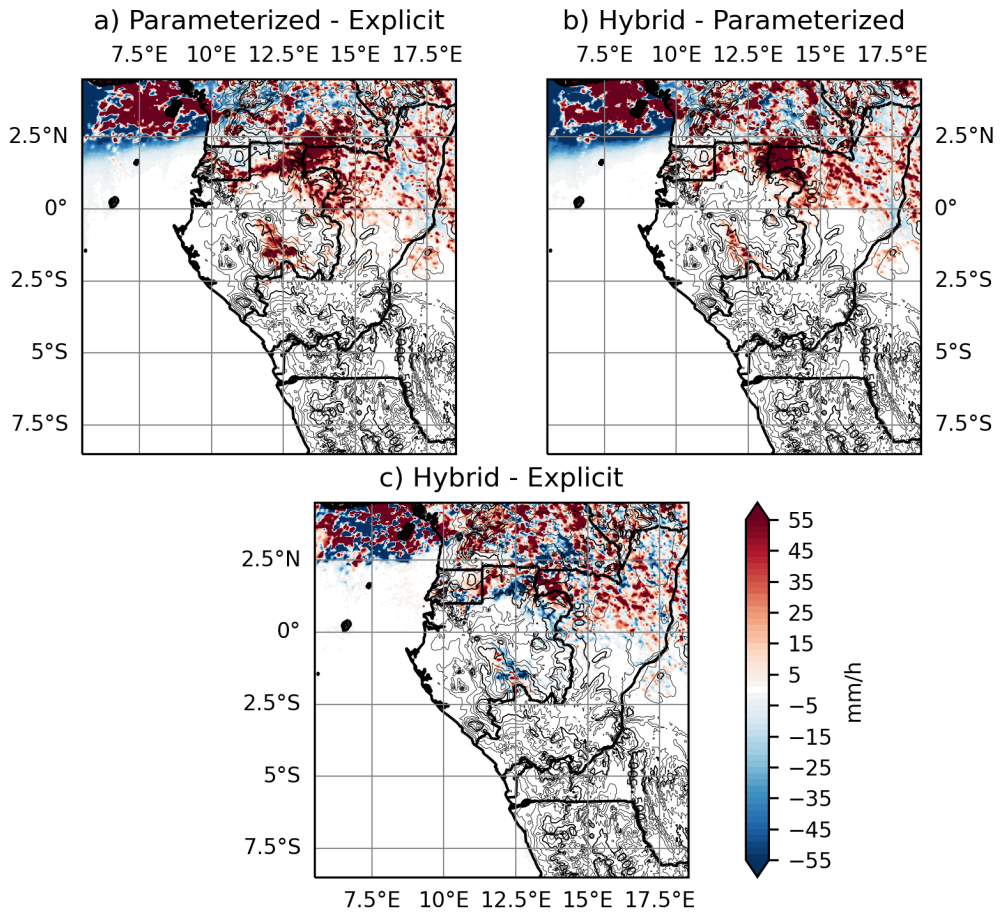

Figure 7.8.: Total precipitation difference between different settings (parameterised, hybrid, and explicit convection), after 174 hours of time integration.

Chaillu mountains than the convective Tiedtke scheme. This pattern also holds for the triangle of Cameroon, Gabon, and RC. Across the Gulf of Guinea, precipitation is widely distributed in the parameterised simulation, with some areas experiencing higher levels of rainfall when convection is switched off. This indicates that the absence of convection results in more evenly distributed precipitation, while the parameterised case produces more frequent outbreaks of rainfall. This pattern is also observed in the northeastern section of the domain, albeit to a lesser extent. Notably, neither simulation yields any rainfall over the southern half of the domain.

When comparing the simulation using parameterised convection with the hybrid form that uses parameterised shallow convection and explicit deep convection, there are notable differences (see Fig. 7.8b). The complete parameterisation results in minimal

precipitation in comparison to the hybrid form over the leeward side and crest of the Chaillu mountains. The northern region of RC has a slightly lower difference in precipitation. This indicates that there is lower precipitation in the simulation utilizing the deep convection scheme than the hybrid simulation. The image is noisy in the northern part of the simulated area. This indicates that there is lower precipitation in the simulation utilizing the deep convection scheme than the hybrid simulation. Both simulations have high levels of precipitation noise. Small-scale convective-driven precipitation is challenging to accurately predict in the correct location using NWP. Consequently, such precipitation-types are expected.

Focusing on the data presented in Fig. 7.8c, it is clear that there is a substantial similarity in precipitation patterns between the hybrid form which includes parameterised shallow convection and the completely explicit convection model. The discrepancy between the two is attributed to the utilization of shallow convection parameterisation. In the leeward side of the Chaillu mountains, the precipitation is locally displaced, but not with a large difference from region to region. Similarly over the triangle of Gabon, Cameroon, and RC, the precipitation appears locally different but without significant differences within the area. There is no clear over-representation of precipitation in one simulation compared to the other.

Parameterised deep convection significantly decreases precipitation in WEA. When shallow convection is also parameterised, precipitation reduction is even greater. Convection schemes generate convective rain, which is the primary driver of convection. In simulations where we disable the schemes, precipitation actually increases. At first glance, this appears to contradict the schemes' working principle. However, further discussion on this issue will follow in the subsequent sections.

7.4.3. Transects of different model experiments

The transects provide a vertical view of the atmosphere. Figure 7.9 shows the southern transect following the streamlines along the 850 hPa. At 1000 UTC, there are no significant disparities in liquid water content among the three simulation settings (parameterised, hybrid, and explicit convection). While along the leeward side of the Chaillu mountains the parameterised version shows a thicker cloud deck at 1000 UTC (see Fig 7.9a), the hybrid version is fragmented in LLCC (see Fig 7.9c) and the explicit convection simulation even stronger (see Fig 7.9e). In regards to the ocean, the simulation with explicit convection exhibits solely more LLCC at 1000 UTC (see Fig. 7.9a). Furthermore, the high density

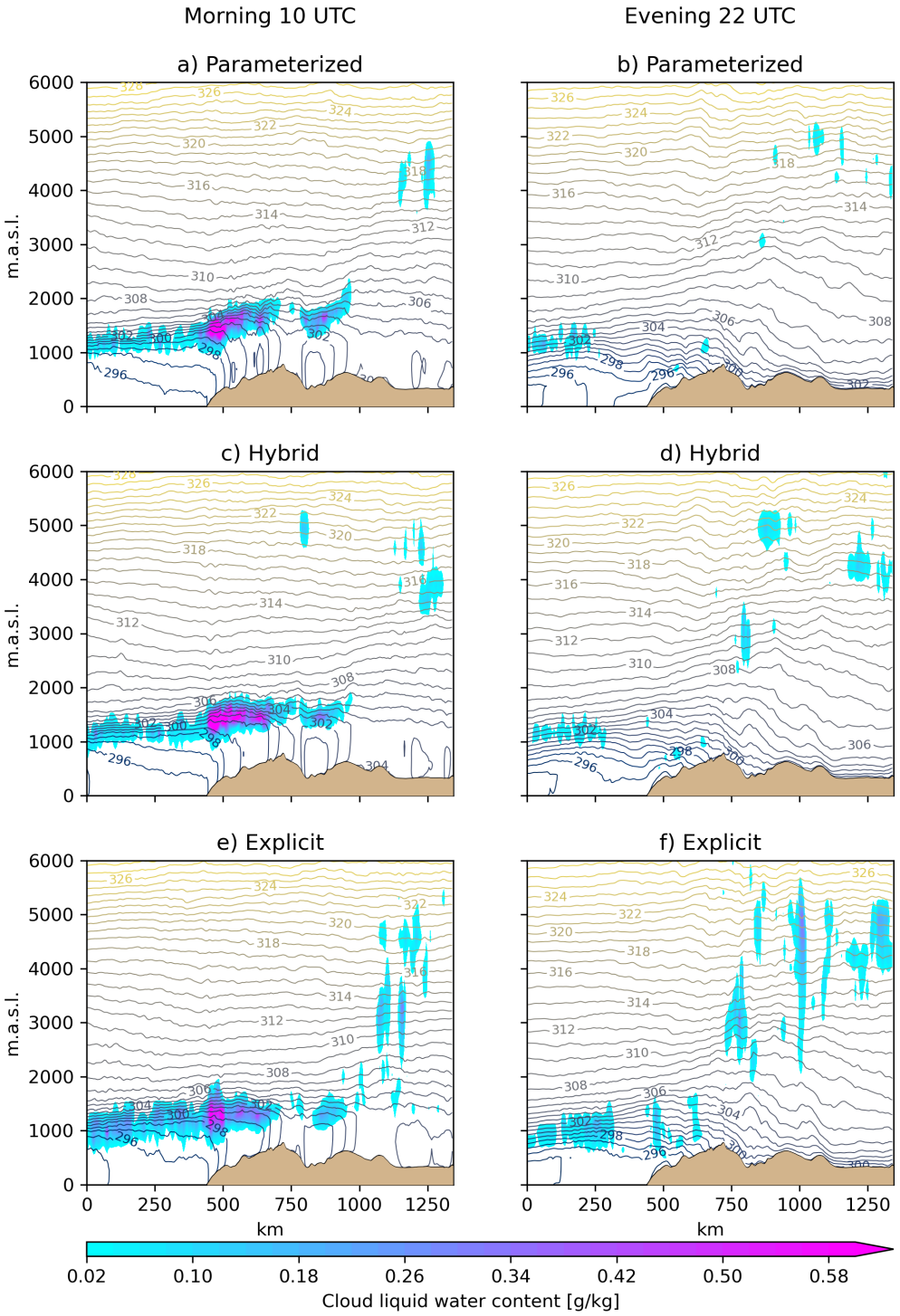

Figure 7.9.: Transect over the Chaillu mountains of cloud liquid water content [g/kg] mean at potential temperature [K] mean at 1000 UTC (left) and at 2200 UTC (right) for the settings parameterised convection (a & b), hybrid convection (c & d), and explicit convection (e & f).

of potential temperature levels at lower heights suggests a lower boundary layer height compared to the hybrid simulation and the simulation with parameterised convection. At 1000 UTC, the boundary layer over the transect on land is warmer in the simulation with explicit convection (see Fig. 7.9e). This could be as a result of the fact that less dense cloud decks allow more energy to pass through, further enhancing the break-up of clouds. In all three simulations, a notable stratification of the lower troposphere over the ocean, in contrast to that over land, is observed. The simulation featuring parameterised convection shows the strongest stratification.

Towards the evening and night, at 2200 UTC, the simulation featuring explicit convection exhibited a greater number of LLCC along the transect in contrast to the hybrid and parameterised versions. The convective episodes resulted in precipitation over the Chaillu mountains, with certain areas displaying cloud remnants, as depicted in Fig. 7.9. At the far end of the transect, there is even liquid water present in the atmosphere at an altitude of 5000 m.a.s.l. (see Fig. 7.9f), which is much less in the parameterised convection simulation. In the hybrid simulation, precipitation over the Chaillu mountains occurs slightly later as compared to the explicit version (see Fig. 7.9e, f). However, this is significantly lower in the simulation using parameterised convection. Nonetheless, in the parameterised version, there is almost no precipitation over the Chaillu mountains. LLCC is larger over the ocean at 1000 UTC in the explicit and convective simulations than in the hybrid version (see Fig. 7.9c, d). This non-linearity may be due to a hysteresis effect. In the simulation with explicit convection, water has precipitated and formed new clouds. However, in the hybrid version, cloud formation has not occurred yet. Moreover, in the parameterised version, there has been less precipitation (see Fig. 7.8), although clouds are still present (see Fig. 7.9a).

The morning situation along the northern and southern transects is comparable. In the simulation incorporating parameterised convection, the amount of cloud liquid water is greater than in the hybrid simulation, and substantially higher than in the simulation relying exclusively on overland explicit convection (see Fig. 7.10a,c,e). When activating the deep convection schemes, the low-level cloud dissipation in the morning is slightly stronger. The positive radiation feedback intensifies the effect. In the simulation that entails explicit convection, the LLCC is notably fragmented (see Fig. 7.10e). The radiation feedback is more prominent in this scenario. Additionally, the cloud deck is elevated in the hybrid version when compared to the explicit version (see Fig. 7.10c,e), thus demonstrating the mixing abilities of the deep convection scheme. There are no significant differences in the

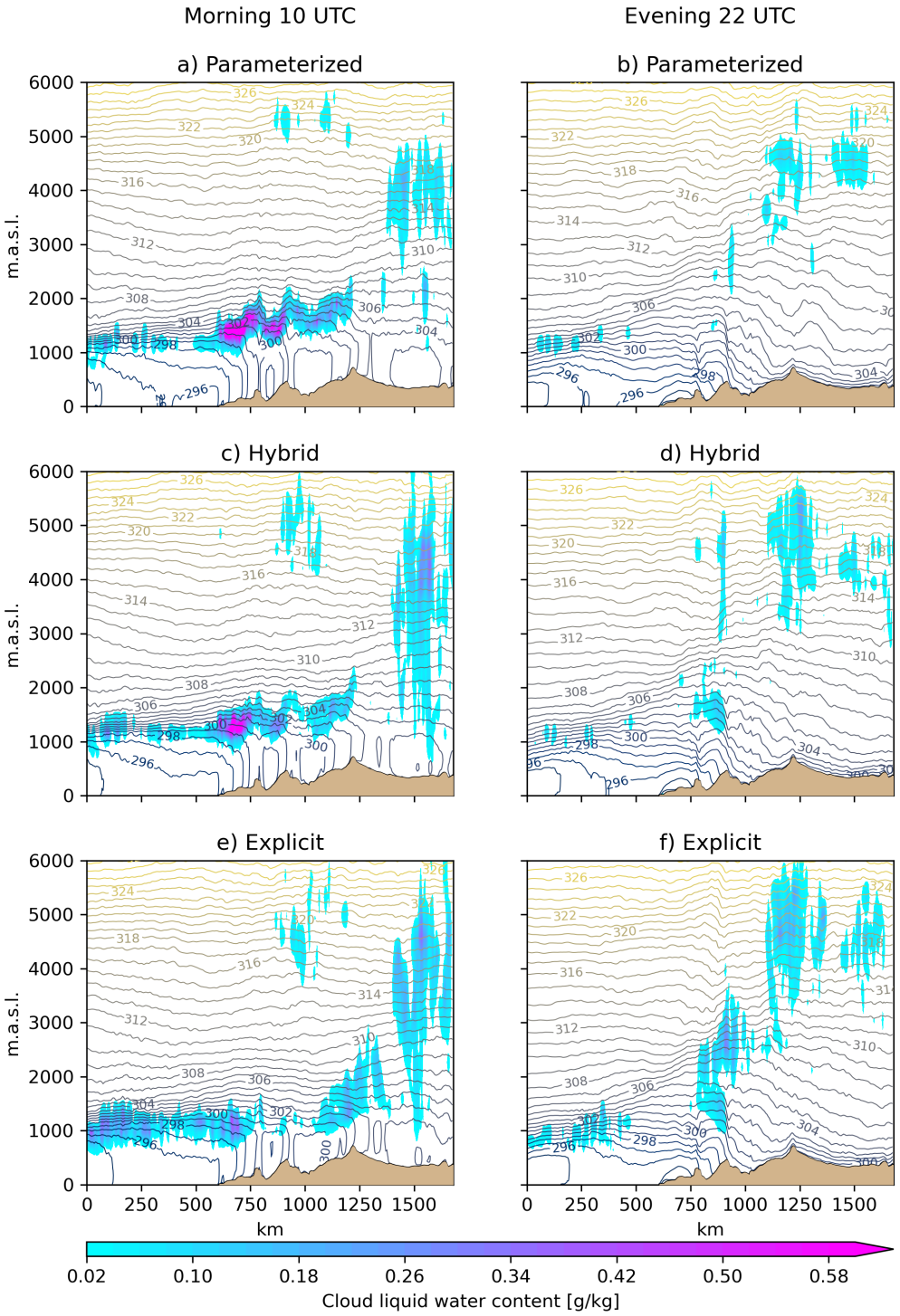

Figure 7.10.: Transect along the Ogooué valley towards east of cloud liquid water content [g/kg] mean at potential temperature [K] mean at 1000 UTC (left) and at 2200 UTC (right) for the settings parameterised convection (a & b), hybrid convection (c & d), and explicit convection (e & f).

boundary level height or cloud height between the hybrid and parameterised versions (see Fig. 7.10a,c). The boundary layer in the explicit simulation is warmer over land compared to other simulations. Increasing the elevation appears to trigger cloud formation. In the far east, beyond the final peak of the transect, the liquid content of cloud water is minimal. In the far east, beyond the final peak of the transect, the liquid content of cloud water is minimal. There are still some higher-reaching clouds, perhaps a relic from an earlier convective situation. This is most prominent in the simulation with explicit convection. In the oceanic region, the explicit convection simulation manifests the densest low-level cloud deck, similar to the southern transect.

Shifting attention to the early morning at 1000 UTC, the LLCC is virtually nonexistent for the parameterised simulations (see Fig. 7.10b,d,f). Cloud formation is seen only over the northernmost regions of the Chaillu mountains, owing to orographic lifting. The hybrid version displays a more pronounced impact in this direction. Over the eastern peak, there is cloud precipitation in the hybrid and even stronger in the explicit simulations. However, there is no precipitation in the parameterised version (see Fig. 7.10e,f). After around 900 km along the transect, the boundary layer becomes unstable in the explicit convective simulations, which may lead to a convective cell later on. In the hybrid simulation, there is even a towering cloud due to deep convection. There is not much LLCC over the ocean. While the explicit convective simulation contains a certain amount of liquid water content at lower levels, the hybrid parameterised exhibits lower levels of liquid water content, and the hybrid almost entirely lacks liquid water content (see Fig. 7.10b,d,f).

The transects of both paths demonstrate the vertical distribution of moisture and stability. Convection schemes mix air into the boundary layer, leading to the drying out and lifting up of the boundary layer height. This makes the process of cloud formation more challenging. Furthermore, less mixing leads to higher energy in the boundary layer, resulting in increased convective activity in simulations without convective active schemes.

7.4.4. Time-height profiles at various locations

Another approach for analysing the weather situation in this case is to examine pseudo-soundings over time. This methodology aims to comprehend the atmospheric alteration above a specific point of concern. Here, we examine Pointe-Noire in RC as a coastal representation of our domain, the peak of the Chaillu mountains in the 3rd domain of the

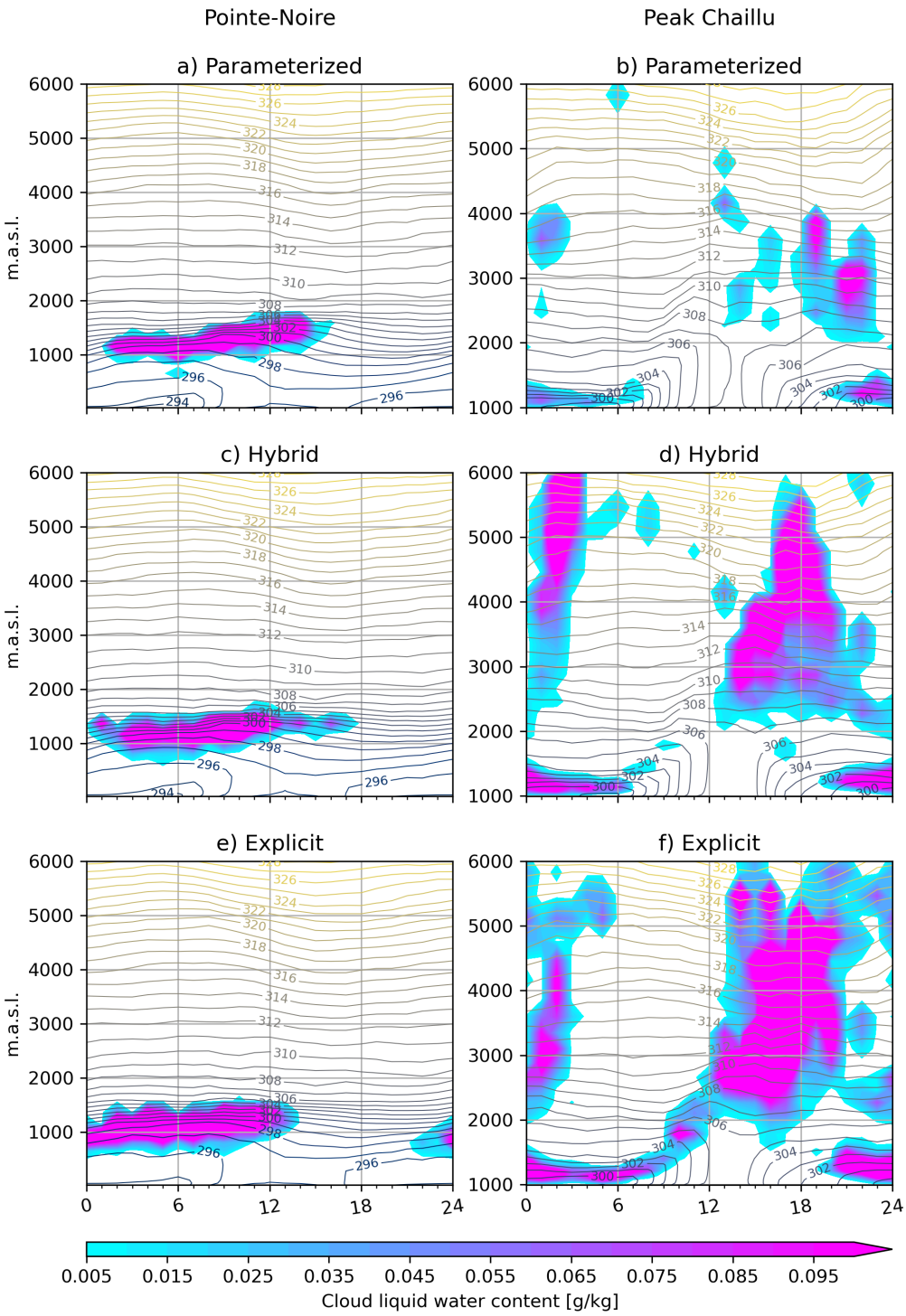

Figure 7.11.: Vertical profiles of the diurnal cycle at Pointe-Noire (left) and the peak of the Chaillu mountains (right) of cloud liquid water content [g/kg] mean and potential temperature [K] mean for the settings: parameterised convection (a & b), hybrid convection (c & d), and explicit convection (e & f).

ICON topography (1°39′*S*, 12°00′*E*), and Franceville M'vengue as a representation of the Batéké plateau situated behind the leeward side of the Chaillu mountains (see Fig. **??**).

Figure 7.11 illustrates the diurnal cycle at Pointe-Noire, simulated with parameterised convection (a), hybrid convection (c), and explicit convection only (e). It can be seen from the data that the parameterised convection caused a lift in the low-level cloud layer over Pointe-Noire by 100 to 300 metres. Further analysis reveals a more stratiform mixed layer for the explicit convection scheme and a slightly stronger mixed layer for the hybrid parameterisation than for the fully parameterised convection simulation (see Figs. 7.11a, c, & e). In addition, the temperature at the surface in the parameterised convection simulation is lower. The findings suggest that the simulation with explicit convection dissolves the low-level cloud layer earlier than the hybrid and parameterised convection. Hence, decreased explicit convection in the presence of parameterised convection results in less cloud breaking in the morning. The shallow convection scheme incorporates a larger volume of air above the boundary layer, thereby expanding it. Consequently, in the simulation with explicit convection, the cloud deck is taller during the morning. The reason for this phenomenon is the larger day-to-day variability in the simulation with explicit convection (see Fig. A.10). There is no evidence to suggest that precipitation occurs in Pointe-Noire in any of the three simulations.

At the summit of the Chaillu mountains, the diurnal cycle differs from that in Pointe-Noire (see Fig. 7.11). In each of the three simulations, a cloud layer develops at lower levels post sunset, which lasts until the morning. Whilst the simulation utilizing parameterised and hybrid convection shows that the LLCC decreases in intensity during the morning and transitions into a clear sky phase, the explicit convection simulation shows that the LLCC transitions into a higher reaching convective cloud phase with precipitation (see Fig. 7.8). However, the simulation with parameterised convection generates mid-level clouds in the afternoon and evening with minimal precipitation. The night and early morning cloud layer is consistently observed near the surface in all three simulations. This data supports the theory of orographic cloud formation during the night, when maritime air is pushed eastward and lifted over the Chaillu mountains. Locally, the weather may even be foggy. Notably, the simulation with the deep convection scheme turned on (see Figs. 7.11b & d) varies from the other simulation in terms of the amount of clouds present in the afternoon. The deep convection scheme produces fewer clouds, which is somewhat counterintuitive for a convection parameterisation scheme. The reason for this remains unclear from these results, but it may be related to the workings of the parameterisation

schemes. The deep convection scheme transports moisture upwards, releasing energy and potential latent heat higher up in the atmosphere. This factor could serve as a valve, reducing high energy at the surface.

To the leeward side of the Chaillu mountains and in Franceville, the weather is less cloudy than over the crest of the Chaillu mountains (see Figs. 7.12 & 7.11). The cloud deck is more persistent in the morning over the leeward side of Chaillu mountains with the parameterised convection than with the hybrid simulation (see Figs. 7.12a & b). Additionally, the simulation using explicit convection does not display a morning cloud deck over the leeward side of the Chaillu mountains. The cloud coverage visible towards the windward side of the Chaillu mountain tends to dissipate over the leeward side (see Figs. 7.9a & c). Cloud water may evaporate on the way to this point. However, the simulation with explicit convection displays a stronger convective troposphere which produces more clouds in the afternoon (see Fig. 7.12f) and stronger precipitation (see Fig. 7.8) compared to the parameterised version. Additionally, the parameterised version exhibits a higher surface temperature (up to $2K$). This result can be attributed to the fact that warm air can hold more water vapor than cold air. The lower temperatures in the explicit simulation promote water condensation, resulting in the release of latent heat near the surface. The graph in Fig. 7.15c displays a higher total vertically integrated water content (TQV) for the explicit convection simulation, which leads to an increase in cloud cover. Local moisture convergence may be a contributing factor, brought on by the updraft generated by the convection. The towering clouds observed in the explicit runs suggest this to be the case. However, an increase in moisture must have a source. An example of a possible source could be the surface, which receives more radiation and consequently has a higher moisture flux into the atmosphere. The compensation for this could then be the precipitation, which is stronger in the explicit convection simulations. Further details on the fluxes will be provided in the next subsection.

Overall, the simulations with parameterised convection display a more prolonged persistence of the cloud cover in comparison to the simulations with explicit convection schemes. Throughout all simulations, the cloud formation process is initiated along the windward side of the Chaillu mountains due to orographic lifting, and it persists downstream over the crest and the plateau. The explicit convection schemes promote stronger precipitation. The convective clouds in these simulations ascend to higher altitudes. The parameterisation schemes mix air above the boundary layer, thickening it to dilute the moisture over a greater amount of air.

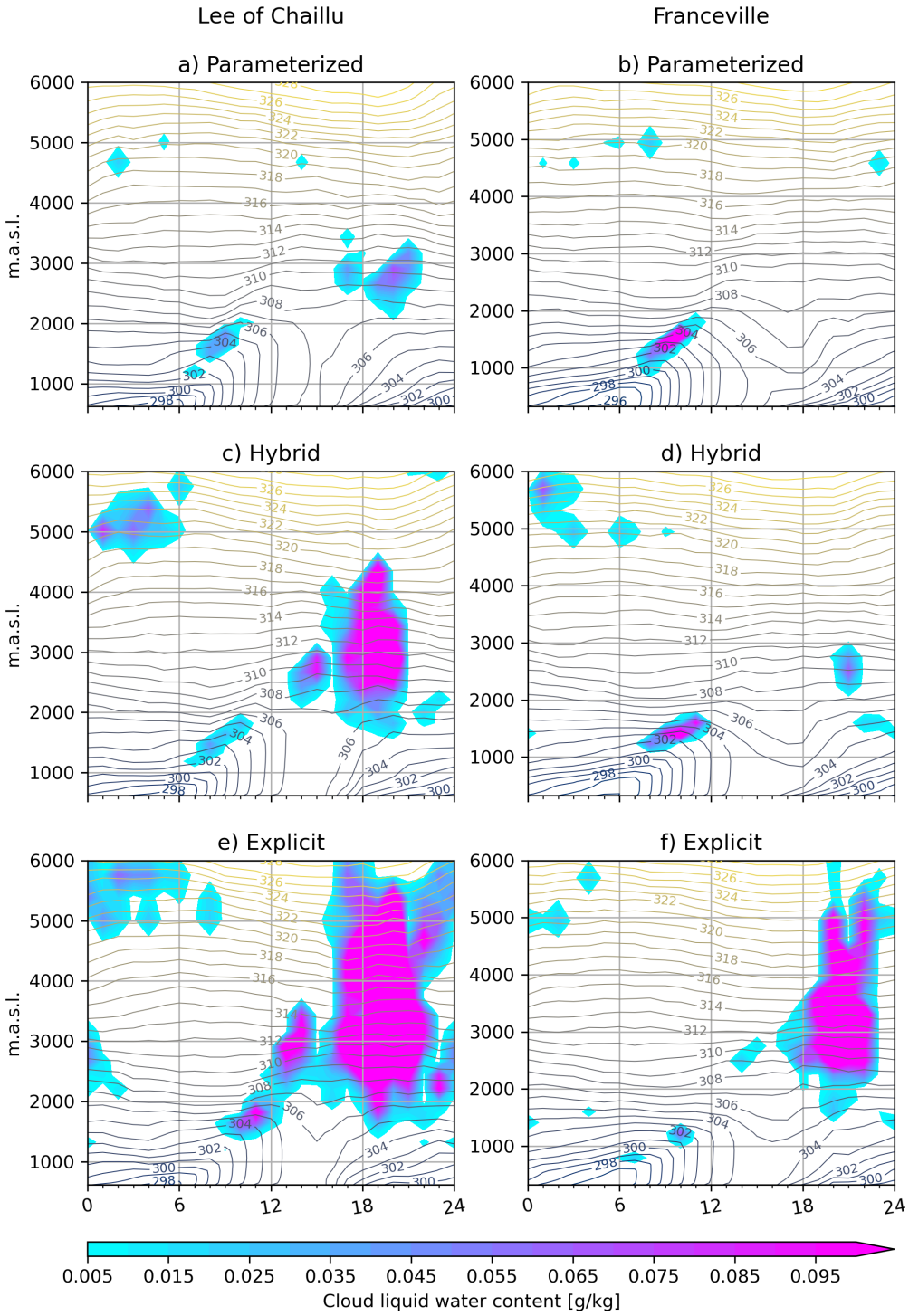

Figure 7.12.: Vertical profiles of the diurnal cycle at the leeward side of the Chaillu mountains (left) and Franceville (right) of cloud liquid water content [g/kg] mean and potential temperature [K] mean for the settings: parameterised convection (a & b), hybrid convection (c & d), and explicit convection (e & f).

7.4.5. Humidity and surface fluxes - latent and sensible heat

When turning our attention towards the surface fluxes, differences between simulations become apparent. The latent heat flux from the surface to the atmosphere, (negative values due to the inverse representation of the variable in the ICON model) is generally higher in the simulation with explicit convection (see Figs. 7.13a, 7.14a & 7.15a). This provides evidence for a slightly greater surface moisture flux in the explicit simulations, which may account for the elevated water vapour content observed in these runs. The sensible heat flux also exhibits a higher flux in the explicit simulations, too (see Figs. 7.13a, 7.14a & 7.15a). The radiation in the parameterised version is less able to penetrate the cloud layer than in the explicit run where convection breaks up the cloud deck. The difference in the dew point temperature additionally supports this asserttion, but mainly over the summit of the Chaillu mountains (see Figs. 7.14b & 7.15b) . While the deviation in dew point temperature between the explicit and parameterised convection runs stabilises during the night (see Figs. 7.15b), the explicit convection simulation experiences a stronger and earlier uptick in dew point temperature shortly after sunrise, compared to the parameterised convection simulation.

Overall, the flux analyses support the hypothesis that there is greater moisture transfer from the surface to the atmosphere with explicit convection only. Moreover, the dew point temperature corroborates this hypothesis, as it is both earlier and more strongly enhanced in cases of explicit convection only.

7.4.6. Total precipitable water content

At the start of the observed period at 0900 UTC, the differences in Total Column Water Vapour (TQV) are minimal and unsteady. However, over the Gulf of Guinea, in the northern region, the parameterised simulation has greater moisture content (see Fig. 7.16). Approximately at 1200 UTC on the first day, higher integrated water vapor content plumes start to develop towards the East, whereas in the simulation with parameterised convection, the moisture level is lower. This disparity amplifies as the day progresses. At 1500 UTC, the higher moisture levels reach the northeastern part of the RC. In contrast, the explicit simulation shows lower humidity levels for southern Cameroon compared to the parameterised simulation. By 1800 UTC, after sunset, the higher integrated humidity now covers more and more areas. An East to West transportation of moisture occurs,

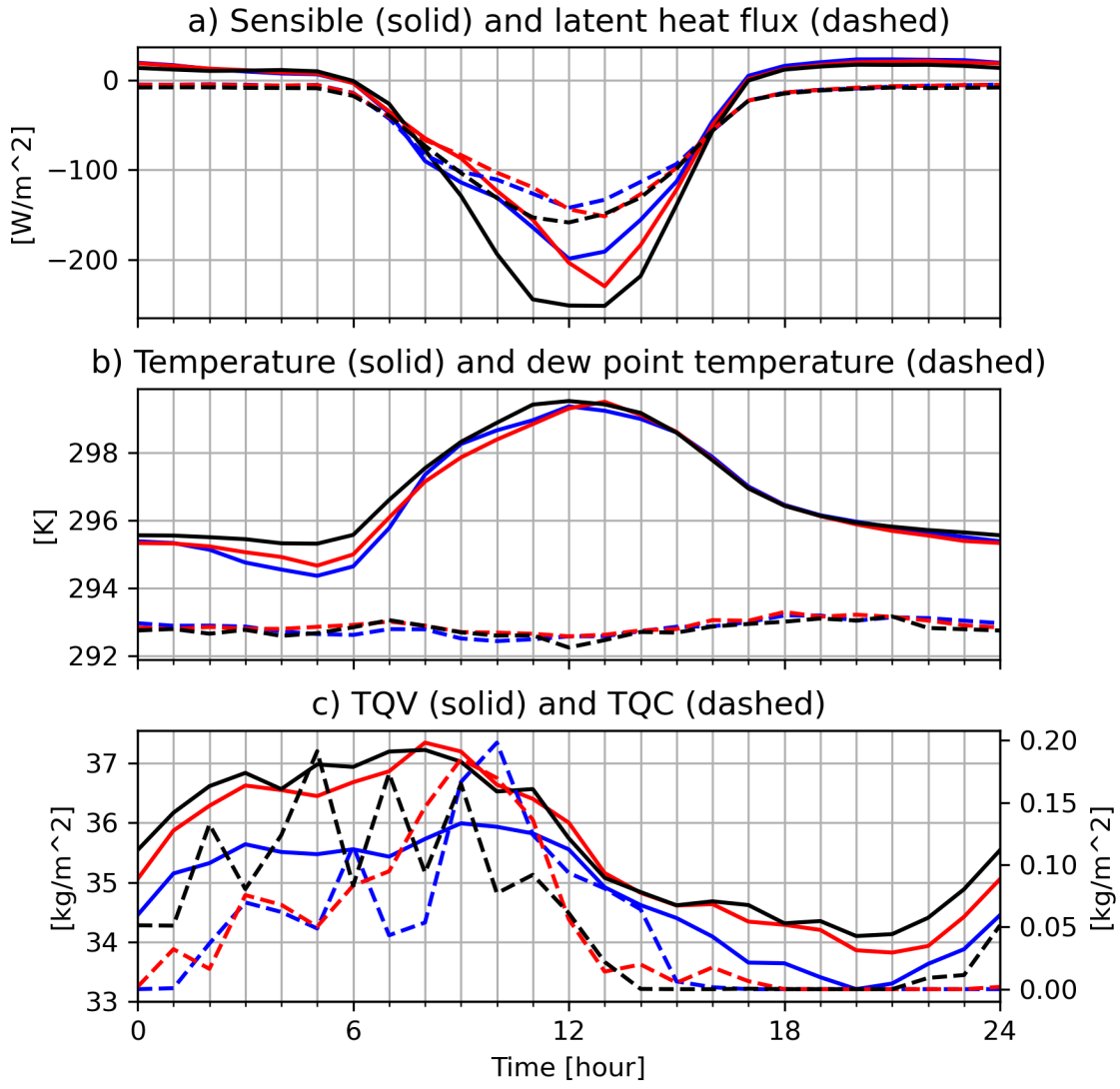

Figure 7.13.: a) Sensible (solid) and latent heat flux (dashed) at Pointe-Noire with parameterised (blue), hybrid (red), and explicit (black) convection. Same color settings in panel b) with 2-m temperature (solid) and 2-m dew point temperature (dashed) and panel c) total integrated water vapor content (solid) and total integrated cloud water content (dashed).

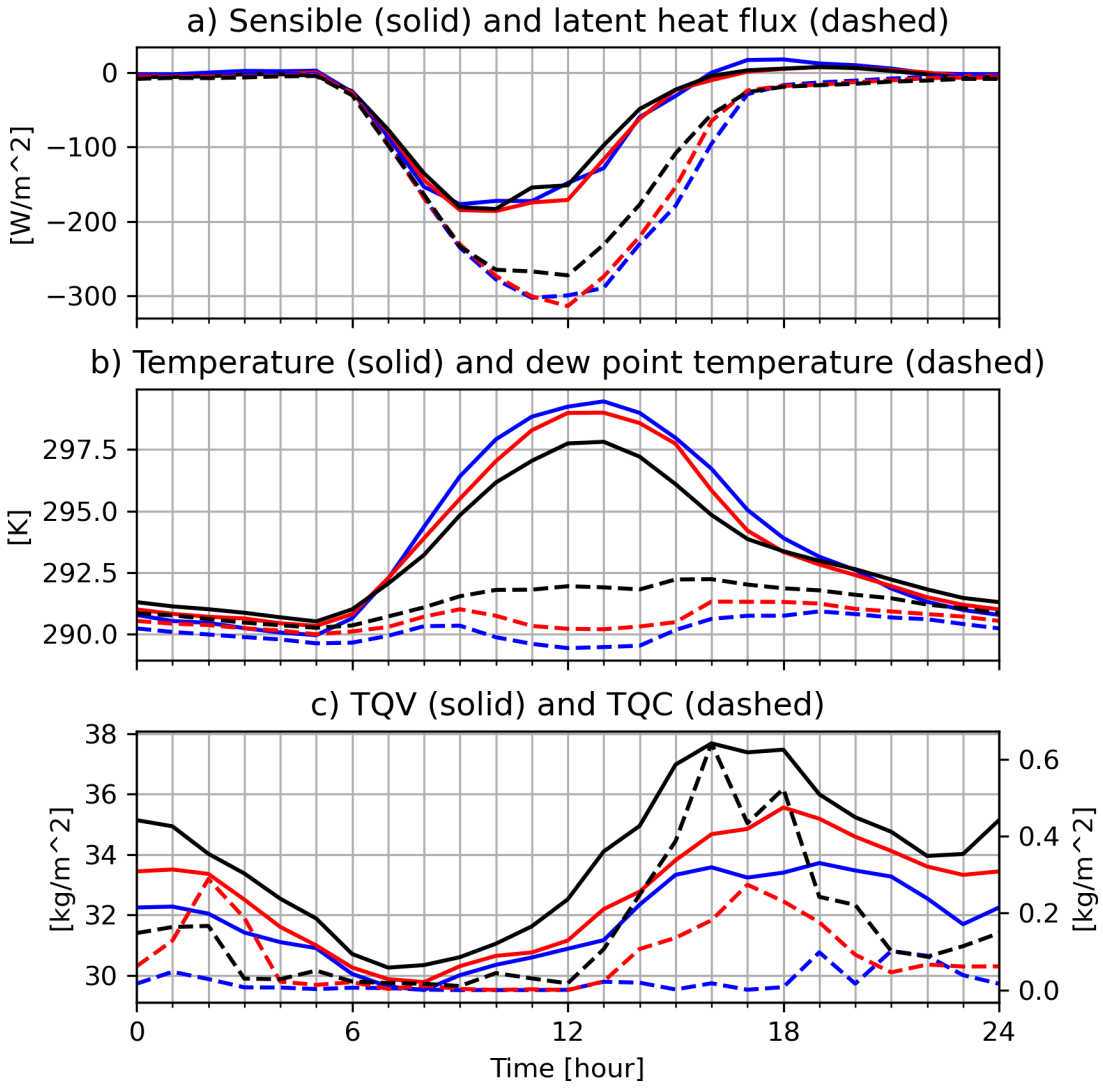

Figure 7.14.: a) Sensible (solid) and latent heat flux (dashed) at the peak of the Chaillu mountains with parameterised (blue), hybrid (red), and explicit (black) convection. Same color settings in panel b) with 2-m temperature (solid) and 2-m dew point temperature (dashed) and panel c) total integrated water vapor content (solid) and total integrated cloud water content (dashed).

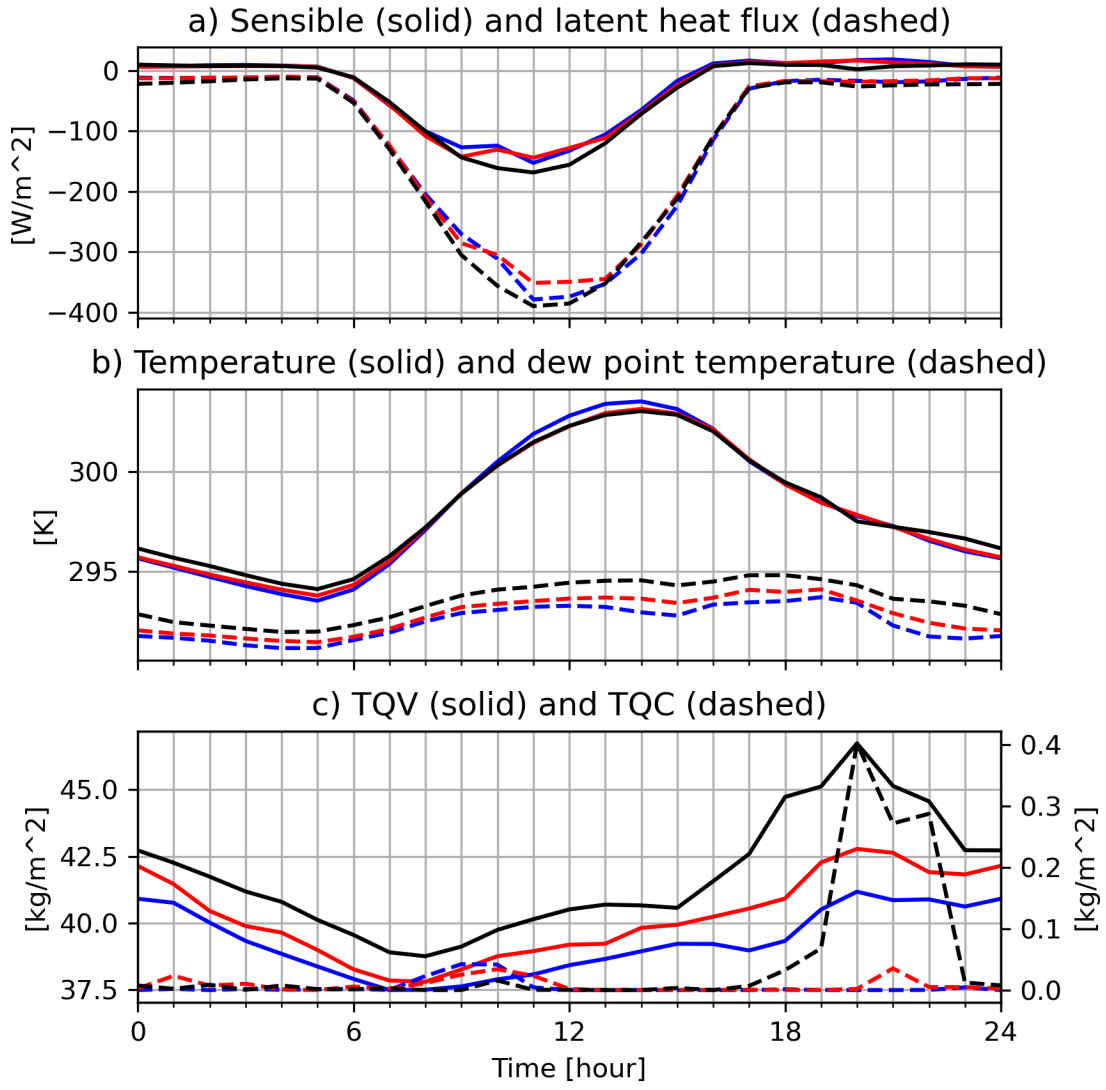

Figure 7.15.: a) Sensible (solid) and latent heat flux (dashed) at Franceville M'vengue with parameterised (blue), hybrid (red), and explicit (black) convection. Same color settings in panel b) with 2-m temperature (solid) and 2-m dew point temperature (dashed) and panel c) total integrated water vapor content (solid) and total integrated cloud water content (dashed).

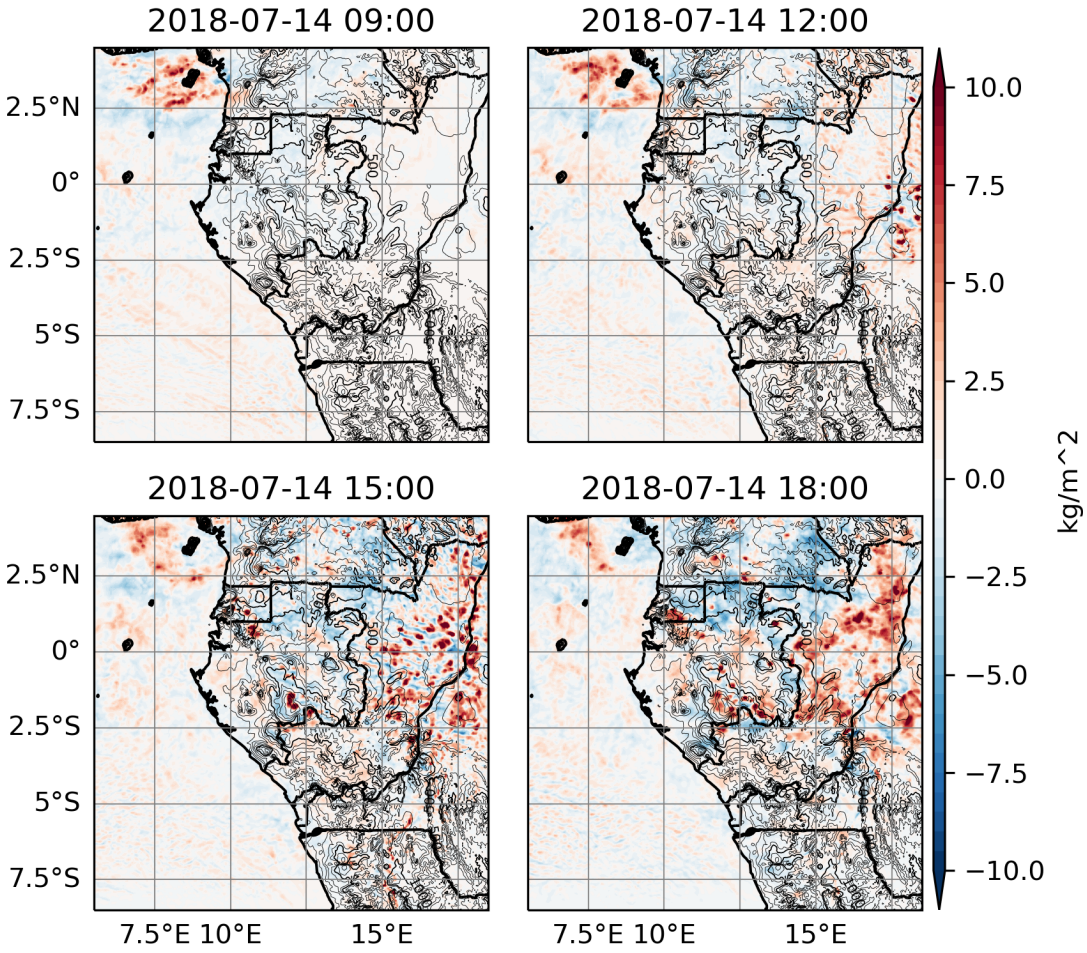

Figure 7.16.: Precipitable water content difference between the simulations with parameterised convection and explicit convection only at certain time frames at the beginning of the study period.

specifically within mid-levels where easterly winds are present. The explicit simulations indicate that the transport is responsible for increased humidity levels in the West.

When taking into account the entire period of separation, the simulation with explicit convection reveals that moisture levels are higher over the majority of our region of interest (see Fig. 7.17). At 0900 UTC, there is a consistent difference in humidity between the parameterised run and the explicit run. By 1600 UTC, numerous small plumes show that explicit simulations experience stronger convection, resulting in moisture convergence in local areas. After sunset, at 2200 UTC, the moisture plumes start to disappear and become even weaker by 0200 UTC (see Fig. 7.17). The explicit simulation demonstrates higher water content across the entire area of interest. In the Gulf Guinea and South Cameroon, the water content is greater for the parameterised simulations, which exhibits typical phenomena resulting from convection parameterisation (see Fig. 7.17). The explicit convection display more precipitation over the Chaillu mountains and the Batéké plateau (see Fig. 7.8a), which reduces the vertical column's water content (see Fig. 7.17). The possible explanation can be the overall increased water content in the explicit simulations as well as the stronger vertical gradient due to the lower mixing (switched off convection parameterisation).

7.4.7. Vertical moisture transport differences between model experiments

From the previous sections, we gained an overview of how moisture is handled by the schemes. Figure 7.18 displays the difference in humidity between the hybrid simulation and the parameterised version on the left-hand side and the hybrid simulation and explicit convection settings on the right-hand side. The moisture differences in the lower troposphere are notable. In the lower portion near the surface, the simulation with explicit convection shows a significantly greater water vapor content than the parameterised run. Conversely, the upper boundary layer in the simulation with parameterised convection has a higher quantity of water vapor. This disparity is not negligible, as it extends up to $5\,g\,kg^{-1}$. While the two sections are separated strictly in the morning, high levels of moisture become apparent in the explicit simulations during the afternoon. Convection enhances the water vapor content throughout the column, resulting in moisture convergence, as discussed in the previous subsection. Hence, the water vapor content is higher across the entire column, with variations in the height of the boundary layer being visible. Already from the ocean, the increased humidity in the parameterised simulations suggests a increased boundary layer height.

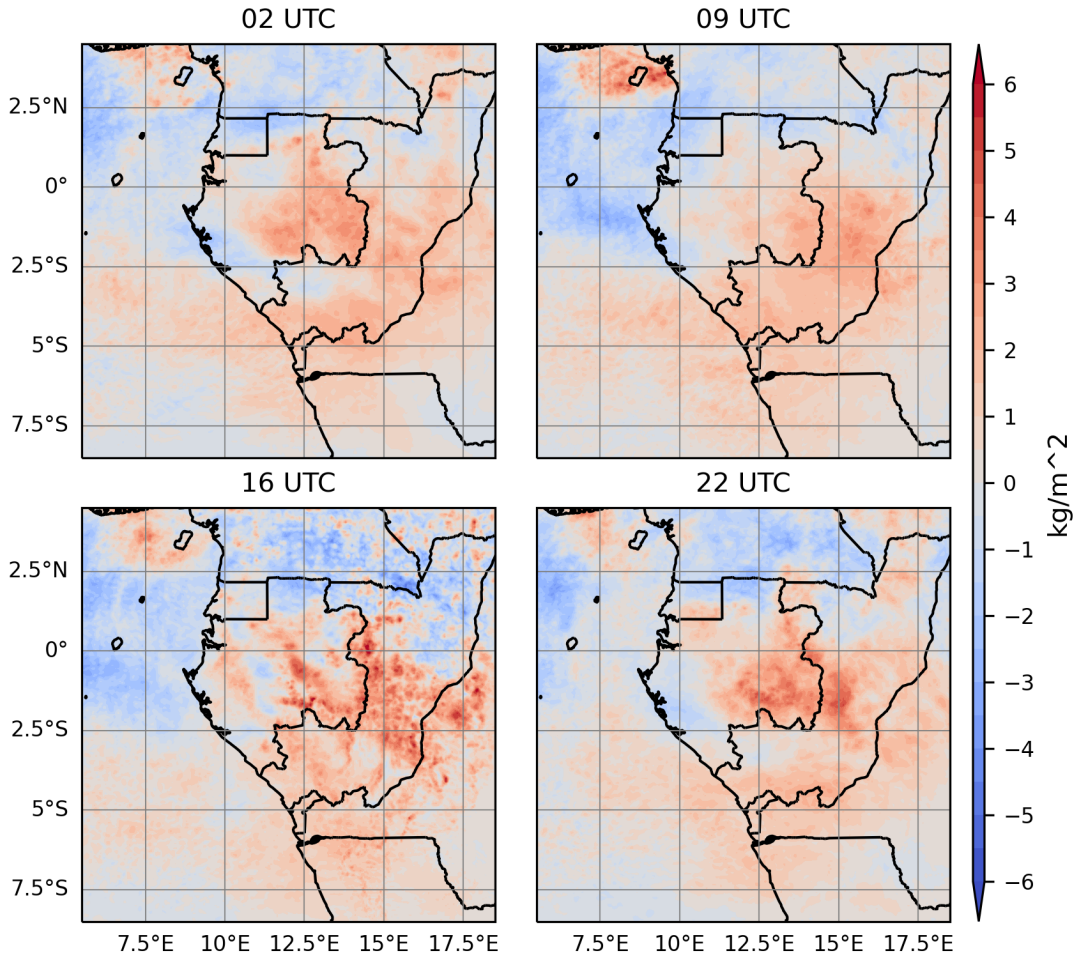

Figure 7.17.: Precipitable water content difference between the simulations with parameterised convection and explicit convection averaged over four times (0200, 0900, 1600 and 2200 UTC) during the study period.

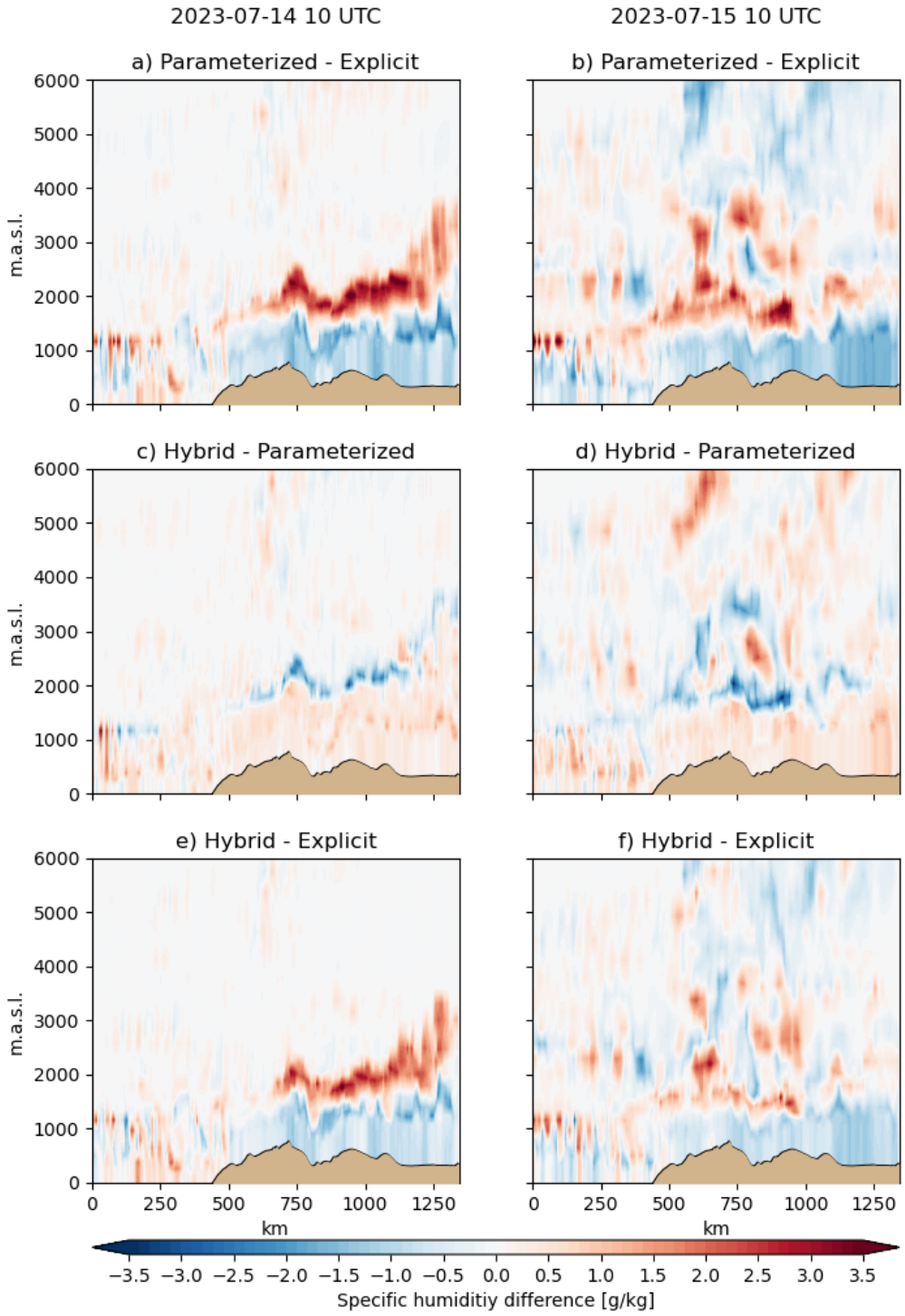

Figure 7.18.: Specific humidity difference [g/kg] on the 14th July 2018 at 1000 UTC (left) and on the 15th July 2018 at 1000 UTC (right) between parameterised and explicit convection (a & b), hybrid and parameterised convection (c & d), and hybrid and explicit convection (e & f) along the transect over the Chaillu mountains.

The convection parameterisation scheme appears to transport moisture upwards in the troposphere by enlarging the height of the boundary layer and mixing in air from the middle troposphere. As a result, the scheme dilutes the boundary layer, leading to fewer convective cells and weaker convection. This can explain the lower precipitation rates observed with a parameterised convergence scheme, as previously noted.

The northern transect presents a comparable image. The parameterised simulation indicates lower humidity in the lower troposphere, up to 1000 m.a.g.l, in contrast to the simulation utilizing explicit convection (see Figs. 7.19a & b). From 2000 to 4000 m.a.g.l., compared to the explicit convection, the parameterised convection shows regions with higher humidity. The deep convection parameterisation transports moisture upwards. The variation is less pronounced compared to the transect over the Chaillu mountains (see Fig. 7.18), apart from two distinct regions at an altitude of approximately 3000 m.a.s.l. At this altitude, an easterly wind prevails. The origin of the increased moisture could potentially be the transport of moisture from the East, although this will be further discussed in the following section.

The distinction between the hybrid and parameterised formats reveals some moisture separation in the lower troposphere, though less pronounced than previously noted (see Figs. 7.19c & d). Notably, the cell farther to the left on the 15th at 1000 UTC stands out as different. As such, while the deep convection scheme does not generate much humidity separation, it does contribute to one of the larger humidity accumulations above the boundary layer. Shifting to a comparison between the hybrid and explicit versions, it is noteworthy that the discrepancies in the lower troposphere are more pronounced (see Figs. 7.19e & f). The enhanced moisture content occurring at around 1100 km along the transect and in the 2000-3000 m.a.s.l. range reveals the impact of the shallow convection scheme on the atmosphere above the boundary layer. When the shallow convection scheme is turned on, the only distinction between the simulations shown in Figs. 7.19e & f appears to be its response for the upward transport of moisture and the expansion of the boundary layer height. Although it produces an area of higher humidity above the boundary layer, this is not as strong as in the deep convection scheme and is more likely to depend on the advection of air masses from the East due to the different wind field in the middle levels.

Taking all presented evidence into account, it appears that the shallow and deep convection schemes have distinct impacts on the lower and middle troposphere behaviour in our area of interest during the dry season. Specifically, the shallow convection scheme appears to be the key driver of vertical humidity separation, while the deep convection

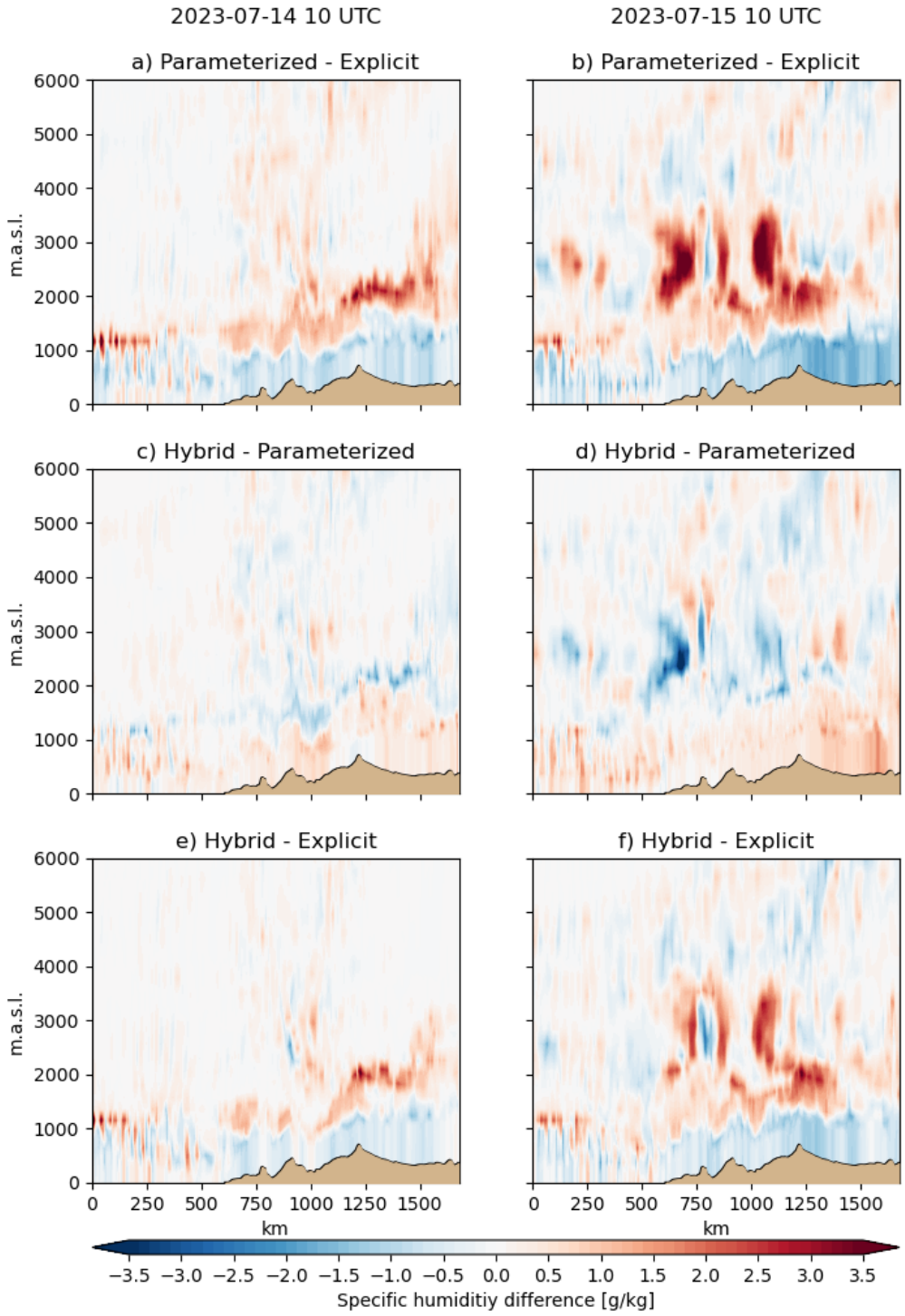

Figure 7.19.: Specific humidity difference [g/kg] on the 14th of July 2018 at 1000 UTC (left) and on the 15th of July 2018 at 1000 UTC (right) between parameterised and explicit convection (a & b), hybrid and parameterised convection (c & d), and hybrid and explicit convection (e & f) along the transect over the Chaillu mountains.

scheme exerts a greater influence on levels between 2000 and 4000 m.a.s.l. A potential reason for the advection of moisture in the mid-levels cannot be displayed by Fig. 7.19. However, more information on this will be presented in the following section.

7.4.8. Humidity budgets

The moisture budget of four distinct regions is presented in Fig. 7.20. The budget illustrates the terms contributing to a change in humidity like convergence, precipitation, and surface moisture flux. The discrepancy between the tendencies in the simulations with explicit and parameterised convection is also illustrated. In the northeastern region of the RC, a noticeable decrease in the difference of absolute moisture levels (indicated by the dotted lines) occurred in the afternoon of July 14th (see Fig. 7.20). This change is primarily influenced by moisture convergence, which is marginally reduced by precipitation. The simulation with explicit convection transports much more moisture into this area, with a major contribution from the eastern flow above the boundary layer (see Fig. 7.20). This pattern persists almost every afternoon and early evening during the analysed period. The precipitation also increases, but it does not equate to moisture convergence. The disparity in surface moisture flux between the two simulations is not substantial (see Fig. 7.20).

The moisture convergence over the Ogooué and Batéké Plateau is less distinct. Convergence typically occurs during the afternoon and early evening, with a drop in the moisture budget during late night and early morning due to convergence. The surface moisture flux is of minor importance.

Along the windward side of the Chaillu mountains, precipitation is higher in the explicit convection-only simulation (see Fig 7.20c). Convergence remains the primary driver of humidity shifts over time, with a more robust convergence leading to slightly higher precipitation amounts in the explicit simulation. On the nights of the 17th and 19th, there were a considerable increases in precipitation on the windward side of the Chaillu mountains in the explicit simulation. However, there was also a noticeable rise in moisture transported to the region.

There is no discernible variation between the explicit and parameterised convection within the coastal region. Moisture change aligns with the convergence curve to a great degree. Precipitation does not occur on a larger scale and does only create a little distinction between the two simulations (see Fig. 7.8a). There are no major differences in surface moisture flux between the simulations and this may not be the most important factor in the difference in moisture content.

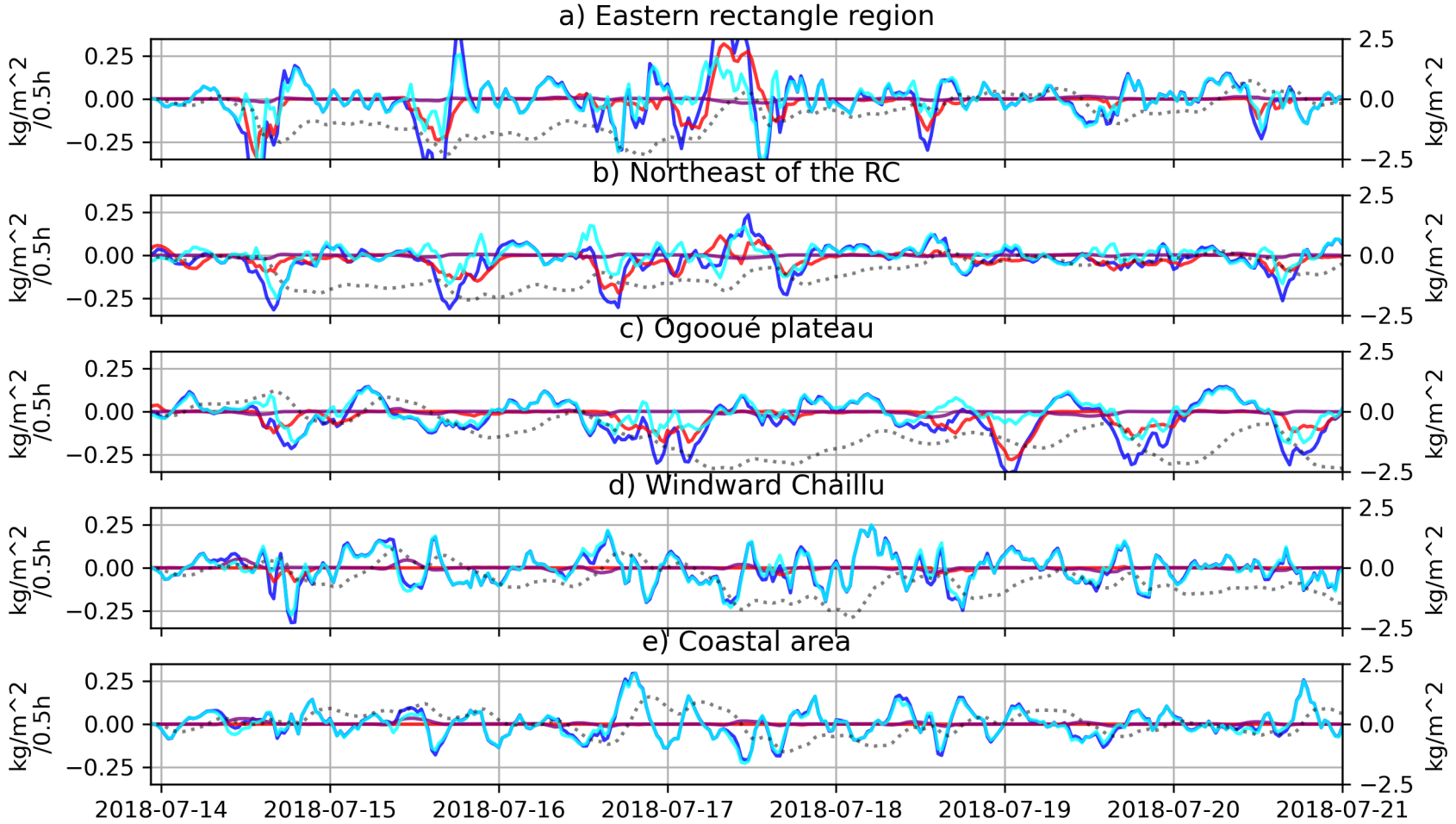

Figure 7.20.: Moisture budget differences between the simulation with parameterised convection and with explicit convection in the eastern edge of the domain, in the Northeast of the RC, over the Ogooué plateau, along the windward side of the Chaillu mountains, and the coastal regions in Gabon. Represented are moisture convergence differences (blue), precipitation differences (red), moisture surface flux differences (purple), and total vertically integrated moisture change (cyan). Dotted is the absolute vertically integrated moisture difference between the two different simulations.

The paragraph describes the moisture budget of four distinct regions, by comparing simulations incorporating explicit and parameterised convection (see Fig 7.20). It was found that simulations using explicit convection transport more moisture from the East to the West and generate more precipitation that do not offset the convergence difference completely. Moisture convergence over the Ogooué and Batéké plateau takes place in the afternoon (see Fig 7.20b). In the coastal region, there is no discernible difference, with moisture change following the convergence curve and surface moisture flux playing a more significant role, possibly due to differences in LLCC (see Fig 7.20d).

In the easternmost region of the domain, we have examined a rectangular section stretching from 17°E to 18.5°E and from 2°S to 1°N to quantify the moisture flow across the border. We aim to highlight the contrast in moisture levels at the start of the flow (see Fig. 7.21). Moisture convergence was evaluated using two approaches in this region: firstly, based on the budget (depicted by the solid line) and secondly, using the humidity velocity on pressure levels (represented by the dashed line). The discrepancies between the two methods of computing moisture convergence arise due to the numerical assumptions made at pressure levels, which cannot account for all model levels. Additionally, the velocity and humidity at the boundaries are captured only as snapshots at half-hour intervals, without consideration for fluctuations in between (see Fig. 7.21a).

On the afternoon of the 14th July, the explicit run shows stronger moisture convergence than the hybrid and parameterised simulations (see Fig. 7.21a). Earlier, before the first convection happens, the curves are similar. Such stronger convection is seen every afternoon. The hybrid convection simulation nearly matches the explicit run's moisture convergence from the afternoon 16th July. Except on the morning of the 17th, the precipitation is heavier in the explicit simulations. The simulation with explicit convection shows higher absolute humidity (see Fig. 7.21e) from the afternoon of the first day of the simulation. The moisture change follows the convergence line, except during precipitation events (see Fig. 7.21a). The moisture surface flux difference between the simulations has only neglectable impact in the far East of the domain.

At the edge of the domain, there are disparities in the moisture budget even though the simulations were intended to be uniform since they both hinge on the equivalent simulation on a broader grid with convection that is parameterised. Consequently, it is crucial to observe what unfolded on the boundary of this small domain in the eastern region. Subsequently, the vertically dispersed moisture transport horizontally will be examined in the subsequent section.

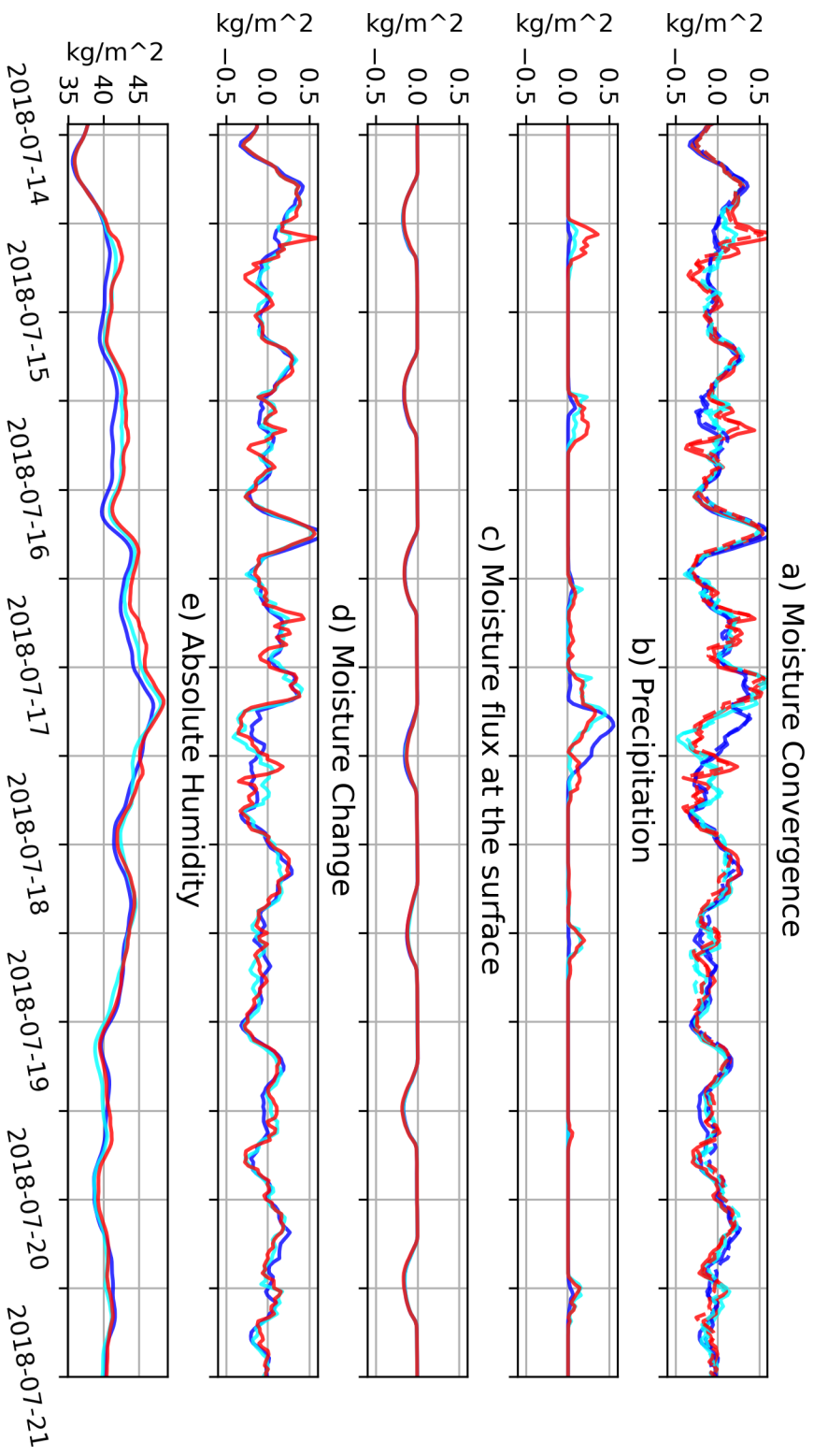

Figure 7.21.: Moisture budget in the rectangle in the very East of the domain (17°E-18.5°E, 2°S-1°N). With the moisture budget as the moisture convergence (a), precipitation (b), moisture flux at the surface (c), total moisture change (d), and the vertically integrated absolute moisture (e).

7.4.9. Profiles of terms of the humidity budget

In this section, we revisit the far eastern area at the boundary of the domain. Below 1700 m.a.s.l, moisture flux is directed towards the East along the eastern and western borders at 1000 UTC, as demonstrated in Fig. 7.22. Additionally, the humidity flux at the eastern border below 1700 m.a.s.l is marginally higher in both explicit and hybrid simulations. Above this altitude, the flux is reversed, and in the lower mid-troposphere, it is slightly higher in the explicit simulations. At the southern border, the flow into the area of interest is weaker below 3700 m.a.s.l. and above it. There is no evident distinction at the southern border. On the northern edge, the parameterised simulation exhibits a slight southward transport of up to 1300 m.a.s.l., whereas it merely transports up to 1050 m.a.s.l. in the simulation solely with explicit convection. Above, there is a strong northwards moisture flux without any big differences between the three different simulations.

At 2200 UTC the differences between the simulation settings are larger (see Fig. 7.23). A noticeably greater moisture flux out of the domain is visible below 1500 m.a.s.l. in the explicit simulation at the East border, while above it, the flux is stronger up to 3800 m.a.s.l. (see Fig. 7.23a). There are minor dissimilarities between parameterised and hybrid convection. The shear moisture flow is comparable on the western border, but more pronounced variations exist between the simulation featuring explicit convection and the other two (see Fig. 7.23b).. The southern border analysis once again demonstrates no apparent differences between the simulations. However, clear discrepancies are observed in the flow along the northern border (see Fig. 7.23d). Specifically, the explicit simulation only displays small lower-level southward moisture flux (see Fig. 7.23c).. The flux reaches up to 700 m.a.s.l., while the parameterised version has its stronger southward flux up to 1000 m.a.s.l.. In the mid-levels, the flow is also weaker in the explicit simulations (see Fig. 7.23d). At 2200 UTC, a smaller amount of moisture is conveyed over the area of interest compared to the simulations with parameterised and hybrid convection.

This comparison demonstrates the variations in humidity treatment across the three simulations. Humidity levels appear to be somewhat higher at all levels along the eastern border. Moisture is brought upwards by the convection parameterisation, thus reducing humidity transportation within the boundary layer. Conversely, more moisture is transported towards the East in explicit simulations compared to hybrid and parameterised simulations in the mid-levels. Between the eastern edge of the domain output and the beginning of the nesting of the domain in parameterised, hybrid, and explicit convection, moisture is lost in the parameterised and hybrid convection simulation. Convection is

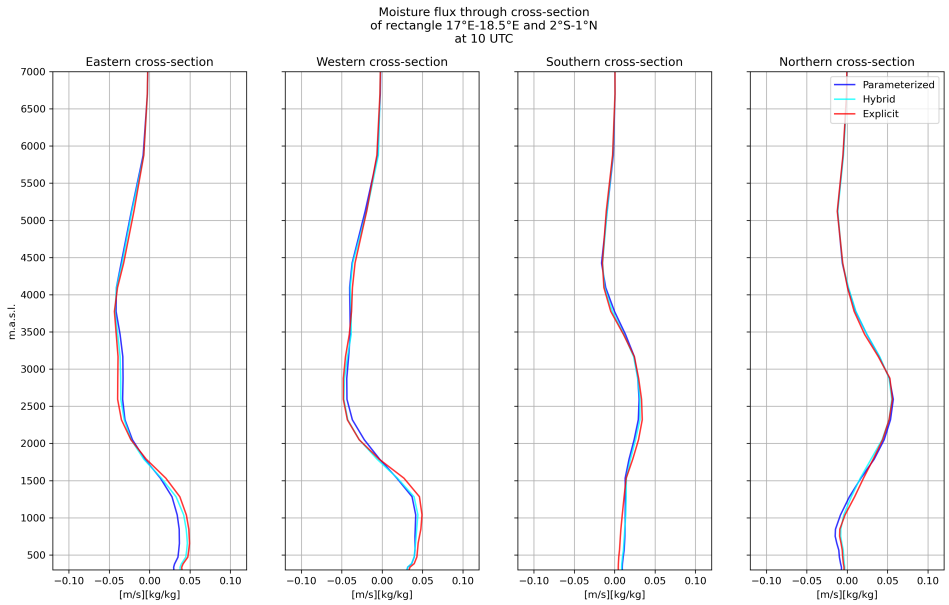

Figure 7.22.: Moisture flux into and out off rectangle (17°E-18.5°E, 2°S-1°N) at 1000 UTC, with explicit convection (red), hybrid convection (cyan), and parameterised convection (blue).

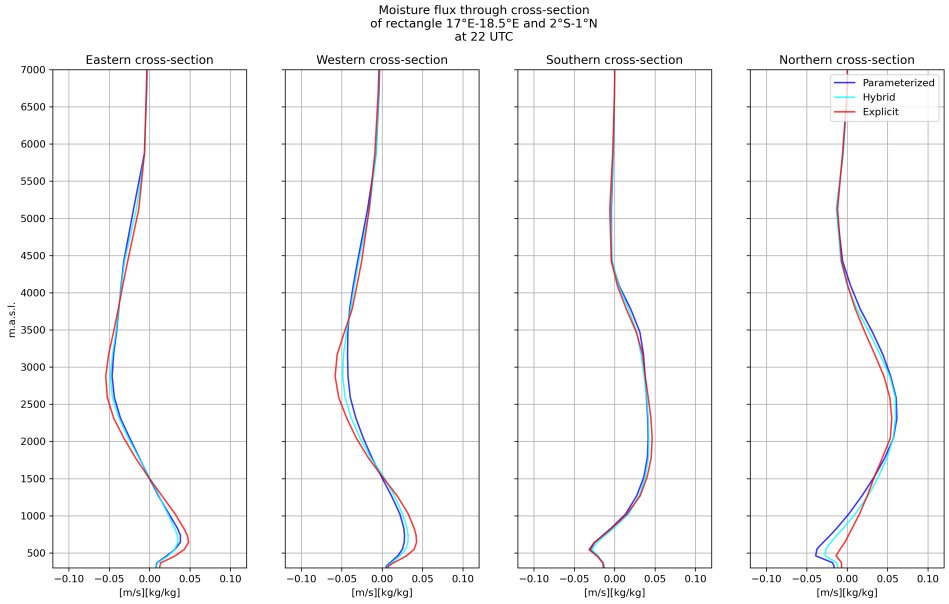

Figure 7.23.: Moisture flux into and out off rectangle (17°E-18.5°E, 2°S-1°N) at 2200 UTC, with explicit convection (red), hybrid convection (cyan), and parameterised convection (blue).

parameterised in the outer nest. Therefore, if the convection is still parameterised, an ongoing precipitating air parcel in the outer domain may continue to precipitate upon entering the inner finer domain. This would not occur if the convection parameterisation is disabled, and the air parcel has to undergo convection without the assistance of the parameterisation scheme. This could clarify the variations in moisture content across the domain.

7.4.10. Relative humidity tendencies

The analysis of humidity tendency at the highest point of the Chaillu mountains is presented in Fig. 7.24. The left-hand side illustrates the contribution of specific humidity to the enhancement or reduction of relative humidity, while the right-hand side displays the impact of the temperature on the enhancement and reduction of relative humidity. It is evident that the variations in specific humidity levels have a significant impact on both simulations, as depicted in Figs. 7.24a, b, c & d. The nocturnal and pre-dawn periods present challenges for distinguishing various patterns due to noise. Around 0400 UTC, the troposphere is more stable than earlier in the night. From 1000 UTC, a first triggering of convection is visible in both the explicit and parameterised versions. In the parameterised version, the trigger is around 1000 UTC on 15 July at about 2200 m.a.s.l. and the RH starts to increase slightly. Conversely, the temperature-trigger appears earlier and at a lower altitude in the atmosphere. The contribution of specific humidity may arise later due to the convergence setting in at higher altitudes, yet its intensity exceeds that of the temperature trigger. In the explicit simulation, convection transpires later than in the parameterised scenario, albeit with greater intensity. The contributions of specific humidity and temperature display similarities to the parameterised simulation.

The simulation employing parameterised convection initiates moisture transport earlier than the one without. Comparable behaviour was already demonstrated in the humidity separation section. The subsequent intensified convection could be attributed to higher humidity in this simulation, as previously mentioned. A later convection trigger combined with a greater potential arising from the increased humidity accounts for the additional and more vigorous convection.

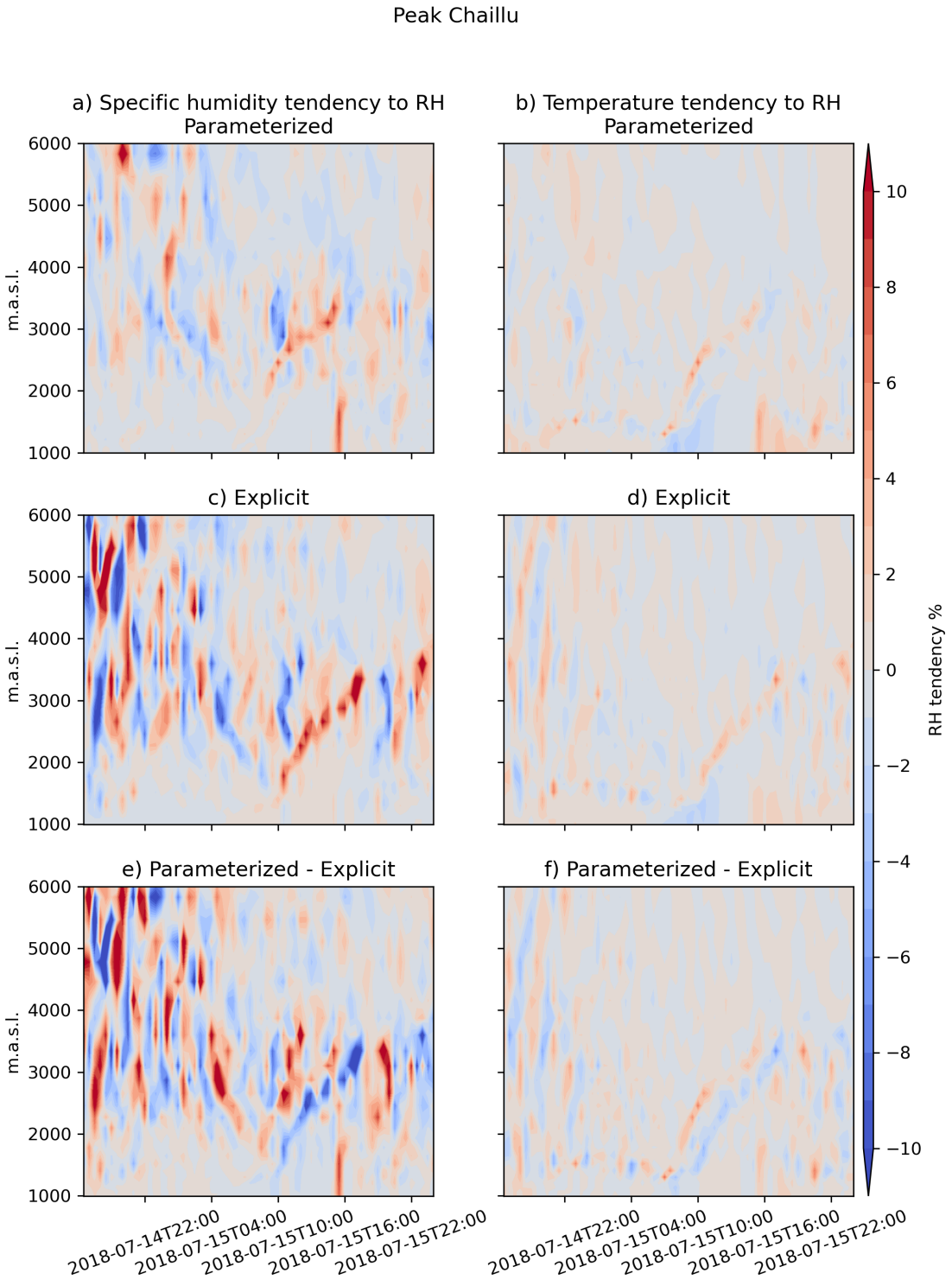

Figure 7.24.: Change of relative humidity based on temperature (right) or specific humidity (left) for the parameterized simulation (a & b), the explicit simulation (c & d) and the difference between them (e & f).

7.4.11. Froude number differences between model experiments

The Froude number, as described in the methods section, measures the passage of an air parcel over or around a mountain range. Figure 7.25 shows the Froude number for both the simulation with explicit convection only and the simulation with parameterised convection. The Froude number is higher on the windward side of the Chaillu mountains in the morning for the explicit version compared to the parameterised version. The contrast is not as significant as one might anticipate from stability variations in other factors.

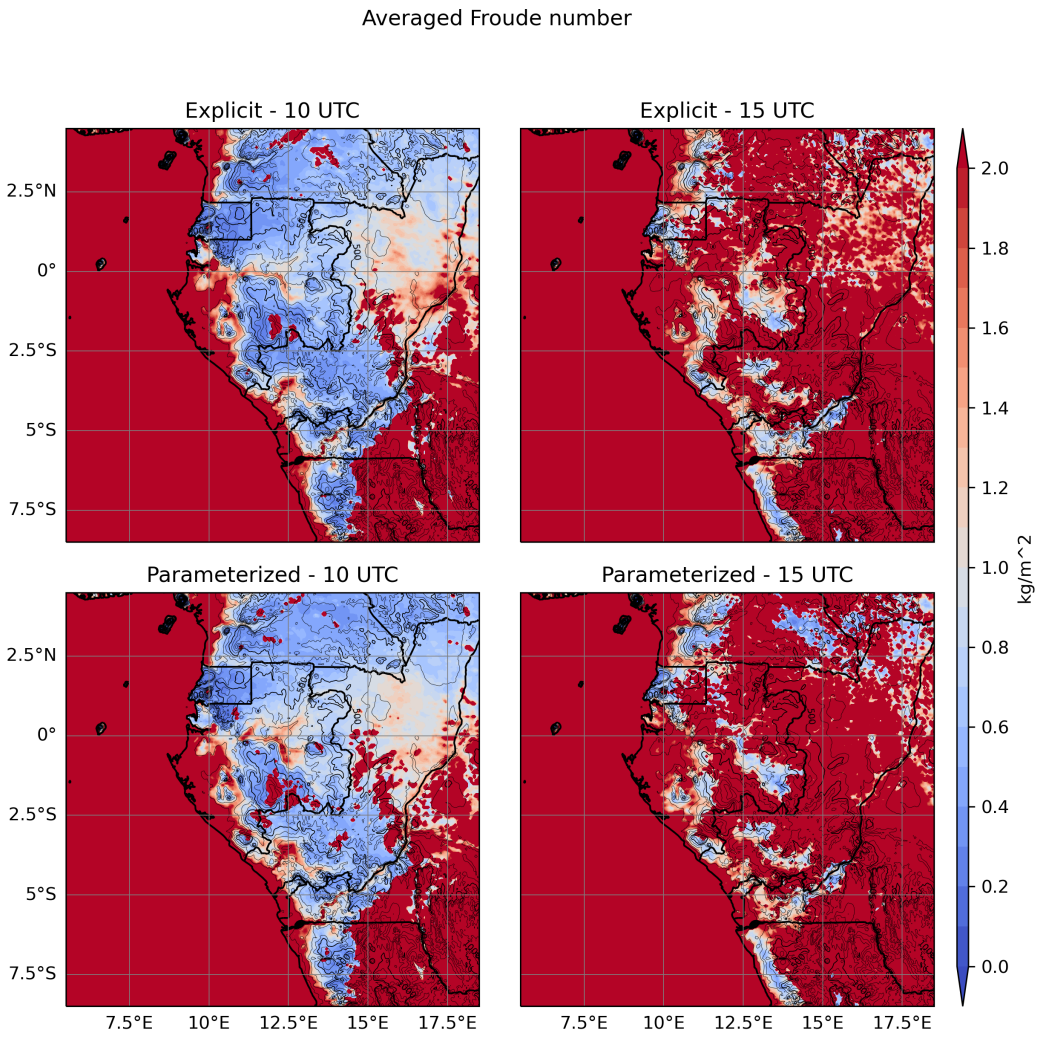

Figure 7.25.: Froude number at 1000 UTC (left) and 1500 UTC (right) averaged over the period of the case study. Upper panels are with explicit convection only and lower panels are with convection parameterisation.

One reason for this could be a lower wind velocity in the explicit version, which is not shown here. Along the ridge, the parameterised model prefers a wider range to surpass. A boundary layer that extends higher might comprise faster wind speeds at elevated altitudes, thereby supplying more momentum to overcome the crest. At 2200 UTC, the majority of the Ogooué valley and plateau region indicates a preference for bypassing obstacles in both scenarios. The Chaillu mountains, in both simulations, favour bypassing the range. In the northeast of Gabon and the RC, the Froude number is slightly lower in the explicit simulation. This may indicate weaker wind flow in the explicit runs, but it cannot be further addressed at this time. On the Batéké plateau, the parameterised version with a higher Froude number favours more bypassing compared to the explicit runs.

To summarise, the simulations exhibit minimal variations in the Froude number. The parameterised simulation slightly favours an overpass in some regions, but the discrepancies are insignificant. The most prominent disparity is the variation between morning and afternoon, which follows a typical diurnal cycle.

7.5. Summary of the case study

The chapter uncovered several disparities in precipitation, humidity, temperature and stability among the three experiments. Specifically, the humidity was higher in the explicit simulations, which can be linked to atmospheric precipitation in the parameterised version in the very East in the transition from the coarser nest to the finest nest. However, this alone cannot account for all the dissimilarities, as shallow convection from the parameterisation scheme also generates a humidity separation. The lower troposphere in the parameterised simulations is comparatively drier than the explicit simulations. But, it is wetter at approximately 2000 m.a.g.l. in the parameterised simulations.

The increased amount of moisture in the explicit simulation results in stronger convection. The explicit simulation shows also a higher amount of low-level clouds. Additionally, a significant finding indicates that moisture is transported from the East (Congo Basin) towards the West in the middle troposphere. This research offers a novel paradigm regarding the moisture origin in WEA. It is strongly influenced by eastern moisture fluxes, not solely by the ocean-side atmosphere. The Froude number, a parameter indicating lower atmosphere stability, suggests that the Chaillu mountains are more likely to be bypassed at night, in all simulation scenarios examined. During the day, they are

more likely to be overflown. This finding supports the presence of strong westerly winds at night, which were previously recorded in 1875 (von Danckelmann, 1878).

Part IV.

Summary and Conclusion

8. Conclusion about the genesis and lysis of low-level clouds

During the long dry season from June to September, LLCC in WEA were analysed in this study. On one hand, the observational approach was employed to achieve a comprehensive climatology of low-level clouds for a deeper understanding of cloud formation and dissipation. On the other hand, the modelling approach was utilised to present in greater detail the specific procedures that can contribute to genesis and lysis of low-level clouds. These two approaches have been used to gain a better understanding of low level clouds and their diurnal cycle during the long dry season in WEA.

8.1. Low-level cloud cover from the observer's perspective

Various observation methods were utilized for the analysis of these LLCC, consisting low-level cloud fraction and genera of synoptic weather observations collected from eighty-five weather stations in WEA (Aellig et al., 2022). These observations are based on four different databases, namely EECRA, ISD, MIDAS, and AMMA. To achieve a uniform representation of the diurnal cycle across time and space, retrievals from the geostationary MSG satellites were used. The cloud fraction of the Geoprof product, derived from data obtained from the polar orbiting satellites CloudSat and CALIPSO in the A-train, was also employed to gain knowledge about the vertical distribution of clouds twice a day. These techniques were employed to examine the cloud distribution profile and address the research questions presented in chapter 3. The diurnal cycle of low-level clouds and their regional variations are the primary subjects of the first research questions.

- **RQ1a:** What are the factors contributing to cloud formation from different observational perspectives in western Equatorial Africa during the long dry season between June and September?

  A1a: Cloud formation takes place at night, when temperatures drop and the saturation capacity of the air decreases. It is apparent from all perspectives. Although the geostationary perspective illustrates a complete diurnal cycle, the Geoprof product is unable to do so. However, the Geoprof product indicates that clouds reach higher altitudes at noon compared to midnight, a perspective that is not visible from the geostationary viewpoint. From the station's perspective, a distinct difference in the diurnal cycle can be seen. Cloud formation typically occurs earlier in the night along the coastline, whereas over the Batéké plateau, cloud formation tends to occur later at night.

- **RQ1b:** What is the low-level cloud diurnal cycle in western Equatorial Africa during the long dry season between June and September?

  A1b: The diurnal variation in cloud cover differs across regions. Low-level cloud cover has a minimal amplitude along the windward side, but it is highest over the plateau and the Northeast of the RC. The low amplitude is caused by cloud accumulation and uplift, resulting in continuous cloud formation along the windward side of the Chaillu mountains throughout the day and night. Low-level clouds over the coast are much more common in the morning, while over the plateau and the Northeast of the RC, clouds tend to have their maximum extent around noon. A possible explanation for the high amplitude could be a slight Foehn effect (Dommo et al., 2018). Distinct phases as in SWA are not observed (Lohou et al., 2020). Finding a comprehensive cloud formation concept in such a diverse region proves to be a challenging task. However, cloud dissipation is an inevitable feature of the day, and low-level cloud formation occurs at night, as expected from previous research (Dommo et al., 2018).

- **RQ1c:** Do we expect different climatologies from different observational perspectives?

  A1c: The dissolution of the clouds usually takes place through a transition from stratiform clouds to cumuliform clouds, induced by daytime turbulence and mixing, what is observable only from cloud types in the station dataset (Aellig et al., 2022, Champagne et al., 2023). The Geoprof data reveals that the landfall of air shows a stronger vertical distribution of low-level clouds at noon and at midnight, which cannot be observed from geostationary satellite retrievals. Based on the satellite and station data available, there is currently no conclusive evidence of a Foehn effect as proposed by Dommo et al. (2018). Nevertheless, it cannot be denied for the time being. However, it is possible that cloud dissipation is predominantly influenced by daytime mixing of the boundary layer, as indicated by the variation in cloud types observed during the afternoon.

- **RQ1:** How can a comprehensive climatology of low-level clouds be developed?

  A1: From the various observation data collected through both station-based and space-borne methods, a comprehensive view of low-level clouds in WEA during extended dry periods has been established. The study identifies the factors contributing to the formation and subsequent dissolution of these clouds.

Furthermore, an understanding of cloud formation can be gained from the vertical distribution of clouds. Over the ocean, the cloud layer is very thin and close to the sea surface. However, over land, the clouds begin to disperse vertically. The satellite tracks of CloudSat and CALIOP are located in the southern section of the region of interest, close to the transect of the 925 hPa flow. From this perspective, it appears that when clouds pass from the sea to the ocean, they encounter turbulence caused by rougher terrain or stronger air turbulence over land. Low-level clouds are shown from different perspectives and in different regions during the long dry season in WEA.

8.2. Low-level cloud cover in numerical weather prediction models

To gain understanding into low-level clouds in western Equatorial Africa, an Numerical Weather Prediction model was utilized in a case study conducted from 14th to 21st July 2018. The study examined numerous parameters, including differences between cases of a parameterised version, a hybrid version that exclusively parameterised shallow convection and a simulation comprising only explicit convection.

The different approaches show the moisture, while investigating the transport of moisture and identifying differences between the test simulation. The analysis examined specific humidity, relative humidity, and condensation. On the other hand, the lower atmosphere's stability was analysed, which included an examination of the Froude number and the vertical gradients of the potential temperature . The chapter 3's posed questions were satisfactorily answered:

- **RQ2a:** How does the parameterisation of convection impact atmospheric moisture and its role in cloud formation and dissolution?

  A2a: The parameterisation decreases the humidity in western Equatorial Africa, leading to dehydration of the boundary layer and its subsequent height increase. The parameterisation scheme resulted in significant drying at the boundary edges of the innermost domain. On the parent grid, the parameterisation scheme is active, resulting in a constant convective atmosphere entering the innermost nest when parameterisation is also active. If parameterisation is switched off in the innermost nest, convection immediately stops entering the innermost nest at its boundaries. Explicit convection needs some time to spin-up. While air masses are transported westward in the mid-troposphere, the air above WEA exhibits higher water content in the explicit simulation. This results in the primary disparities between the moisture budgets in the modelled regions when employing distinct convection approaches.

- **RQ2b:** What is the effect of shallow convection parameterisation on moisture levels in the model?

  A2b: Shallow convection leads to certain mixing and drying effects in the lower troposphere. It does not have the same impact on humidity as the deep convection parameterisation does. The shallow convection transports moist air from the boundary layer upwards while mixing with dry air from above. This results in a drier boundary layer and a more humid mid-low troposphere, as illustrated in Figs. 7.18 & 7.19. The increased moisture in the boundary layer in the explicit simulation results in a higher potential for strong convective situations. Therefore, in the simulation with only shallow convection parameterised, precipitation is reduced compared to the explicit as the explicit simulations generate convective-driven precipitation. Furthermore, the shallow convection scheme mixes in dry air, resulting in a moisture-deficient boundary layer and fewer clouds forming at night.

- **RQ2c:** Which fluxes, both sensible and latent, are observed on the ground in the context of parameterised, shallow convection or explicit convection only?

  A2c: A distinct diurnal cycle is apparent, with small differences in heat fluxes observed on days with substantial variations in cloud cover. From the perspective of the moisture budget, the most pronounced disparities in moisture content among the various methods pertain to the convergence of moisture into the WEA domain. The differences in specific humidity and temperature do not result in a significant increase in moisture fluxes. The difference in heat flow and latent heat flow between the simulations is negligible. Nevertheless, the surface fluxes are of secondary importance when considering the moisture budget.

- **RQ2:** How do the different approaches concerning convection affect the formation and dissipation of low-level clouds?

  A2: The primary impact on humidity arises from deep convection at the edges of the domain, which can be clearly seen in the moisture budgets. A less humid atmosphere yields a reduction in low-level clouds. The vertical tranport of moisture leads to greater atmospheric stability, albeit resulting in relatively fewer low-level clouds. Moreover, the dry shallow convection mechanism results in a drier boundary layer. The higher precipitation in the explicit simulation is unable to offset the humidity differences.

Low-level cloud cover is more pronounced in explicit simulations. Depending on the region a different picture of cloud formation can be drawn. While on the eastern part of the domain, the absence of moisture advection appears to be the driving factor for the fewer low-level clouds. In contrast, a different regime is present along the coast. The marine air remains unaffected by the convection-driven dry spells overland in the east. The coastal regions experience equally humid maritime air in both the parameterised simulation and the explicit simulation. This permits a delayed dissipation of the low-level clouds in the parameterised version over the coastal area.

The dissolution of clouds over the Batéké plateau, caused by convection, is evident in the station data where Stratocumulus clouds transform into Cumulus clouds. This phenomenon is also observable in the afternoon breakups simulated in the case study. Additionally, the simulation and observations indicate cloud accumulation on the windward side of the Chaillu mountains. This was exceptionally noteworthy within the Transects (see Fig. 7.9). From the simulations, it appears that there is an inhibition of overflow during the night based on the Froude number (see Fig. 7.25). During the daytime, when the atmosphere is less stable, the overflow appears to be dominant.

Moisture and stability are important factors in the region of western Equatorial Africa. This has been demonstrated using moisture profiles and transects. The source and sink of moisture are also discussed in this thesis. Moisture advection in the lower mid-troposphere (2000 - 4000 m.a.s.l., see Figs. 7.22 & 7.23) plays a larger role than initially expected. The conceptual approach of Adler et al. (2019) and Lohou et al. (2020) cannot be applied here because of the ubiquitous moisture input from the east. Therefore, it is not the maritime air that is the dominant driver of humidity, but rather the midlevel moisture advection from the East.

The study also showed the limitations of NWP in the region, which is little explored in terms of atmospheric behaviour and measurements, especially in-situ. The differences between the approaches revealed the potential driver, but could not be finally quantified. This study provides an overview of low level clouds over western Equatorial Africa.

9. Outlook

Low-level clouds continue to be a vital concern in a region that plays an essential role in climate change. Clouds, particularly those in the lower troposphere, have a significant impact on the Earth's energy balance. Since their behaviour is not entirely comprehended, it is possible that weather and climate models may be biased, leading to inaccurate representation of low-level clouds (Vignesh et al., 2020).

A thorough understanding of low-level clouds remains crucial. It might be crucial to develop approaches to better represent them to reduces biases in climate models. Further, it is necessary to conduct NWP model simulations to explore low-level clouds and comprehend the processes that generate and disperse them. Large-Eddy simulation will show the way, when and where do they dissipate in the WEA.

A more extensive examination of the dynamical flow and moisture advection originating from the East is also highly significant. Conducting a study would enable the identification of long-term sources and sinks of moisture in the region. Nevertheless such a study would need a lot of computational effort but might reveal new insights.

Africa is a continent where observation data are scarce. Compared to other regions such as Europe, North America and China, the data sets are small. At least some observations were made long ago, providing some insight into cloud formation and surface wind flow (von Danckelmann, 1878). But to resolve the behaviour of the boundary layer and its influence on the low-level cloud deck, broad and intensive measurements are essential. An observational campaign of the kind once planned for this study is of great importance in resolving the unknown processes that drive the atmosphere in western equatorial Africa.

The precise processes, including water vapour and heat fluxes at the surface, would help to unravel the lower troposphere. Radiosondes and remote sensing instruments would also help to understand the state of the atmosphere. But such fieldwork is a huge commitment and difficult to organise in politically unstable regions. Until now, we have had to rely on monitoring carried out mainly by airports and aerodrome maintainers. They

are obliged to monitor certain atmospheric parameters. However, the scarcity and bias of this data is also a problem.

One hope for a deeper understanding of low-level clouds and their behaviour in the atmosphere is Meteosat Third Generation, launched last year (2022). Compared to Meteosat Second Generation (EUMETSAT, 2004), the new instruments have a higher resolution and measure in finer wavelength bands (Holmlund et al., 2021). This opens up new possibilities for tracking low-level clouds, as was done with Meteosat Second Generation. A new tool, measuring lightning activity, would even allow us to see potential convective systems during the dry season if they are present. There is therefore hope for further progress in understanding low-level clouds over western Equatorial Africa.

A. Appendix

A.1. Supplementary Material

A.1.1. Radiosond observations and modelled vertical Profiles

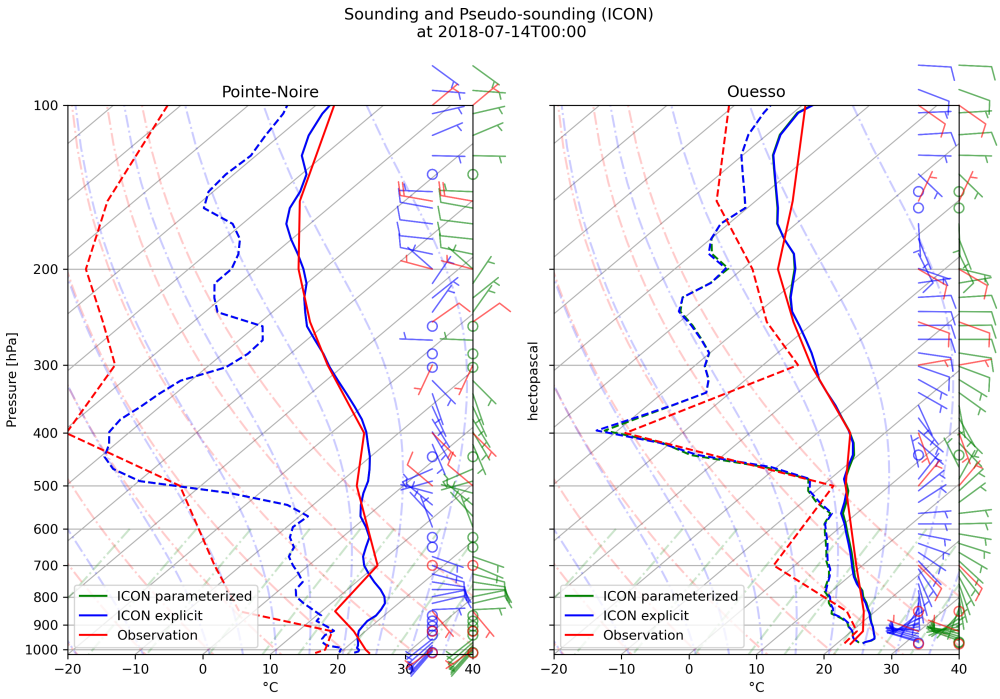

Figure A.1.: Radiosonde observations(red) at noon in Pointe-Noire(left) and Ouesso(right) and the closest vertical profile in the model for the parameterised (green) the explicit (blue) setting at 00 UTC on the 14th July 2018.

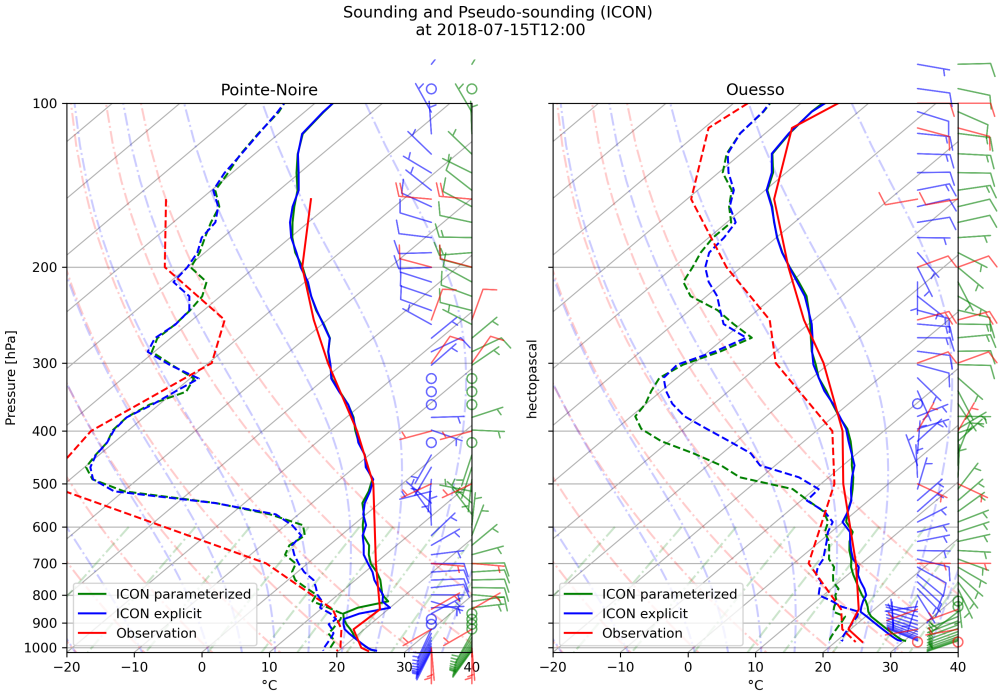

Figure A.2.: Radiosonde observations(red) at noon in Pointe-Noire(left) and Ouesso(right) and the closest vertical profile in the model for the parameterised (green) the explicit (blue) setting at 12 UTC on the 15th July 2018.

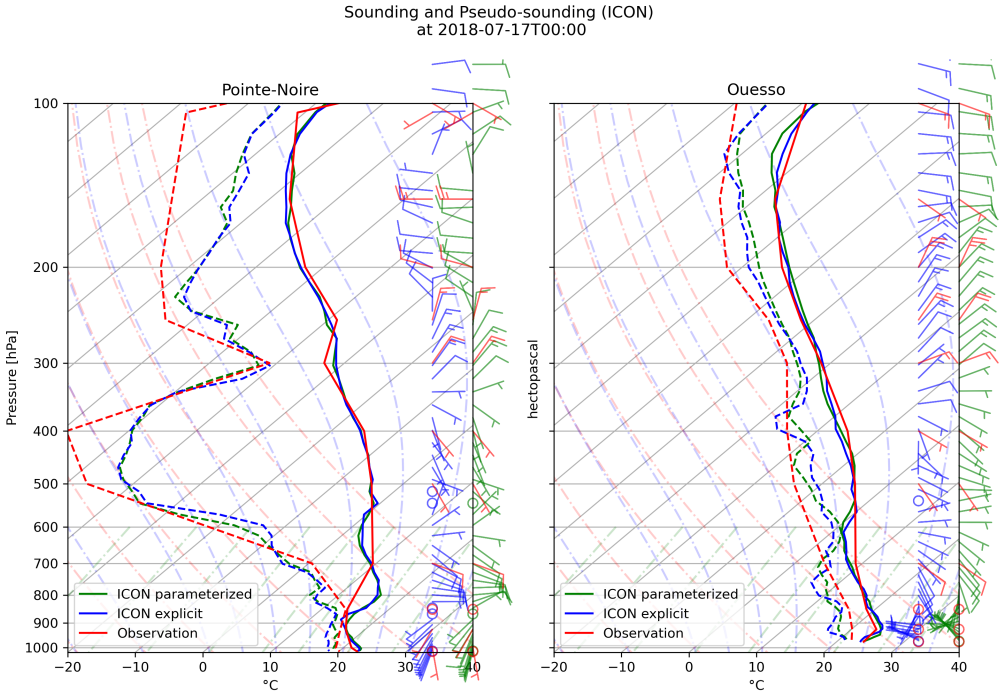

Figure A.3.: Radiosonde observations(red) at noon in Pointe-Noire(left) and Ouesso(right) and the closest vertical profile in the model for the parameterised (green) the explicit (blue) setting at 00 UTC on the 17th July 2018.

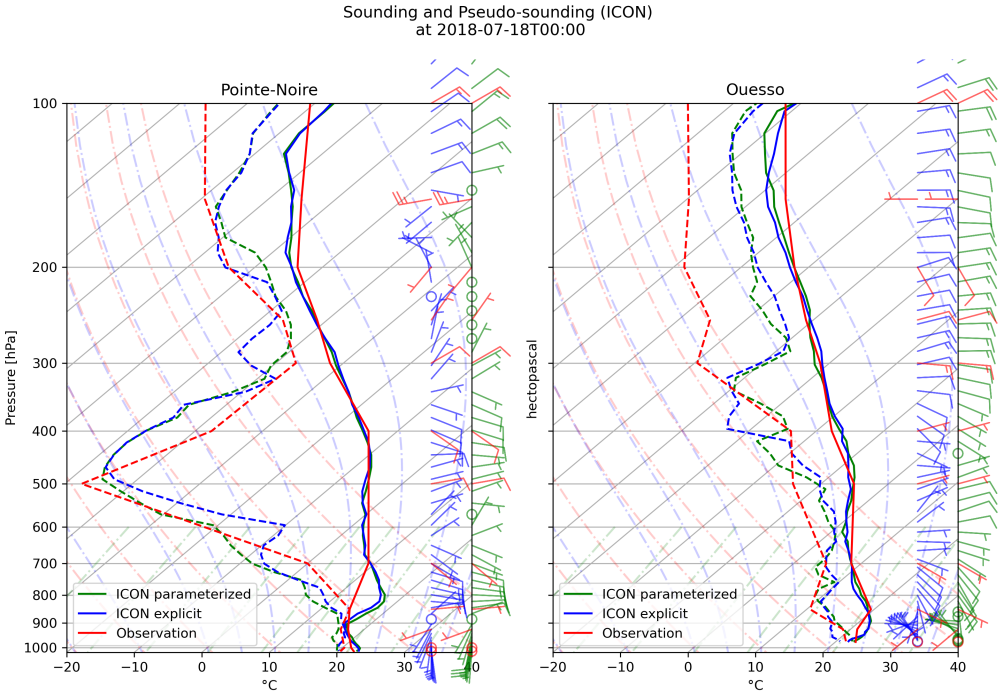

Figure A.4.: Radiosonde observations(red) at noon in Pointe-Noire(left) and Ouesso(right) and the closest vertical profile in the model for the parameterised (green) the explicit (blue) setting at 00 UTC on the 18th July 2018.

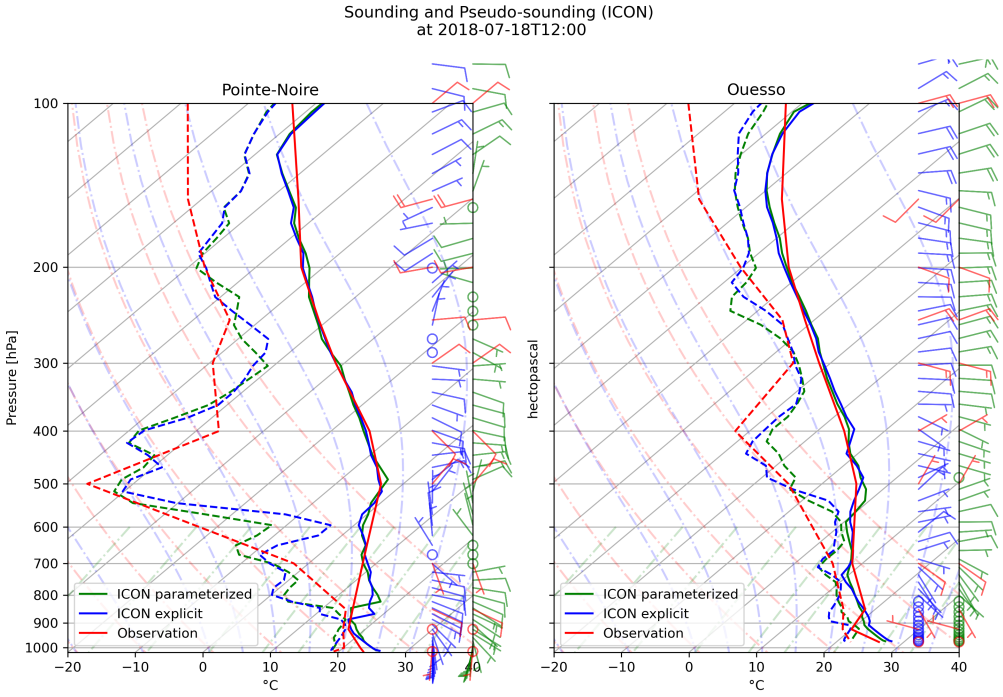

Figure A.5.: Radiosonde observations(red) at noon in Pointe-Noire(left) and Ouesso(right) and the closest vertical profile in the model for the parameterised (green) the explicit (blue) setting at 12 UTC on the 18th July 2018.

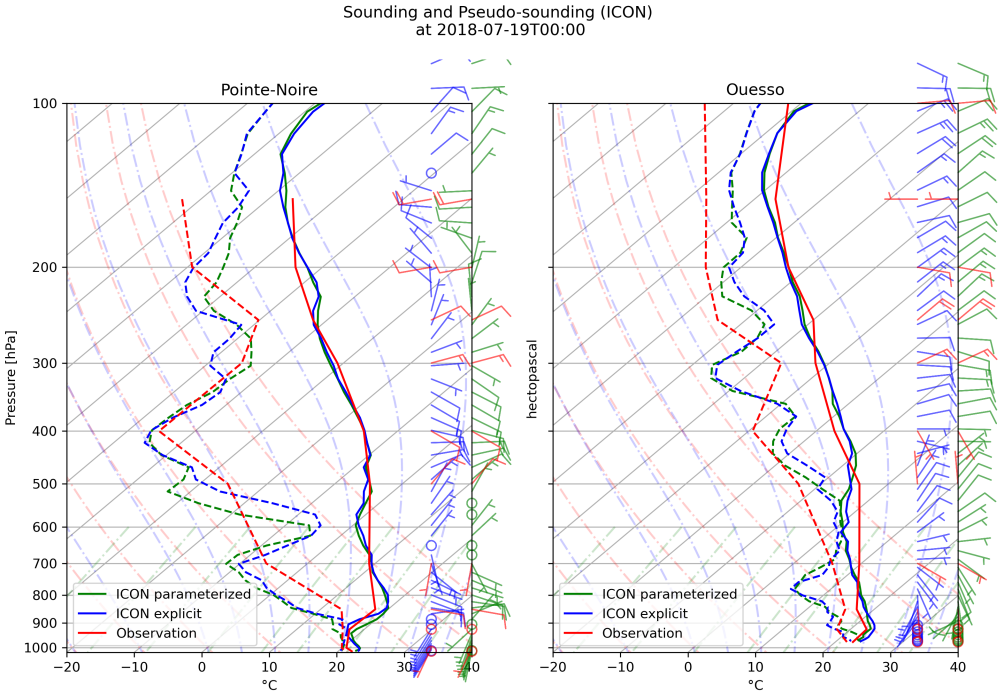

Figure A.6.: Radiosonde observations(red) at noon in Pointe-Noire(left) and Ouesso(right) and the closest vertical profile in the model for the parameterised (green) the explicit (blue) setting at 00 UTC on the 19th July 2018.

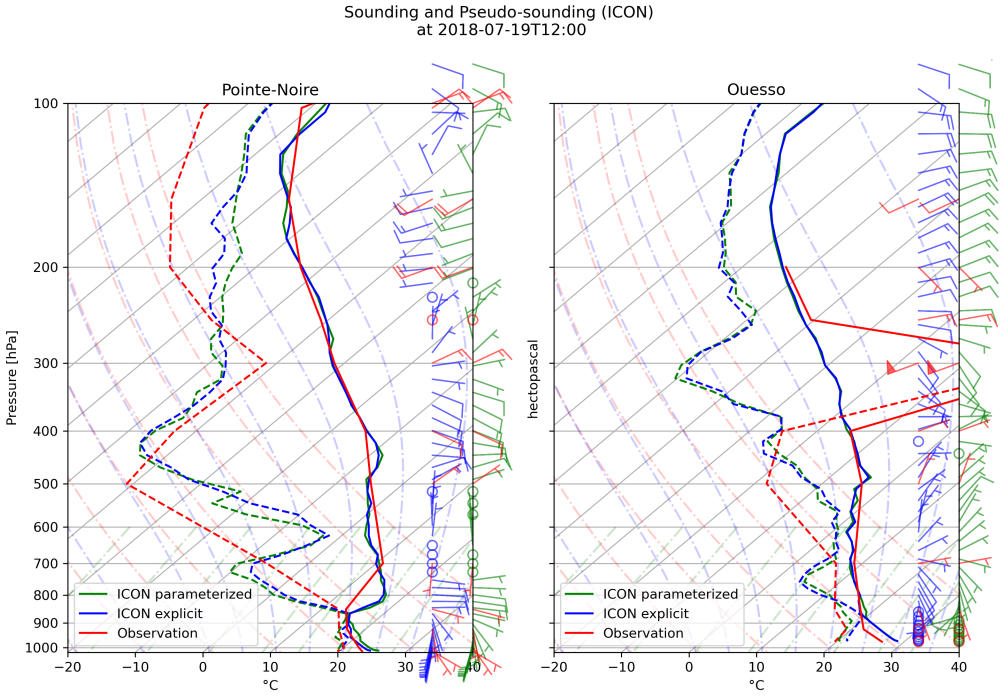

Figure A.7.: Radiosonde observations(red) at noon in Pointe-Noire(left) and Ouesso(right) and the closest vertical profile in the model for the parameterised (green) the explicit (blue) setting at 12 UTC on the 19th July 2018.

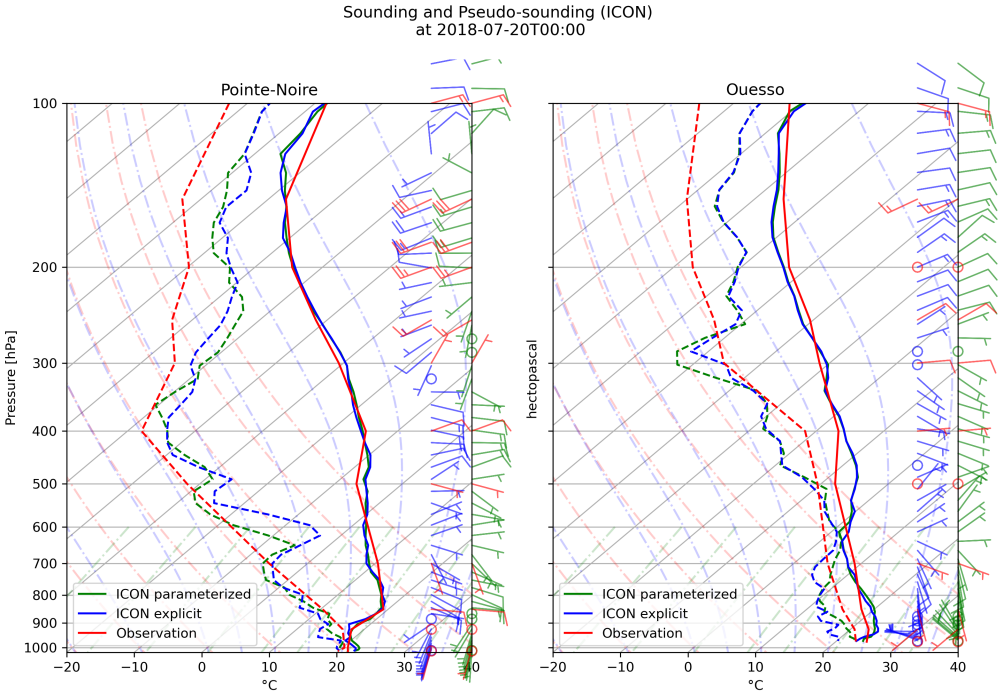

Figure A.8.: Radiosonde observations(red) at noon in Pointe-Noire(left) and Ouesso(right) and the closest vertical profile in the model for the parameterised (green) the explicit (blue) setting at 00 UTC on the 20th July 2018.

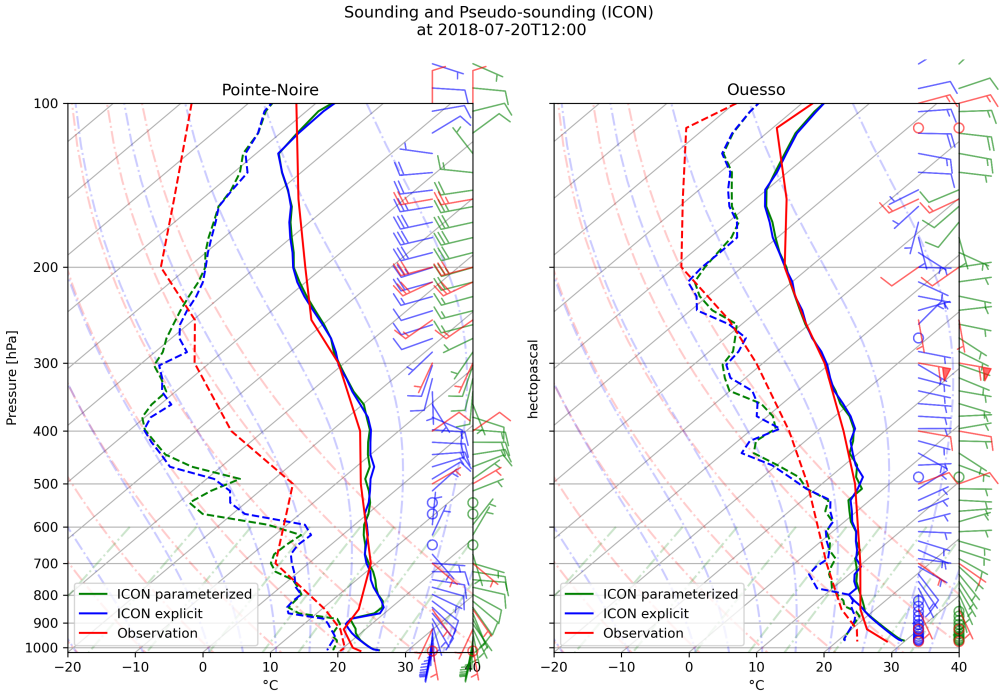

Figure A.9.: Radiosonde observations(red) at noon in Pointe-Noire(left) and Ouesso(right) and the closest vertical profile in the model for the parameterised (green) the explicit (blue) setting at 12 UTC on the 20th July 2018.

A.2. Profiles over time at points of interest

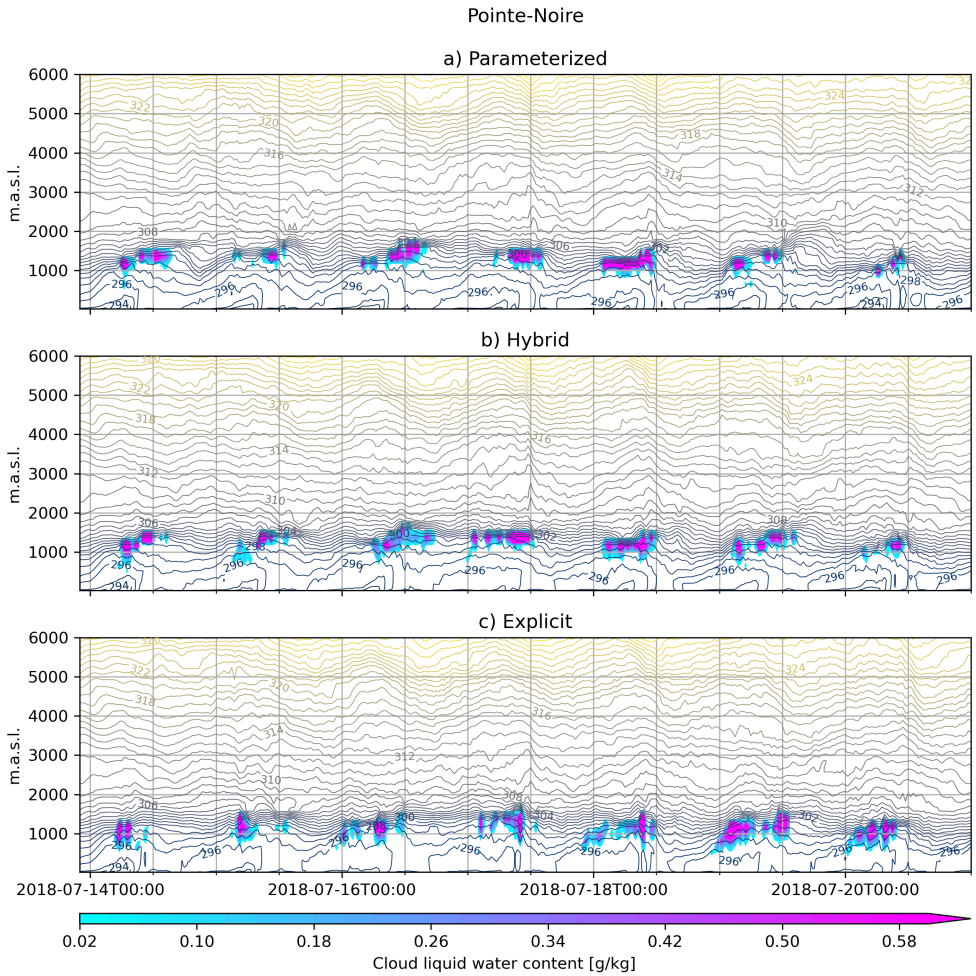

Figure A.10.: Vertical profiles of the diurnal cycle at Pointe-Noire of cloud liquid water content [g/kg] mean and potential temperature [K] mean for the settings: parameterised convection (a), hybrid convection (b), and explicit convection (c).

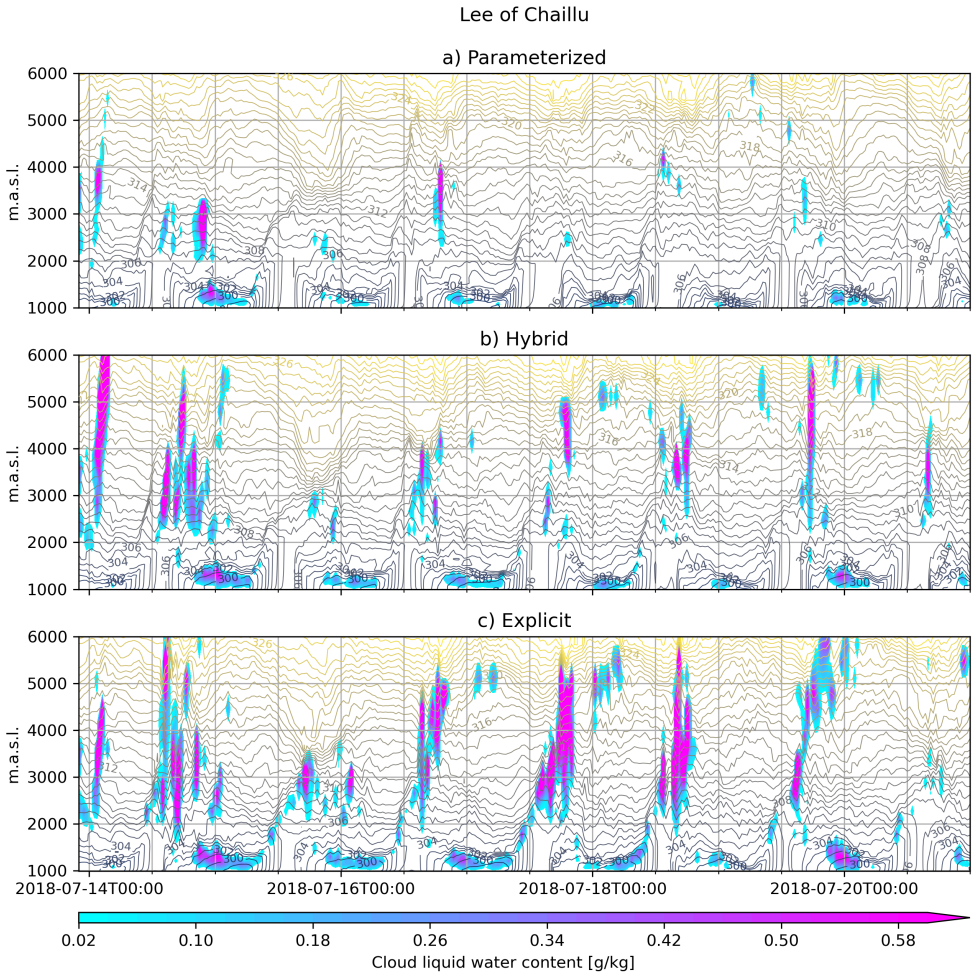

Figure A.11.: Vertical profiles of the diurnal cycle at the peak of the Chaillu mountains of cloud liquid water content [g/kg] mean and potential temperature [K] mean for the settings: parameterised convection (a), hybrid convection (b), and explicit convection (c).

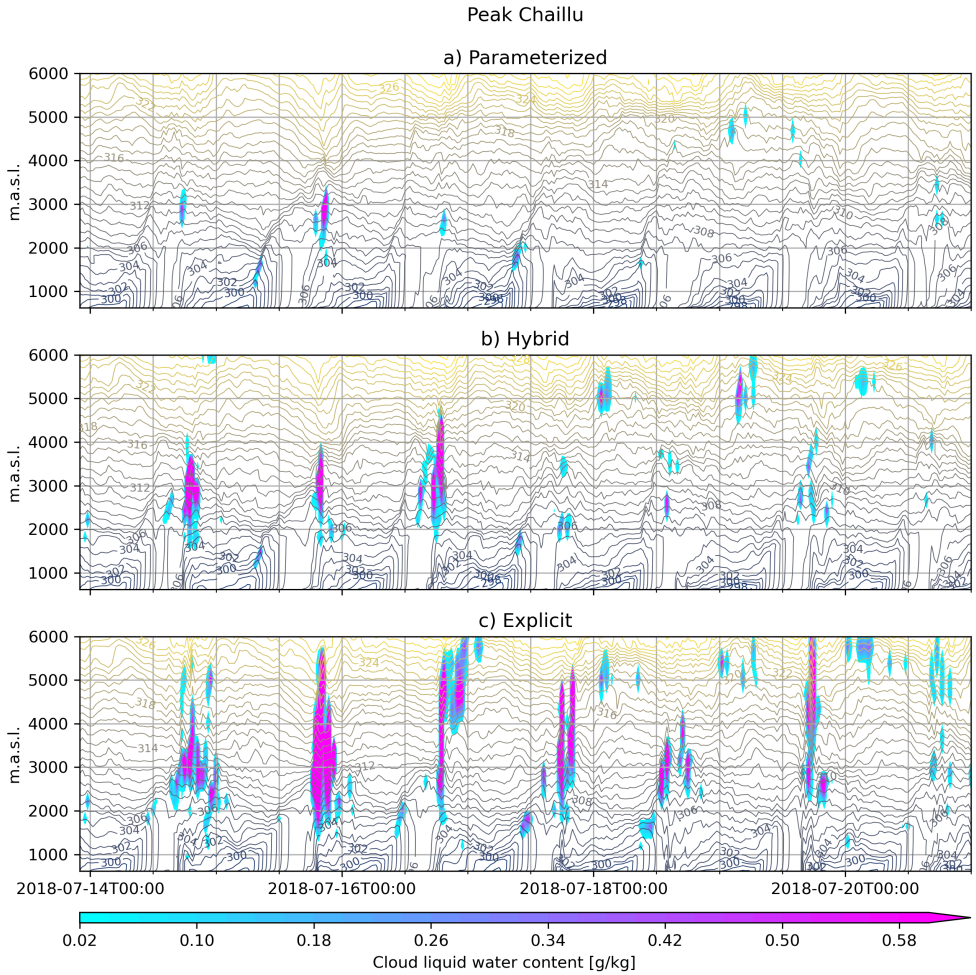

Figure A.12.: Vertical profiles of the diurnal cycle at the leeward side of the Chaillu mountains of cloud liquid water content [g/kg] mean and potential temperature [K] mean for the settings: parameterised convection (a), hybrid convection (b), and explicit convection (c).

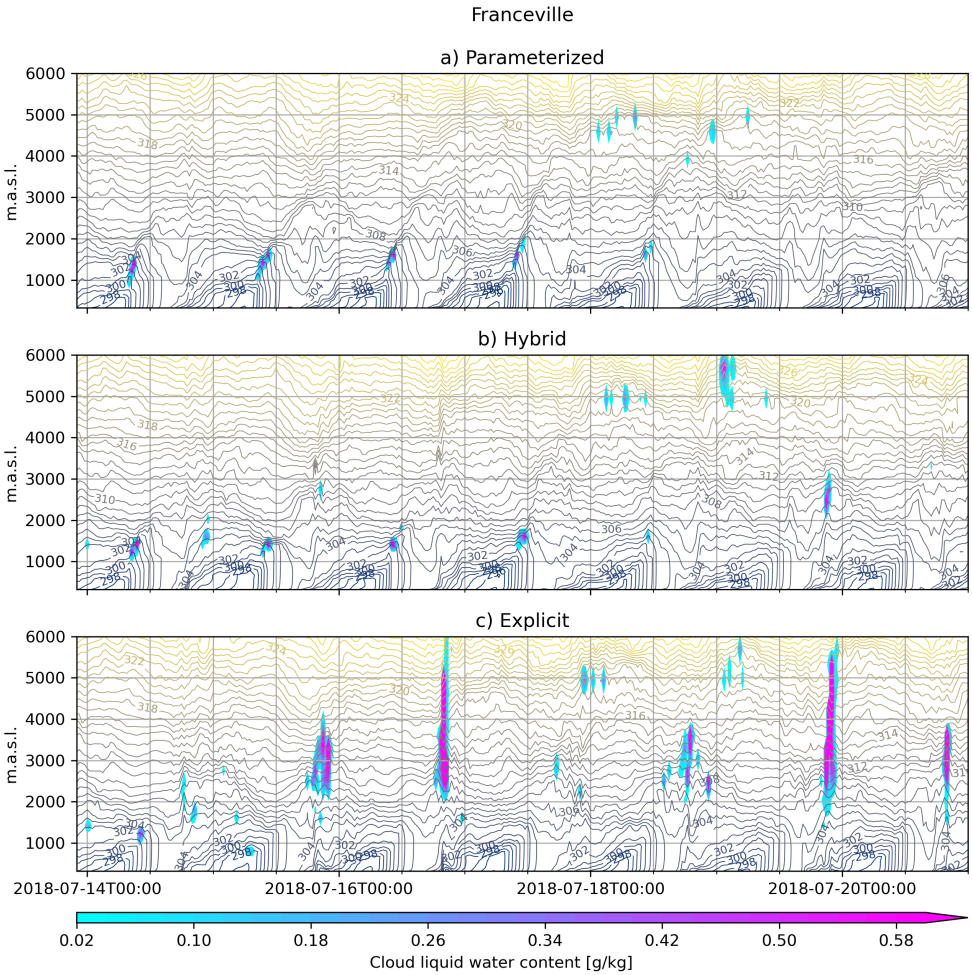

Figure A.13.: Vertical profiles of the diurnal cycle at Franceville M'vengue of cloud liquid water content [g/kg] mean and potential temperature [K] mean for the settings: parameterised convection (a), hybrid convection (b), and explicit convection (c).

B. Acknowledgements

At this point I would like to take a few lines to thank the people who have accompanied and supported me on my doctoral journey. First, of course, I would like to thank Andreas Fink who, as my supervisor, has given me valuable input into my research during our Wednesday afternoon meetings over the past few years. Whether they were short or long, the meetings were always productive and full of new ideas. Thanks also for the constant encouragement, which was very helpful in planning the fieldwork. Unfortunately, the planned campaign in Gabon did not take off, but it was still a very valuable experience. A big thank you also goes to my second supervisor, Peter Knippertz, who gave me a lot of input during our meetings and always had a good guess to explain an unexplained phenomenon. I would also like to thank our French partners, Nathalie Philippon, Pierre Camberlin and Vincent Moron, with whose collaboration we were able to generate a lot of scientific output in our bi-national project DYVALOCCA. Despite the difficult circumstances during the pandemic, to which we all had to adapt at first, the joint project meetings were always productive and fruitful.

Thanks also to Martin Kohler and Simone Scheer for their help in preparing the field campaign. The long days at Campus North to test instruments or to get the supposedly last certificate for the shipment of our instruments for the field campaign were made easier by the good atmosphere at work or during the joint coffee breaks.

Another big thank you goes to Marlon, Lea and Christoph, who were very supportive and became valuable friends during the difficult times of starting in a new city during a pandemic. Also a big thank you to all the other colleagues I had the pleasure of spending time with, giving me scientific input or just having a great time. In particular, a big thank you to Athul and Beth, who were a great help in proofreading my thesis, and to Jannik and Marlon, who were indispensable in helping me obtain data through PAMORE.

I would also like to thank my parents, who made it possible for me to follow the path I have chosen. It was very valuable for me to know that education was very important

to them and that they supported my studies, especially at such a competitive university as ETHZ.

My greatest thanks go to Saija, who has known me since my time in Karlsruhe. She was always supportive and a source of joy during the difficult times of the PhD. The emotional support has been incredibly helpful in this very challenging time and I am glad and happy to have her by my side.

Bibliography

Adler, B., Babić, K., Kalthoff, N., Lohou, F., Lothon, M., Dione, C., Pedruzo-Bagazgoitia, X., & Andersen, H. (2019). Nocturnal low-level clouds in the atmospheric boundary layer over southern west africa: An observation-based analysis of conditions and processes. *Atmospheric Chemistry and Physics*, *19*(1), 663–681.

Adler, B., Kalthoff, N., & Gantner, L. (2017). Nocturnal low-level clouds over southern west africa analysed using high-resolution simulations. *Atmospheric Chemistry and Physics*, *17*(2), 899–910.

Aellig, R., Moron, V., Camberlin, P., Champagne, O., Philippon, N., Fink, A. H., & Knippertz, P. (2022). Cloud observing data of 85 stations in western central africa.

Albrecht, R. I., Goodman, S. J., Buechler, D. E., Blakeslee, R. J., & Christian, H. J. (2016). Where are the lightning hotspots on earth? *Bulletin of the American Meteorological Society*, *97*(11), 2051–2068.

Alexandersson, H., & Moberg, A. (1997). Homogenization of swedish temperature data. part i: Homogeneity test for linear trends. *Int. J. Climatol.*, *17*, 25–34.

AMMA. (2002). *African monsoon multidisciplinary analysis - data base*. Météo France.

Avgoustoglou, E., Voudouri, A., Carmona, I., Bucchignani, E., Levi, Y., & Bettems, J. (2020). A methodology towards the hierarchy of cosmo parameter calibration tests via the domain sensitivity over the mediterranean area. *COSMO Techical Report*, *42*.

Balas, N., Nicholson, S., & Klotter, D. (2007). The relationship of rainfall variability in west central africa to sea-surface temperature fluctuations. *International Journal of Climatology: A Journal of the Royal Meteorological Society*, *27*(10), 1335–1349.

Barker, H. W., Stephens, G., Partain, P., Bergman, J., Bonnel, B., Campana, K., Clothiaux, E., Clough, S., Cusack, S., Delamere, J., et al. (2003). Assessing 1d atmospheric solar radiative transfer models: Interpretation and handling of unresolved clouds. *Journal of Climate*, *16*(16), 2676–2699.

Bayon, G., Schefuß, E., Dupont, L., Borges, A. V., Dennielou, B., Lambert, T., Mollenhauer, G., Monin, L., Ponzevera, E., Skonieczny, C., & André, L. (2019). The roles of climate

and human land-use in the late holocene rainforest crisis of central africa. *Earth and Planetary Science Letters*, *505*, 30–41. https://doi.org/https://doi.org/10.1016/j.epsl.2018.10.016

Bechtold, P., Sandu, I., Klocke, D., Semane, N., Ahlgrimm, M., Beljaars, A., Forbes, R., & Rodwell, M. (2014). The role of shallow convection in ecmwfs integrated forecasting system. http://www.ecmwf.int/publications/

Bechtold, P., Köhler, M., Jung, T., Doblas-Reyes, F., Leutbecher, M., Rodwell, M. J., Vitart, F., & Balsamo, G. (2008). Advances in simulating atmospheric variability with the ecmwf model: From synoptic to decadal time-scales. *Quarterly Journal of the Royal Meteorological Society*, *134*, 1337–1351. https://doi.org/10.1002/qj.289

Bigot, S., Philippon, N., Gond, V., Moron, V., Pokam, W., Bayol, N., Boyemba, F., Kahindo, B., Samba, G., Ngomanda, A., et al. (2016). État actuel des réseaux de mesures éco-climatiques en afrique centrale: Les ambitions du projet de recherche international forgreene., 101–106.

Bjerknes, J. (1969). Atmospheric teleconnections from the equatorial pacific. *Monthly weather review*, *97*(3), 163–172.

Bony, S., Stevens, B., Frierson, D. M., Jakob, C., Kageyama, M., Pincus, R., Shepherd, T. G., Sherwood, S. C., Siebesma, A. P., Sobel, A. H., et al. (2015). Clouds, circulation and climate sensitivity. *Nature Geoscience*, *8*(4), 261–268.

Bretherton, C. (1997). Entrainment, detrainment and mixing in atmospheric convection. In *The physics and parameterization of moist atmospheric convection* (pp. 211–230). Springer.

Brönnimann, S. (2009). Start of the classic papers series. *Meteorologische Zeitschrift*, *18*(3), 339–340. https://doi.org/10.1127/0941-2948/2009/0385

Cermak, J. (2012). Low clouds and fog along the south-western african coast—satellite-based retrieval and spatial patterns. *Atmospheric Research*, *116*, 15–21.

Champagne, O., Aellig, R., Fink, A. H., Philippon, N., Camberlin, P., Moron, V., Knippertz, P., Seze, G., & van der Linden, R. (2023). Climatology of low-level clouds over western equatorial africa based on ground observations and satellites. *Journal of Climate*, *36*(13), 4289–4306.

Cheng, A., & Xu, K.-M. (2015). Improved low-cloud simulation from the community atmosphere model with an advanced third-order turbulence closure. *Journal of Climate*, *28*(14), 5737–5762.

Christian, H. J., Blakeslee, R. J., Boccippio, D. J., Boeck, W. L., Buechler, D. E., Driscoll, K. T., Goodman, S. J., Hall, J. M., Koshak, W. J., Mach, D. M., et al. (2003). Global frequency and distribution of lightning as observed from space by the optical transient detector. *Journal of Geophysical Research: Atmospheres*, *108*(D1), ACL–4.

Cook, K. H., & Vizy, E. K. (2016). The congo basin walker circulation: Dynamics and connections to precipitation. *Climate Dynamics*, *47*, 697–717.

Dee, D. P., Uppala, S. M., Simmons, A. J., Berrisford, P., Poli, P., Kobayashi, S., Andrae, U., Balmaseda, M., Balsamo, G., Bauer, d. P., et al. (2011). The era-interim reanalysis: Configuration and performance of the data assimilation system. *Quarterly Journal of the royal meteorological society*, *137*(656), 553–597.

Dione, C., Lohou, F., Lothon, M., Adler, B., Babić, K., Kalthoff, N., Pedruzo-Bagazgoitia, X., Bezombes, Y., & Gabella, O. (2018). Low level cloud and dynamical features within the southern west african monsoon. *Atmos. Chem. Phys. Discuss., https://doi.org/10.5194/acp-2018-1149, in review*.

Dommo, A., Philippon, N., Vondou, D. A., Sèze, G., & Eastman, R. (2018). The june–september low cloud cover in western central africa: Mean spatial distribution and diurnal evolution, and associated atmospheric dynamics. *Journal of Climate*, *31*(23), 9585–9603.

Doms, G., Förstner, J., Heise, E., Herzog, H., Mironov, D., Raschendorfer, M., Reinhardt, T., Ritter, B., Schrodin, R., Schulz, J.-P., et al. (2011). A description of the nonhydrostatic regional cosmo model. part ii: Physical parameterization. *Deutscher Wetterdienst, Offenbach, Germany*.

Dufresne, J.-L., & Bony, S. (2008). An assessment of the primary sources of spread of global warming estimates from coupled atmosphere–ocean models. *Journal of Climate*, *21*(19), 5135–5144.

Durre, I., Yin, X., Vose, R. S., Applequist, S., Arnfield, J., Korzeniewski, B., & Hundermark, B. (2016). *Integrated global radiosonde archive (igra), version 2.* (Dataset IGRA - v2) [DOI:10.7289/V5X63K0Q (accessed 2021-06-01).]. NOAA National Centers for Environmental Information. Ann Arbor , MI.

Eastman, R., & Warren, S. G. (2014). Diurnal cycles of cumulus, cumulonimbus, stratus, stratocumulus, and fog from surface observations over land and ocean. *Journal of climate*, *27*(6), 2386–2404.

EUMETSAT. (2004). *Meteosat second generation*. Retrieved October 5, 2023, from https://www.eumetsat.int/meteosat-second-generation

EUMETSAT. (2012). The conversion from effective radiances to equivalent brightness temperatures.

Eumetsat. (2012). Effective radiance and brightness temperature relation tables for meteosat second generation. http://www.eumetsat.int

Fletcher, S. J. (2023). Chapter 14 - observations. In S. J. Fletcher (Ed.), *Data assimilation for the geosciences (second edition)* (Second Edition, pp. 601–629). Elsevier. https://doi.org/https://doi.org/10.1016/B978-0-32-391720-9.00018-8

Fleury, L., Boichard, J.-L., Brissebrat, G., Cloché, S., Eymard, L., Mastrorillo, L., Moulaye, O., Ramage, K., Asencio, N., Coppeaux, J., et al. (2011). Amma information system: An efficient cross-disciplinary tool and a legacy for forthcoming projects. *Atmospheric Science Letters*, *12*(1), 149–154.

Garcin, Y., Deschamps, P., Ménot, G., De Saulieu, G., Schefuss, E., Sebag, D., Dupont, L. M., Oslisly, R., Brademann, B., Mbusnum, K. G., et al. (2018). Early anthropogenic impact on western central african rainforests 2,600 y ago. *Proceedings of the National Academy of Sciences*, *115*(13), 3261–3266.

Gassmann, A., & Herzog, H.-J. (2008). Towards a consistent numerical compressible non-hydrostatic model using generalized hamiltonian tools. *Quarterly Journal of the Royal Meteorological Society*, *134*(635), 1597–1613.

Guidosse, Q., Du Jardin, P., White, L., Lassois, L., & Doucet, J.-L. (2022). Gabon's green gold: A bibliographical review of thirty years of research on okoumé (aucoumea klaineana pierre). *Biotechnologie, Agronomie, Société et Environnement*, *26*(1).

Hahn, C. J., & Warren, S. G. (1999). *Extended edited synoptic cloud reports from ships and land stations over the globe, 1952-1996* (tech. rep.). Oak Ridge National Lab.(ORNL), Oak Ridge, TN (United States).

Hannak, L., Knippertz, P., Fink, A. H., Kniffka, A., & Pante, G. (2017). Why do global climate models struggle to represent low-level clouds in the west african summer monsoon? *Journal of Climate*, *30*(5), 1665–1687.

Hartman, A. T. (2018). An analysis of the effects of temperatures and circulations on the strength of the low-level jet in the turkana channel in east africa. *Theoretical and Applied Climatology*, *132*, 1003–1017.

Heidke, P. (1926). Berechnung des erfolges und der güte der windstärkevorhersagen im sturmwarnungsdienst. *Geografiska Annaler*, *8*(4), 301–349.

Hersbach, H., Bell, B., Berrisford, P., Hirahara, S., Horányi, A., Muñoz-Sabater, J., Nicolas, J., Peubey, C., Radu, R., Schepers, D., Simmons, A., Soci, C., Abdalla, S., Abellan, X.,

Balsamo, G., Bechtold, P., Biavati, G., Bidlot, J., Bonavita, M., … Thépaut, J. N. (2020). The era5 global reanalysis. *Quarterly Journal of the Royal Meteorological Society*, *146*, 1999–2049. https://doi.org/10.1002/qj.3803

Herzog, H.-J., & Gaßmann, A. (2005). *Lorenz-and charney-phillips vertical grid experimentation using a compressible nonhydrostatic toy-model relevant to the fast-mode part of the" lokal-modell"* (tech. rep.). DWD.

Hogan, R. J., & Illingworth, A. J. (2000). Deriving cloud overlap statistics from radar. *Quarterly Journal of the Royal Meteorological Society*, *126*(569), 2903–2909.

Holmlund, K., Grandell, J., Schmetz, J., Stuhlmann, R., Bojkov, B., Munro, R., Lekouara, M., Coppens, D., Viticchie, B., August, T., et al. (2021). Meteosat third generation (mtg): Continuation and innovation of observations from geostationary orbit. *Bulletin of the American Meteorological Society*, 1–71.

Houze, R. A. (2014). Chapter 3 - cloud microphysics. In R. A. Houze (Ed.), *Cloud dynamics* (pp. 47–76). Academic Press. https://doi.org/https://doi.org/10.1016/B978-0-12-374266-7.00003-2

Howard, E., & Washington, R. (2018). Characterizing the synoptic expression of the angola low. *Journal of Climate*, *31*(17), 7147–7165.

Hymas, O. (2016). *L'okoumé, fils du manioc: Post-logging in remote rural forest areas of gabon and its long-term impacts on development and the environment* (Doctoral dissertation). UCL (University College London).

Imbol Koungue, R. A., Rouault, M., Illig, S., Brandt, P., & Jouanno, J. (2019). Benguela niños and benguela niñas in forced ocean simulation from 1958 to 2015. *Journal of Geophysical Research: Oceans*, *124*(8), 5923–5951.

Jiang, J. H., Su, H., Zhai, C., Perun, V. S., Del Genio, A., Nazarenko, L. S., Donner, L. J., Horowitz, L., Seman, C., Cole, J., et al. (2012). Evaluation of cloud and water vapor simulations in cmip5 climate models using nasa "a-train" satellite observations. *Journal of Geophysical Research: Atmospheres*, *117*(D14).

Jiang, Q. (2003). Moist dynamics and orographic precipitation. *Tellus A: Dynamic Meteorology and Oceanography*, *55*(4), 301–316.

Kimura, R. (2002). Numerical weather prediction. *Journal of Wind Engineering and Industrial Aerodynamics*, *90*(12-15), 1403–1414.

Klein, S. A., Hall, A., Norris, J. R., & Pincus, R. (2018). *Low-cloud feedbacks from cloud-controlling factors: A review*. Springer.

Klein, S. A., & Hartmann, D. L. (1993). The seasonal cycle of low stratiform clouds. *Journal of Climate*, *6*(8), 1587–1606.

Laing, A. G., Carbone, R. E., & Levizzani, V. (2011). Cycles and propagation of deep convection over equatorial africa. *Monthly Weather Review*, *139*(9), 2832–2853.

Lauer, A., & Hamilton, K. (2013). Simulating clouds with global climate models: A comparison of cmip5 results with cmip3 and satellite data. *Journal of Climate*, *26*(11), 3823–3845.

Lensky, I. M., & Rosenfeld, D. (2008). Clouds-aerosols-precipitation satellite analysis tool (capsat). *Atmospheric Chemistry and Physics*, *8*, 6739–6753. https://doi.org/10.5194/acp-8-6739-2008

Leuenberger, D., Koller, M., Fuhrer, O., & Schär, C. (2010). A generalization of the sleve vertical coordinate. *Monthly Weather Review*, *138*(9), 3683–3689.

Lohmann, U., Lüönd, F., & Mahrt, F. (2016). *An introduction to clouds: From the microscale to climate*. Cambridge University Press.

Lohou, F., Kalthoff, N., Adler, B., Babić, K., Dione, C., Lothon, M., Pedruzo-Bagazgoitia, X., & Zouzoua, M. (2020). Conceptual model of diurnal cycle of low-level stratiform clouds over southern west africa. *Atmospheric Chemistry and Physics*, *20*(4), 2263–2275.

Lott, F., & Miller, M. J. (1997). A new subgrid-scale orographic drag parametrization: Its formulation and testing. *Quarterly Journal of the Royal Meteorological Society*, *123*(537), 101–127.

Mace, G. G., & Zhang, Q. (2014). The cloudsat radar-lidar geometrical profile product (rl-geoprof): Updates, improvements, and selected results. *Journal of Geophysical Research: Atmospheres*, *119*(15), 9441–9462.

Maley, J., Doumenge, C., Giresse, P., Mahé, G., Philippon, N., Hubau, W., Lokonda, M. O., Tshibamba, J. M., & Chepstow-Lusty, A. (2018). Late holocene forest contraction and fragmentation in central africa. *Quaternary Research*, *89*(1), 43–59.

Maloba Makanga, J.-D. (2010). *Les précipitations au gabon: Climatologie analytique en afrique*. L'Harmattan.

Marchand, R., & Mace, G. G. (2018). Level 2 geoprof product process description and interface control document.

Marchand, R., Mace, G. G., Ackerman, T., & Stephens, G. (2008). Hydrometeor detection using cloudsat—an earth-orbiting 94-ghz cloud radar. *Journal of Atmospheric and Oceanic Technology*, *25*(4), 519–533.

Mayaux, P., Pekel, J.-F., Desclée, B., Donnay, F., Lupi, A., Achard, F., Clerici, M., Bodart, C., Brink, A., Nasi, R., et al. (2013). State and evolution of the african rainforests between 1990 and 2010. *Philosophical Transactions of the Royal Society B: Biological Sciences*, *368*(1625), 20120300.

Megevand, C. (2013). *Integrated safeguards data sheet (concept stage)-gabon-sustainable management of critical wetlands ecosystems-p143914* (tech. rep.). The World Bank.

MetOffice. (2012). Met office integrated data archive system (midas) land and marine surface stations data (1853-current). *NCAS British Atmospheric Data Centre*.

Michalakes, J., & Vachharajani, M. (2008). Gpu acceleration of numerical weather prediction. *2008 IEEE International Symposium on Parallel and Distributed Processing*, 1–7.

Mlawer, E. J., Taubman, S. J., Brown, P. D., Iacono, M. J., & Clough, S. A. (1997). Radiative transfer for inhomogeneous atmospheres: Rrtm, a validated correlated-k model for the longwave. *Journal of Geophysical Research Atmospheres*, *102*, 16663–16682. https://doi.org/10.1029/97jd00237

Moroshkin, K., Bubnov, V., & Bulatov, R. (1970). Water circulation in the eastern south atlantic ocean. *OCEANOLOGY, VOL 10, NO 1, P 27-34, 1970. 8 P, 4 FIG, 13 REF.*

NASA. (2003a). *Cloud profiling radar*. Retrieved October 24, 2023, from https://cloudsat.atmos.colostate.edu/instrument

NASA. (2003b). *Cloudsat*. Retrieved October 24, 2023, from https://eospso.nasa.gov/missions/cloudsat

NASA. (2011). *Cloudsat battery issue*. Retrieved October 24, 2023, from https://cloudsat.atmos.colostate.edu/news/CloudSat_status

national d'études spatiales - CNES, C. (2003). *Calipso*. Retrieved October 24, 2023, from https://calipso.cnes.fr/en/CALIPSO/index.htm

Neggers, R. (2015). Attributing the behavior of low-level clouds in large-scale models to subgrid-scale parameterizations. *Journal of Advances in Modeling Earth Systems*, *7*(4), 2029–2043.

Nelson, G. (1992). Equatorward wind and atmospheric pressure spectra as metrics for primary productivity in the benguela system. *South African journal of marine science*, *12*(1), 19–28.

Nicholson, S., Klotter, D., Dezfuli, A., & Zhou, L. (2018). New rainfall datasets for the congo basin and surrounding regions. *Journal of Hydrometeorology*, *19*(8), 1379–1396.

Oliveira, R. S., Eller, C. B., Bittencourt, P. R., & Mulligan, M. (2014). The hydroclimatic and ecophysiological basis of cloud forest distributions under current and projected climates. *Annals of Botany*, *113*(6), 909–920.

Orr, A., Bechtold, P., Scinocca, J., Ern, M., & Janiskova, M. (2010). Improved middle atmosphere climate and forecasts in the ecmwf model through a nonorographic gravity wave drag parameterization. *Journal of Climate*, *23*, 5905–5926. https://doi.org/10.1175/2010JCLI3490.1

Pan, Y., Birdsey, R. A., Fang, J., Houghton, R., Kauppi, P. E., Kurz, W. A., Phillips, O. L., Shvidenko, A., Lewis, S. L., Canadell, J. G., et al. (2011). A large and persistent carbon sink in the world's forests. *Science*, *333*(6045), 988–993.

Peterson, R. G., & Stramma, L. (1991). Upper-level circulation in the south atlantic ocean. *Progress in oceanography*, *26*(1), 1–73.

Philander, S., Gu, D., Lambert, G., Li, T., Halpern, D., Lau, N., & Pacanowski, R. (1996). Why the itcz is mostly north of the equator. *Journal of climate*, *9*(12), 2958–2972.

Philippon, N., Cornu, G., Monteil, L., Gond, V., Moron, V., Pergaud, J., Sèze, G., Bigot, S., Camberlin, P., Doumenge, C., et al. (2019). The light-deficient climates of western central african evergreen forests. *Environmental Research Letters*, *14*(3), 034007.

Philippon, N., De Lapparent, B., Gond, V., Sèze, G., Martiny, N., Camberlin, P., Cornu, G., Morel, B., Moron, V., Bigot, S., et al. (2016). Analysis of the diurnal cycles for a better understanding of the mean annual cycle of forests greenness in central africa. *Agricultural and Forest Meteorology*, *223*, 81–94.

Prein, A. F., Langhans, W., Fosser, G., Ferrone, A., Ban, N., Goergen, K., Keller, M., Tölle, M., Gutjahr, O., Feser, F., et al. (2015). A review on regional convection-permitting climate modeling: Demonstrations, prospects, and challenges. *Reviews of geophysics*, *53*(2), 323–361.

Prill, F., Reinert, D., Rieger, D., & Zängl, G. (2022). Icon tutorial. *ICON*.

Raschendorfer, M. (2001). The new turbulence parameterization of lm. *COSMO newsletter*, *1*, 89–97.

Reinert, D., Prill, F., Frank, H., Denhard, M., Baldauf, M., Schraff, C., Gebhardt, C., Marsigli, C., & Zängl, G. (2020). Dwd database reference for the global and regional icon and icon-eps forecasting system. *DWD 2023Available online: https://www. dwd. de/DWD/forschung/nwv/fepub/icon_database_main. pdf (accessed on 27 January 2023)*.

Research Data Archive, C., & Information Systems Laboratory, U. C. f. A. R., National Center for Atmospheric Research. (2014). *Ncar upper air database, 1920-ongoing* (tech. rep.) [DOI:10.7289/V5X63K0Q (accessed 2021-06-01).]. National Center for Atmospheric Research. Research Data Archive at the National Center for Atmospheric Research, Computational; Information Systems Laboratory.

Richardson, L. F. (1922). *Weather prediction by numerical process*. University Press.

Roehrig, R., Bouniol, D., Guichard, F., Hourdin, F., & Redelsperger, J.-L. (2013). The present and future of the west african monsoon: A process-oriented assessment of cmip5 simulations along the amma transect. *Journal of Climate*, *26*(17), 6471–6505.

Schär, C., Leuenberger, D., Fuhrer, O., Lüthi, D., & Girard, C. (2002). A new terrain-following vertical coordinate formulation for atmospheric prediction models. *Monthly Weather Review*, *130*(10), 2459–2480.

Schlemmer, L., Zängl, G., Helmert, J., Köhler, M., Mironov, D., Raschendorfer, M., Reinert, D., Rieger, D., Schäfer, S., & Seifert, A. (2020). *Icon model parameters suitable for model tuning* (tech. rep.).

Schmid, J. (2000). The seviri instrument. *Proceedings of the 2000 EUMETSAT meteorological satellite data user's conference, Bologna, Italy*, *29*, 13–32.

Schrage, J. M., & Fink, A. H. (2012). Nocturnal continental low-level stratus over tropical west africa: Observations and possible mechanisms controlling its onset. *Monthly Weather Review*, *140*(6), 1794–1809.

Schrodin, R., & Heise, E. (2001). *The multi-layer version of the dwd soil model terra_lm* (tech. rep.). DWD.

Schulz, J.-P., Vogel, G., Becker, C., Kothe, S., Rummel, U., & Ahrens, B. (2016). Evaluation of the ground heat flux simulated by a multi-layer land surface scheme using high-quality observations at grass land and bare soil. *Meteorologische Zeitschrift*, *25*(5), 607–620. https://doi.org/10.1127/metz/2016/0537

Seifert, A. (2008). A revised cloud microphysical parameterization for cosmo-lme. *COSMO Newsletter*, *7*, 25–28.

Shannon, L., & Pillar, S. (1986). The benguela ecosystem. part iii. plankton. *Oceanogr Mar Biol Annu Rev*, *24*, 65–170.

Shuman, F. G. (1989). History of numerical weather prediction at the national meteorological center. *Weather and forecasting*, *4*(3), 286–296.

Smith, A., Lott, N., & Vose, R. (2011). The integrated surface database - isd: Recent developments and partnerships. *Bull. Amer. Meteor. Soc.*, *92*, 704–708.

Spracklen, D. V., Arnold, S. R., & Taylor, C. (2012). Observations of increased tropical rainfall preceded by air passage over forests. *Nature*, *489*(7415), 282–285.

Stensrud, D. J. (2009). *Parameterization schemes: Keys to understanding numerical weather prediction models*. Cambridge University Press.

Tiedtke, M. (1989). A comprehensive mass flux scheme for cumulus parameterization in large-scale models. *Monthly weather review*, *117*(8), 1779–1800.

Toracinta, E. R., & Zipser, E. J. (2001). Lightning and ssm/i-ice-scattering mesoscale convective systems in the global tropics. *Journal of Applied Meteorology and Climatology*, *40*(6), 983–1002.

van der Linden, R., Fink, A. H., & Redl, R. (2015). Satellite-based climatology of low-level continental clouds in southern west africa during the summer monsoon season. *Journal of Geophysical Research: Atmospheres*, *120*(3), 1186–1201.

Vignesh, P. P., Jiang, J. H., Kishore, P., Su, H., Smay, T., Brighton, N., & Velicogna, I. (2020). Assessment of cmip6 cloud fraction and comparison with satellite observations. *Earth and Space Science*, *7*(2), e2019EA000975.

Viúdez-Mora, A., Costa-Surós, M., Calbó, J., & González, J. (2015). Modeling atmospheric longwave radiation at the surface during overcast skies: The role of cloud base height. *Journal of Geophysical Research: Atmospheres*, *120*(1), 199–214.

von Danckelmann, A. (1878). *Die meteorologischen beobachtungen der güssfeldt'schen loango-expedition*. Frohberg. https://books.google.de/books?id=a9yE1OcnjBEC

von Danckelmann, A., & Lorenz, O. (1878). *Resultate aus den beobachtungen des dr. o. lenz in den ogoweländern*. Frohberg. https://books.google.de/books?id=a9yE1OcnjBEC

Wang, P. K. (2013). *Clouds and precipitaiton*. Cambridge University Press.

Williams, E., & Sàtori, G. (2004). Lightning, thermodynamic and hydrological comparison of the two tropical continental chimneys. *Journal of Atmospheric and Solar-Terrestrial Physics*, *66*(13-14), 1213–1231.

Wilson, A. M., & Jetz, W. (2016). Remotely sensed high-resolution global cloud dynamics for predicting ecosystem and biodiversity distributions. *PLoS biology*, *14*(3), e1002415.

Winker, D. M., Hunt, W. H., & McGill, M. J. (2007). Initial performance assessment of caliop. *Geophysical Research Letters*, *34*(19).

WMO. (2019a). *International cloud atlas of the world meteorological organization*. Retrieved October 5, 2023, from https://cloudatlas.wmo.int/en/observation-of-clouds-from-the-earths-surface.html

WMO. (2019b). *Manual on codes, volume i.1 – international codes (wmo-no. 306)* (tech. rep.). World Meteorologcial Organization.

Yoshino, M. (1981). Orographically-induced atmospheric circulations. *Progress in physical geography*, *5*(1), 76–98.

Zängl, G., Reinert, D., Rípodas, P., & Baldauf, M. (2015). The icon (icosahedral non-hydrostatic) modelling framework of dwd and mpi-m: Description of the non-hydrostatic dynamical core. *Quarterly Journal of the Royal Meteorological Society*, *141*, 563–579.

Zipser, E. J., Cecil, D. J., Liu, C., Nesbitt, S. W., & Yorty, D. P. (2006). Where are the most intense thunderstorms on earth? *Bulletin of the American Meteorological Society*, *87*(8), 1057–1072.